

AD-A112 253

PHYSICAL SCIENCES INC WOBURN MA
LABCEDE AND COCHISE ANALYSIS II.
FEB 80 B D GREEN, G E CALEDONIA

VOLUME II.(U)

F/G 7/4

F1962A-77-C-0089

UNCLASSIFIED

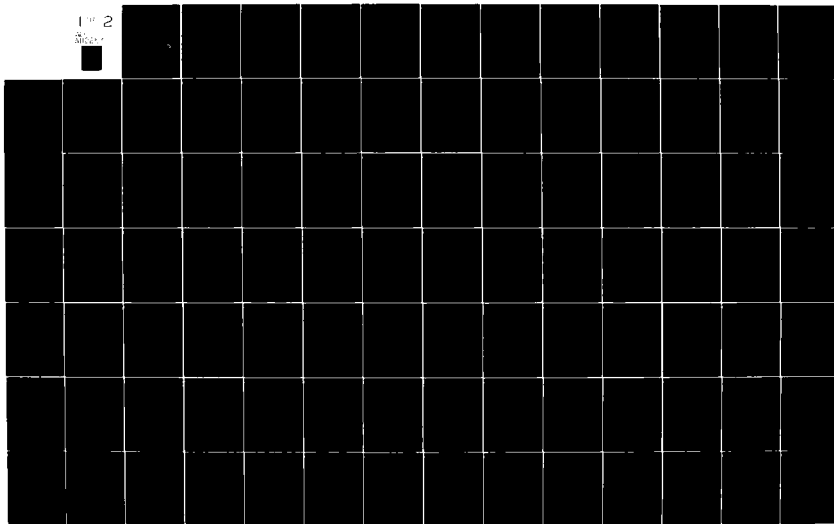
PSI-TR-2078

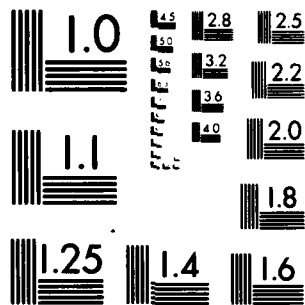
AFOL-TR-80-0063(II)

NL

1 of 2

AD-A112 253





MICROCOPY RESOLUTION TEST CHART
NATIONAL BUREAU OF STANDARDS-1963-A

12

ADA112253

AFGL-TR-80-0063(II)

LABCEDE AND COCHISE ANALYSIS II
Volume II: LABCEDE Studies

B. D. Green
G. E. Caledonia

Physical Sciences, Inc.
30 Commerce Way
Woburn, Massachusetts 01801

February 1980

Final Report
10 December 1978 - 10 February 1980

Approved for public release; distribution unlimited

DTIC
SELECTED
MAR 22 1982
H

AIR FORCE GEOPHYSICS LABORATORY
AIR FORCE SYSTEMS COMMAND
UNITED STATES AIR FORCE
HANCOM AFB, MASSACHUSETTS 01781

DTIC FILE COPY

82 03 22 131

UNCLASSIFIED

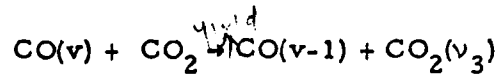
SECURITY CLASSIFICATION OF THIS PAGE (When Data Entered)

REPORT DOCUMENTATION PAGE		READ INSTRUCTIONS BEFORE COMPLETING FORM
1. REPORT NUMBER AFGL-TR-80-0063(II)	2. GOVT ACCESSION NO. AF-A112 252	3. RECIPIENT'S CATALOG NUMBER
4. TITLE (and Subtitle) LABCEDE and COCHISE Analysis II Volume II: LABCEDE Studies		5. TYPE OF REPORT & PERIOD COVERED Final Report 10 Dec. 1976 - 10 Feb. 1980
7. AUTHOR(s) B. D. Green and G. E. Caledonia		6. PERFORMING ORG. REPORT NUMBER PSI TR-207B
9. PERFORMING ORGANIZATION NAME AND ADDRESS PHYSICAL SCIENCES INC. 30 Commerce Way Woburn, MA 01801		8. CONTRACT OR GRANT NUMBER(s) F19628-77-C-0089
11. CONTROLLING OFFICE NAME AND ADDRESS Air Force Geophysics Laboratory Hanscom Air Force Base, MA 01731 Monitor/John Kennealy/OPR		10. PROGRAM ELEMENT, PROJECT, TASK AREA & WORK UNIT NUMBERS 61102F 2301G4AA
14. MONITORING AGENCY NAME & ADDRESS (if different from Controlling Office)		12. REPORT DATE February 1980
		13. NUMBER OF PAGES 181
		15. SECURITY CLASS. (of this report) UNCLASSIFIED
		15a. DECLASSIFICATION/DOWNGRADING SCHEDULE
16. DISTRIBUTION STATEMENT (of this Report) Approved for public release; distribution unlimited		
17. DISTRIBUTION STATEMENT (of the abstract entered in Block 20, if different from Report)		
18. SUPPLEMENTARY NOTES		
19. KEY WORDS (Continue on reverse side if necessary and identify by block number) Infrared Radiation Vibrational Kinetics Chemiluminescence Electron Irradiation Radiation Transfer CO ₂ (v ₃) NO CO N ₂ O		
20. ABSTRACT (Continue on reverse side if necessary and identify by block number) This report describes the analysis of the infrared radiation signatures occurring in electron irradiated mixtures of CO ₂ /Ar. Topics covered include; (1) the development of an absolute calibration for the LABCEDE facility including a mapping of the relative response function across the system field of view, (2) An examination of CO ₂ (v ₃) fluorescence histories with a determination of the electron beam excitation efficiency for the CO ₂ (v ₃) mode, and (3), an analysis of CO fundamental band radiation		

UNCLASSIFIED

SECURITY CLASSIFICATION OF THIS PAGE(When Data Entered)

directed towards the evaluation of the rate constants for the processes



as well as the electron beam rates and efficiencies for producing $\text{CO}(v)$.

The infrared fluorescence of electron irradiated room air and mixtures of N_2/O_2 has been observed over the spectral range of 1000-6700 cm^{-1} . Dominant spectral features include the NO fundamental and first overtone bands as well as the $\text{CO}_2(v_3)$ and $\text{N}_2\text{O}(v_3)$ fundamental bands. Comparisons between the spectra observed in room air and laboratory N_2/O_2 mixtures are provided.

Accession For	
NTIS GRA&I	<input checked="" type="checkbox"/>
DTIC TAB	<input type="checkbox"/>
Unannounced	<input type="checkbox"/>
Justification	
By	
Distribution	
Availability Codes	
1	
2	
3	
4	
5	
6	
7	
8	
9	
10	
11	
12	
13	
14	
15	
16	
17	
18	
19	
20	
21	
22	
23	
24	
25	
26	
27	
28	
29	
30	
31	
32	
33	
34	
35	
36	
37	
38	
39	
40	
41	
42	
43	
44	
45	
46	
47	
48	
49	
50	
51	
52	
53	
54	
55	
56	
57	
58	
59	
60	
61	
62	
63	
64	
65	
66	
67	
68	
69	
70	
71	
72	
73	
74	
75	
76	
77	
78	
79	
80	
81	
82	
83	
84	
85	
86	
87	
88	
89	
90	
91	
92	
93	
94	
95	
96	
97	
98	
99	
100	



UNCLASSIFIED

SECURITY CLASSIFICATION OF THIS PAGE(When Data Entered)

TABLE OF CONTENTS

	<u>Page</u>
I. INTRODUCTION	1
II. CALIBRATION STUDIES	3
III. CO ₂ INFRARED FLUORESCENCE	15
A. The Transmission Function for an Individual Transition	18
B. Transmission of the CO ₂ (ν_3) Band Within the Test Chamber	24
C. The Effect of Atmospheric CO ₂	32
D. Comparison With the Data Base	37
E. Determination of the Excitation Efficiency	73
IV. CO DATA ANALYSIS	83
V. SUMMARY AND CONCLUSIONS	117
VI. ACKNOWLEDGEMENTS	121
VII. REFERENCES	123
APPENDIX	127
I. ABSTRACT	128
II. INTRODUCTION	129
III. EXPERIMENTAL	133
IV. DATA ANALYSIS AND INTERPRETATION	141
V. SUMMARY AND CONCLUSIONS	167
REFERENCES	169

LIST OF ILLUSTRATIONS

<u>Figure</u>		<u>Page</u>
1	Relative response of detector to a constant intensity point source as a function of radial displacement from optical axis.	4
2	Predicted fraction of total detected intensity contained within the normalized radius, r/r_{max} , using the radial detector response function of Fig. 1 and assuming circular symmetry.	5
3	Detector field of view at electron beam.	9
4	Predicted fraction of total electron beam intensity (PbSe 2 mm round detector) contained with radius r using the experimentally measured radial response function Fig. 1 viewing the spatially non-uniform electron beam as in Fig. 3.	11
5	Typical $\text{CO}_2(\nu_3)$ band intensity history.	16
6	Fractional transmission as a function of rotational line-strength times column density for Doppler, Voigt, and Lorentz calculations.	25
7	Total transmitted intensity for all bands as a function of CO_2 pressure for Voigt (solid), Doppler and Lorentz (broken) transmission functions.	29
8	Fractional transmission of four of the strongest bands as function of CO_2 pressure for the Voigt - broadened absorbers.	30
9	Relative contributions of four of the strongest bands to the total transmitted intensity at the chamber window as a function of CO_2 pressure.	31
10	Relative contributions of the three strongest bands to the total transmitted intensity after attenuation by both chamber and atmospheric CO_2 , plotted as a function of chamber CO_2 pressure.	35

LIST OF ILLUSTRATIONS (cont'd)

<u>Figure</u>		<u>Page</u>
11	The fraction of the total CO ₂ fluorescence at the chamber window transmitted through an atmospheric pressure optical path containing various concentrations of CO ₂ plotted as a function of the experimental CO ₂ pressure.	36
12	Normalized experimental data from 11 MARCH RUN 2, 0.1 msec before beam termination.	40
13	Data from 11 MARCH RUN 2, 16 MARCH RUN 2, 16 MARCH RUN 3, and 16 MARCH RUN 4, 0.1 msec before beam termination, normalized to the same scale.	41
14	Predicted fluorescence spectrum transmitted to the chamber window through Voigt broadened absorption lines. 0.33 torr CO ₂ .	42
15	Predicted fluorescence at chamber windows for Voigt lines with 10 cm ⁻¹ resolution. 0.2 torr CO ₂ .	43
16	Predicted fluorescence at chamber window for Voigt lines with 10 cm ⁻¹ resolution. 0.1 torr CO ₂ .	44
17	Predicted fluorescence at chamber window for Voigt lines with 10 cm ⁻¹ resolution. Trace CO ₂ .	45
18	Predicted fluorescence spectrum at the detector after transmission through chamber and atmospheric absorbers. 0.33 torr CO ₂ .	46
19	Predicted spectrum at detector including effects of both chamber and atmospheric absorbers. 0.2 torr CO ₂ .	47
20	Predicted spectrum at detector including effects of both chamber and atmospheric absorbers. 0.1 torr CO ₂ .	48
21	Predicted spectrum at detector including effects of both chamber and atmospheric absorbers. Trace CO ₂ .	49
22	Some predicted spectra at the detector for a range of atmospheric CO ₂ concentrations.	51

LIST OF ILLUSTRATIONS (cont'd)

<u>Figure</u>		<u>Page</u>
23	Comparison of data (broken line) with prediction for 0.1 torr chamber pressure of CO ₂ and atmospheric CO ₂ concentration of 300 ppm.	52
24	Comparison of data taken 0.1 msec before beam termination with 0.2 torr CO ₂ pressure (11 MARCH RUN 1) and prediction assuming the same chamber pressure and 300 ppm ambient CO ₂ concentration.	54
25	Comparison of data, taken 0.1 msec before beam termination with 9.1 torr CO ₂ pressure and a very fast purge, and a prediction assuming 0.25 torr CO ₂ chamber pressure and 66 ppm ambient CO ₂ concentration.	55
26	Comparison of data taken 0.1 msec before beam termination with 0.1 torr CO ₂ pressure and no purge (broken line) with a prediction assuming the same CO ₂ pressure and 430 ppm ambient CO ₂ concentration.	56
27	CO ₂ absorption feature in the spectrum of a 1173 K black-body.	58
28	Hi-tran predictions of blackbody radiation with atmospheric CO ₂ absorption features for a range of CO ₂ pressures.	60
29	Observed fluorescence, 0.1 msec before beam termination, from 0.3 torr CO ₂ , 49.7 torr Ar (18 APRIL RUN 2) with no optical path purge.	63
30	Experimental data, 0.1 msec before beam termination, from a 0.2 torr CO ₂ , 86 torr Ar experimental mixture (18 APRIL RUN 3).	64
31	Fractional transmission as a function of rotational line-strength times column density for two high pressure Voigt calculations.	65
32	Relative contributions of four of the strongest bands to the total transmitted intensity at the chamber window as a function of CO ₂ pressure in 85 Torr of argon.	66

LIST OF ILLUSTRATIONS (cont'd)

<u>Figure</u>		<u>Page</u>
33	Predicted fluorescence at chamber window for Voigt lines broadened by 85 torr Ar. 0.33 torr CO ₂ .	68
34	Predicted fluorescence at chamber window for Voigt lines broadened by 85 torr Ar. 0.1 torr CO ₂ .	69
35	Total transmitted intensity for all bands as a function of CO ₂ pressure for Voigt lines broadened by 85 Torr of Argon.	70
36	Comparison of predicted spectrum using 0.2 torr CO ₂ , 85 torr argon and 430 ppm atmospheric CO ₂ with experimental data (broken line) of Fig. 25.	71
37	Comparison of predicted spectrum using 0.33 torr CO ₂ , 50 torr Ar and 430 ppm atmospheric CO ₂ with experimental data (broken line) of Fig. 24.	72
38	The specific transmittivity as a function of experimental CO ₂ pressure for different amounts of atmospheric CO ₂ : 66 ppm (fast purge), 300 ppm (slow purge) and 430 ppm (no purge).	74
39	Argon excitation efficiencies as a function of primary electron energy for a 1% CO ₂ /99% Ar mixture	80
40	CO ₂ excitation efficiencies as a function of primary electron energy for a 1% CO ₂ /99% Ar mixture.	81
41	CO fluorescence spectra after beam termination plotted every 0.2 msec from 2.8 - 10.0 msec for 16MARCH RUN 2.	89
42	CO fluorescence spectra during beam pulse plotted at 0.2 msec intervals between 1.0 and 2.4 msec for 16MARCH RUN 2.	90
43	Curve fit to data of 11MARCH RUN 2 at 0.3 msec after beam termination.	92
44	Curve fit to data of 11MARCH RUN 2 at 2.5 msec after beam termination conditions as in Fig. 43.	93

LIST OF ILLUSTRATIONS (cont'd)

<u>Figure</u>		<u>Page</u>
45	Curve fit to data of 11MARCH RUN 2 at 4.7 msec after beam termination conditions as in Fig. 43.	94
46	Curve fit to data of 11MARCH RUN 2 at 7.9 msec after beam termination conditions as in Fig. 43.	95
47	Curve fit to data of 11MARCH RUN 2 at 9.3 msec after beam termination conditions as in Fig. 43.	96
48	Population of vibrationally excited CO in the field of view as a function of vibrational level for several different times after beam termination.	98
49	Populations of CO in levels $v = 1 - 7$ within the field of view as a function of time after beam onset.	99
50	Populations of CO in levels $v = 8 - 14$ within the field of view as a function of time after beam onset.	100
51	The absolute relaxation rates for the eight runs in Table VI plotted as a function of vibration level.	104
52	Relaxation rates for the eight runs analyzed.	105
53	Curve fit of 11MARCH RUN 1 data at 0.6 msec after beam initiation.	107
54	Curve fit of 11 MARCH RUN 1 data at 1.4 msec after beam initiation.	108
55	Curve fit of 11MARCH RUN1 data at 2.4 msec after beam initiation (0.1 msec before beam termination).	109
56	Population of CO in levels $v = 1 - 14$ within the field of view as a function of time after the onset of the beam.	110
57	The absolute excitation rates for the 30 kV runs listed in Table VI calculated using data from the time interval 0.0 - 2.4 msec.	111
58	The effective excitation rates per unit energy deposition for the six 30 kV runs.	113

LIST OF TABLES

<u>Table</u>		<u>Page</u>
I	CO ₂ (ν_3) SPECTRAL PROPERTIES	27
II	RUNS INCLUDED IN CO ₂ SPECTRAL ANALYSIS	39
III	PREDICTED FRACTIONAL TRANSMISSIONS OF BLACKBODY RADIATION	61
IV	CO ₂ (ν_3) CONCENTRATIONS AND EXCITATION RATES WITHIN THE FIELD OF VIEW	75
V	ELECTRON EXCITATION EFFICIENCY FOR CO ₂ (ν_3) MODE	77
VI	EXPERIMENTAL CONDITIONS FOR RUNS INCLUDED IN CO ANALYSIS	85
VII	CO EXCITATION PROPERTIES	114

I. INTRODUCTION

The LABCEDE facility is dedicated towards the study of the fluorescence arising from electron irradiated gases. In this experiment a pulsed, collimated, mono-energetic beam of electrons is introduced into a chamber containing a constant pressure, flowing gas. Free radicals and excited atomic or molecular states are created in collisions between the electron beam and gas target and these species can either fluoresce directly or undergo further chemical reactions which ultimately result in fluorescence. In the LABCEDE facility this irradiation induced fluorescence is observed along an optical axis at right angles to the beam direction.

Present studies are directed towards the study of the infrared radiation emitted from electron irradiated gas mixtures of Ar/CO₂. This emission is monitored through use of a Michelson interferometer which is operated in a mode¹ which allows observation of both the spectral and temporal evolution of the fluorescence. Since the electron beam is operated in a pulsed mode (25 msec period, 10% duty cycle), both the fluorescence excitation and decay can be monitored.

The two dominant sources of radiation observed in electron irradiated mixtures of CO₂/Ar are the CO₂(ν_3) band at 4.3 μm and the fundamental vibration/rotation band of CO which spans the spectral region of 4.5 - 6.0 μm . This latter radiation is found to correspond to that of highly vibrationally excited CO present in strongly non-Boltzmann vibrational distributions. A preliminary description of these observations, along with a detailed examination of the electron beam gas interaction, has been presented earlier.² A much larger data base is examined in this report and absolute values of the fluorescence excitation efficiencies are provided.

A detailed examination of the LABCEDE system field-of-view, including the development of an absolute calibration, is presented in Section II.

The $\text{CO}_2(\nu_3)$ data base is considered in Section III. Topics discussed in this section include vibrational relaxation, ν_3 band fluorescence, self absorption and transmission, and the absolute electron excitation efficiency for the $\text{CO}_2(\nu_3)$ mode. An examination of the CO data base is provided in Section IV. Subjects considered include the deduction of the level dependent vibrational relaxation rate constants for collisions between $\text{CO}(\nu)$ and CO_2 , and the determination of the absolute electron excitation efficiency for vibrationally excited CO in Ar/ CO_2 mixtures. Lastly the summary and conclusions of the report are presented in Section V.

An examination of NO vibration/rotation band fluorescence occurring in electron irradiated air and N_2/O_2 mixtures has also been performed during the present reporting period. This work has been described in an earlier report³ and is included here as an appendix.

II. CALIBRATION STUDIES

The first steps in developing an absolute intensity calibration for the LABCEDE system involve defining the interferometer field-of-view and the relative response function of the interferometer for radiation occurring at different positions within this field-of-view. The LABCEDE test chamber is cylindrical with inner radius of 10 cm and length of 16 cm with the electron beam directed along the cylinder axis. A circular arsenic trisulfide window, with radius of 4 cm, is positioned along one side of the cylinder and centered 8 cm downstream of the beam entrance nozzle. The optical axis of the interferometer co-incides with a line drawn radially from the cylinder axis through the center of the window. The distance between the cylinder axis and the entrance slit of the interferometer is 41 cm and the effective internal length of the interferometer is 17 cm. Lastly the distance between the cylinder axis and the window exterior is 13 cm.

The limiting stop of the interferometer is the detector (PbS or PbSe) which is 2mm x 2mm. This detector is positioned immediately beyond a short focal length lens. The optimum relative position of the detector is set by requiring that the detector be filled by the central fringe of the diffraction pattern resulting from a point source positioned along the optical axis at the center of the test tank. Such a setting allows for optimum interferometer resolution for a given throughput while minimizing radial distortion and chromatic aberrations. This setting is achieved by careful positioning of the detector relative to the lens and appropriate masking of the detector. A complication arises in that the central fringes for off-axis radiation will fall off detector center and thus some of this radiation will be lost. The net result is that the system response will be non-uniform across the field-of-view and this effect must be accounted for in the development of an absolute calibration. (Note this effect may be ameliorated by positioning

collimating/telescoping optics between source and interferometer. Such a system is presently under development.)

The interferometer field-of-view was mapped for a source held at a distance of 41 cm from the entrance aperture (corresponding to the distance from the test chamber axis). The detailed detector response within the field-of-view was measured using several different methods:

- by using a blackbody point source and radiometrically measuring relative response as a function of source position perpendicular to the optical axis;
- by using a blackbody point source and interferometrically monitoring relative intensities at several source positions;
- by using a spectrally filtered blackbody point source and radiometrically and interferometrically monitoring as above;
- by using a planar line source (He lamp) much larger than the field-of-view and radiometrically observing detector signal as a function of circular aperture size at the source.

All experiments yielded compatible results; the field-of-view is grossly circular about the optical axis and has a gaussian decay with increasing radial position. The detailed field-of-view as determined by the first method above is displayed in Fig. 1. In Fig. 2, the fraction of the total field-of-view response predicted within radius r is plotted using a radial distribution as displayed in Fig. 1 and assuming cylindrical symmetry. Also plotted are measurements with apertures obtained by the last method above. Agreement is seen to be excellent.

Clearly, response non-uniformity precludes use of the full extended field-of-view area, $\pi(3.8 \text{ cm})^2$, in developing an absolute calibration. The area under the circular Gaussian response curve may be used to determine

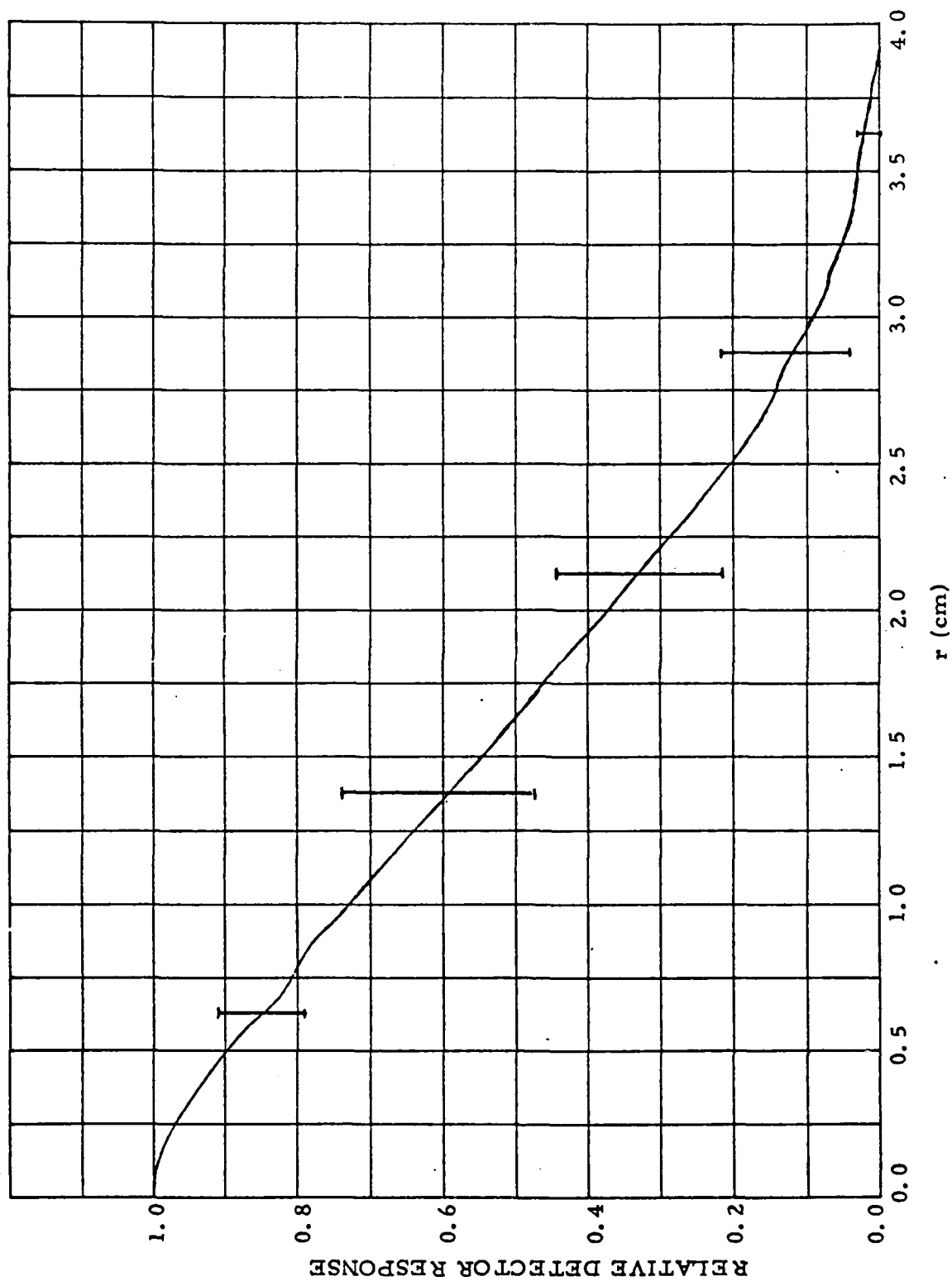


Fig. 1 Relative response of detector to a constant intensity point source as a function of radial displacement from optical axis. Solid line is average of sixteen radial rays. Bars indicate extreme experimental values. Detector is lead selenide 2 mm square, masked to 2 mm round.

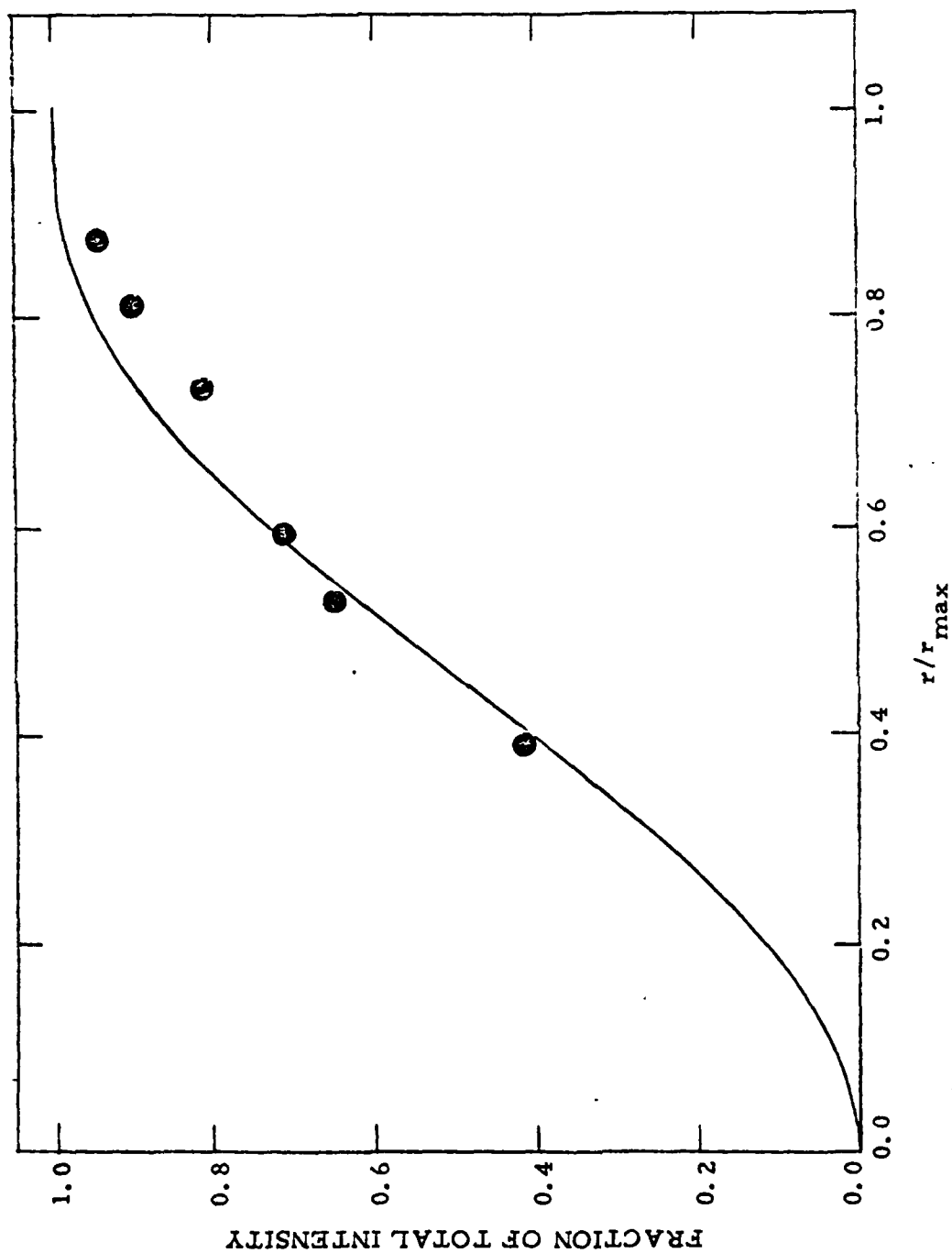


Fig. 2 Predicted fraction of total detected intensity contained within the normalized radius, r/r_{\max} , using the radial detector response function of Fig. 1 and assuming circular symmetry. Prediction is made from blackbody point source data, and r_{\max} is the maximum off axis source displacement which produced measurable signal. Also displayed are measurements using apertures in front of a planar source.

an average flat response across the whole field-of-view or alternately the response may be defined as unitary for radial positions less than an effective radius, r_{eff} and zero beyond this value. For the PbSe detector used for the above study $r_{\text{eff}} = 1.93$ cm at the distance of the electron beam from the interferometer. Note that the area of this effective field-of-view is about one-fourth (0.26) that of the full geometric field-of-view thus exhibiting the severity of the effect of this non-uniform response.

Approximation of the real Gaussian field-of-view by a flat response field-of-view with $r_{\text{eff}} = 1.93$ cm is possible only for a constant extended source which fills the full field-of-view. In the present experiments the radiation source is roughly conical in shape with the cone symmetry axis perpendicular to the interferometer optic axis. The source radiation will be peaked along the horizontal optical center line and the radiation will be highly radially unsymmetric about the center of the detector field-of-view. Furthermore the radiation source need not fill the field-of-view.

The electron beam (and thus fluorescence) spatial distribution may be modeled using empirical formulas developed by Center⁵. For all horizontal positions downstream of beam origin, x , the electron beam current density in a vertical plane perpendicular to the beam axis is a radially symmetric Gaussian about that axis. The radius within which one half of the beam current is contained, $r_{1/2}$, grows with beam propagation through the target chamber:

$$r_{1/2} = x \tan \left(\frac{A(Nx)^{3/2}}{1 + B(Nx)} \right) + r_o \quad (1)$$

Where A and B have values of $4.0 \times 10^{-28} \text{ cm}^3$ and $2.7 \times 10^{-18} \text{ cm}^2$ respectively for an electron beam accelerated by 30 kV propagating through argon,^{2, 5} N is the number density in the test chamber, $2.9 \times 10^{17} \text{ molecules/cm}^3$ for

the case of interest, and r_0 is the beam radius at the chamber entrance. The beam current density at any point in space $i(x, y, z)$ is then simply:

$$i(x, y, z) \propto \frac{I e^{-(r/1.2 r_{1/2})^2}}{\pi r_{1/2}^2} \quad (2)$$

Where I is the total current and the coordinate system is given in Fig. 3. The beam profile presented in the figure is appropriate for 30 kV and 9 torr of argon. Displacements in y and z about the beam axis are symmetric and use of $r = (y^2 + z^2)^{1/2}$ is valid. The detector field-of-view is taken as perpendicular to the beam axis (along z) and is centered on the beam axis at $x = 8$ cm, with the full field-of-view extending from 4.2 to 11.8 cm from the beam entrance to the chamber. For the case of Fig. 3 only 89.7% of the beam current between the planes $x = 4.2, 11.8$ cm fall within this field-of-view.

The response of the interferometer to this non-uniform source may be determined by convoluting the volumetric source function, Eq. (2), over the experimentally determined relative response function displayed in Fig. 1. This has been done for a source corresponding to 30 kV and 9 torr Ar and it was found that the effective system response was 0.32, i. e., as if only 32% of the source radiation produced detector signal. This value is to be compared with the factor of 0.26 deduced for the case of a constant source filling the field-of-view.

It should be noted that the actual beam shape has not been measured in the present experiment. The validity of using Centers formalism has been checked by measuring the variation in the observed interferometer signal with effective test chamber window radius, i. e., limiting the field of view. The source for this test was infrared radiation emanated by CO_2 seeded Ar held at a pressure of 9 torr and irradiated by 30 kV electrons.

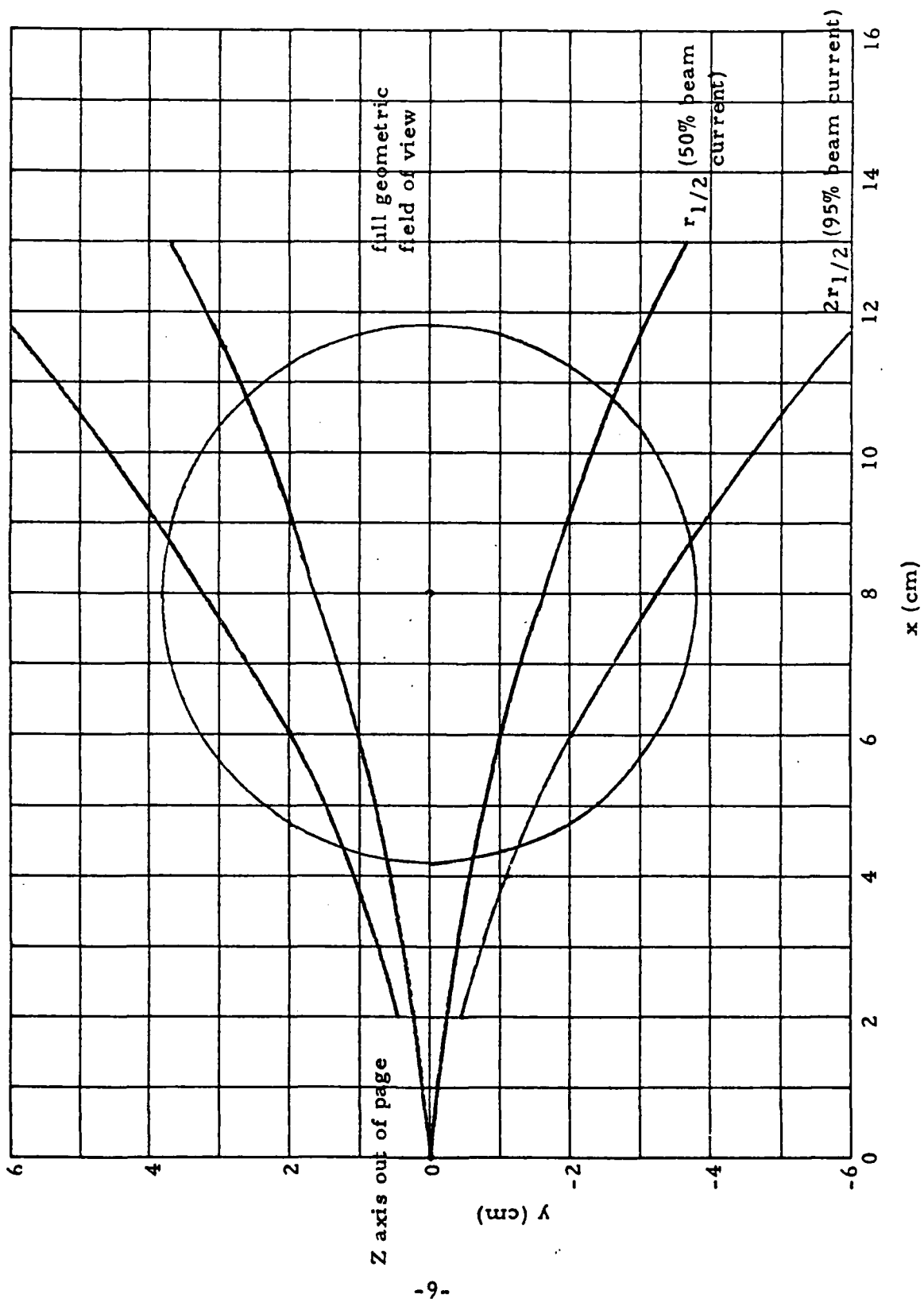


Fig. 3 Detector field of view at electron beam. The beam distribution is symmetric in y, z plane.
 $V = 30 \text{ kV}$ $P = 9 \text{ torr Ar}$

The measured fractional transmitted signal as a function of radius was compared to that predicted by convoluting Eq. (2) over the measured system response function and this comparison is shown in Fig. 4. As can be seen data and theory are in excellent agreement thus providing an additional degree of confidence in the analysis.

The additional correction developed here for source non-uniformity is approximately a 25% effect and is very specific to the choice of beam/gas conditions. However the variation in this correction is not severe. The most pronounced effect of source non-uniformity corresponds to the beam acting as a line source along the cylinder axis and in this case it may be readily shown that the effective relative response would be 0.44. On the other hand as conditions are adjusted such that the beam grows more rapidly the fluorescence becomes more diffuse and the relative response approaches the constant source value of 0.26. It is of course assumed here that the gas does not act as a thick target, i. e., that the electrons are sufficiently energetic to traverse the field-of-view. Furthermore it has been assumed that the fluorescence occurs co-incident with the beam current density. There will actually be a finite time lag between excitation and fluorescence and thus the source of fluorescence can be more diffuse than the electron source, necessitating a smaller response correction. For the characteristic times and gas densities of interest in the present studies excited state diffusion distances will be quite small and this latter effect can be neglected.

It now remains to develop an absolute calibration through use of a black body source. It is to be remembered that the fluorescence from test chamber center traverses a distance of 13 cm prior to entry into the room air environment. Thus the black body was positioned 28 cm rather than 41 cm from the interferometer entrance aperture in order to properly reproduce the effects of atmospheric absorption. The black body source used in the calibration allowed for several different aperture sizes, all of which were

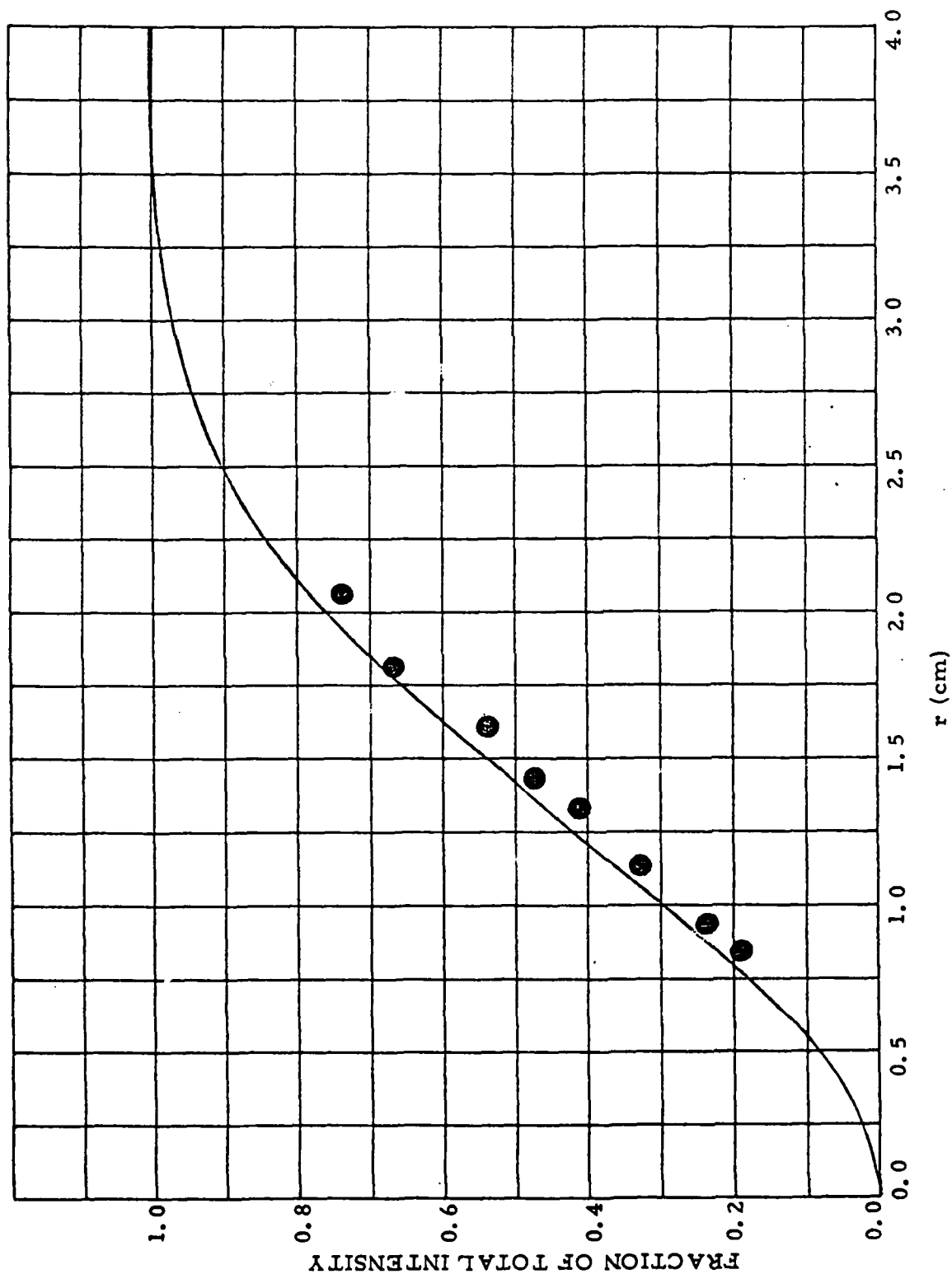


Fig. 4 Predicted fraction of total electron beam intensity (PbSe 2 mm round detector) contained within radius r using the experimentally measured radial response function of Fig. 1 viewing the spatially non-uniform electron beam as in Fig. 3. Also displayed are measurements taken with apertures centered on optical axis (\bullet).

much smaller than the area of the field-of-view. The choice of blackbody aperture size is subject to two opposing constraints. If the aperture area is too small 300 K background radiation dominates the recorded spectrum and the calculated responsivity is much too small. On the other hand if the aperture area is too large, the detector saturates and response becomes nonlinear and too small. This nonlinearity would be uniform for the detector DC level, however, the interferogram intensity would be asymmetrically distorted. The actual experimental data from a pulsed, low intensity source is not restricted by these constraints. A blackbody aperture of area $1 \times 10^{-2} \text{ cm}^2$ was found to be the largest size allowable for a temperature of 1173 K and was used in the calibration.

After the calibration interferogram is Fourier transformed a relation between detector signal and blackbody radiation may be developed, i. e.,

$$S_{BB}(\lambda) = a(\lambda) \epsilon' N_{\lambda} A_{BB} \quad (3)$$

where $S_{BB}(\lambda)$ is the detector signal in mV induced at wavelength λ by a blackbody source having intensity N_{λ} in $\text{W/cm}^2\text{-sr-}\mu\text{m}$ and area A_{BB} . The quantity $a(\lambda)$ is the response function and ϵ' is the collection efficiency for point source radiation positioned along the optical axis 28 cm from the interferometer entrance aperture. This latter quantity may be related to ϵ , the centerline collection efficiency at a distance of 41 cm (tank center), by the inverse square law, i. e.,

$$\epsilon = \left(\frac{45}{58}\right)^2 \epsilon' \quad (4)$$

Note that the internal interferometer length of 17 cm has been added to both distances in Eq. (4)

If I_λ is the total volume radiation in Watts/sr- μm emanated within the field-of-view by a non-uniform source centered along the test chamber axis, then the relevant detector signal would be given by

$$S_S(\lambda) = a(\lambda) \bar{\epsilon} I_\lambda \tau_\lambda \quad (5)$$

where $\bar{\epsilon}$ is the average collection efficiency over the field-of-view specific to the source in question and τ_λ is the transmittivity of the chamber window. The quantity $\bar{\epsilon}$ may be related to the on axis collection efficiency ϵ by the relation

$$\bar{\epsilon} = g \epsilon \quad (6)$$

where g is the previously determined factor which accounts for the non-uniform response of the system, i. e., $g = 0.26$ for a constant source or 0.32 for the e-beam case considered earlier.

The final relationship between source intensity and detector signal is arrived at by combining Eqs. (3) - (6) with the result

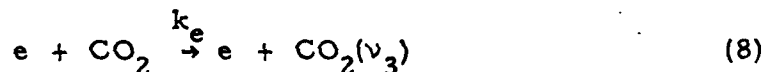
$$I_\lambda = [1.66 N_\lambda A_{BB} S_S(\lambda)] / [g \tau_\lambda S_{BB}(\lambda)] \quad (7)$$

Expression (7) has been used in determining the absolute intensities presented in the following sections. Note that the field-of-view, and the quantity g , can vary significantly with detector change or repositioning. For the data to be discussed the detector configuration exhibited a field-of-view of radius 3.2 cm. It was found that for this field-of-view and the standard case of 30 kV electrons injected into 9 torr of argon, the average normalized response was $g = 0.38$. This circular field-of-view encompasses 77.3% of the beam current density falling between the planes at $x = 4.8, 11.2$ cm.

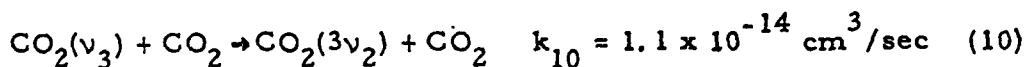
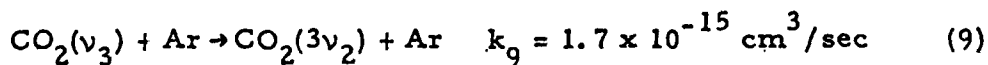
III. CO₂ INFRARED FLUORESCENCE

A number of fluorescence measurements were performed in room temperature mixtures of Ar/CO₂. Typical experimental conditions were P_{Ar} = 9 - 11 torr, P_{CO₂} = 0.1 - 0.3 torr with electron beam parameters V = 30 kV and I ~ 1 mA. In all cases fluorescence due to CO₂(ν₃) band transitions was observed in the spectral region of 2200 - 2400 cm⁻¹. A typical emission history for this band is shown in Fig. 5. The electron beam is operated in the pulsed mode, on 2.5 msec and off 22.5 msec. The history of Fig. 5 shows a continuous increase in the radiation level while the beam is on followed by an exponential decay upon beam termination.

It is anticipated that the appropriate excitation mechanism producing this fluorescence is



where the electrons are dominantly low energy secondary electrons produced in ionizing collisions between the primary electron beam and neutral gas target. The dominant loss mechanisms for CO₂(ν₃) are collisional quenching



where the listed room temperature rate constants are from Yardley and Moore⁶. CO₂(ν₃) deactivation by radiative decay,

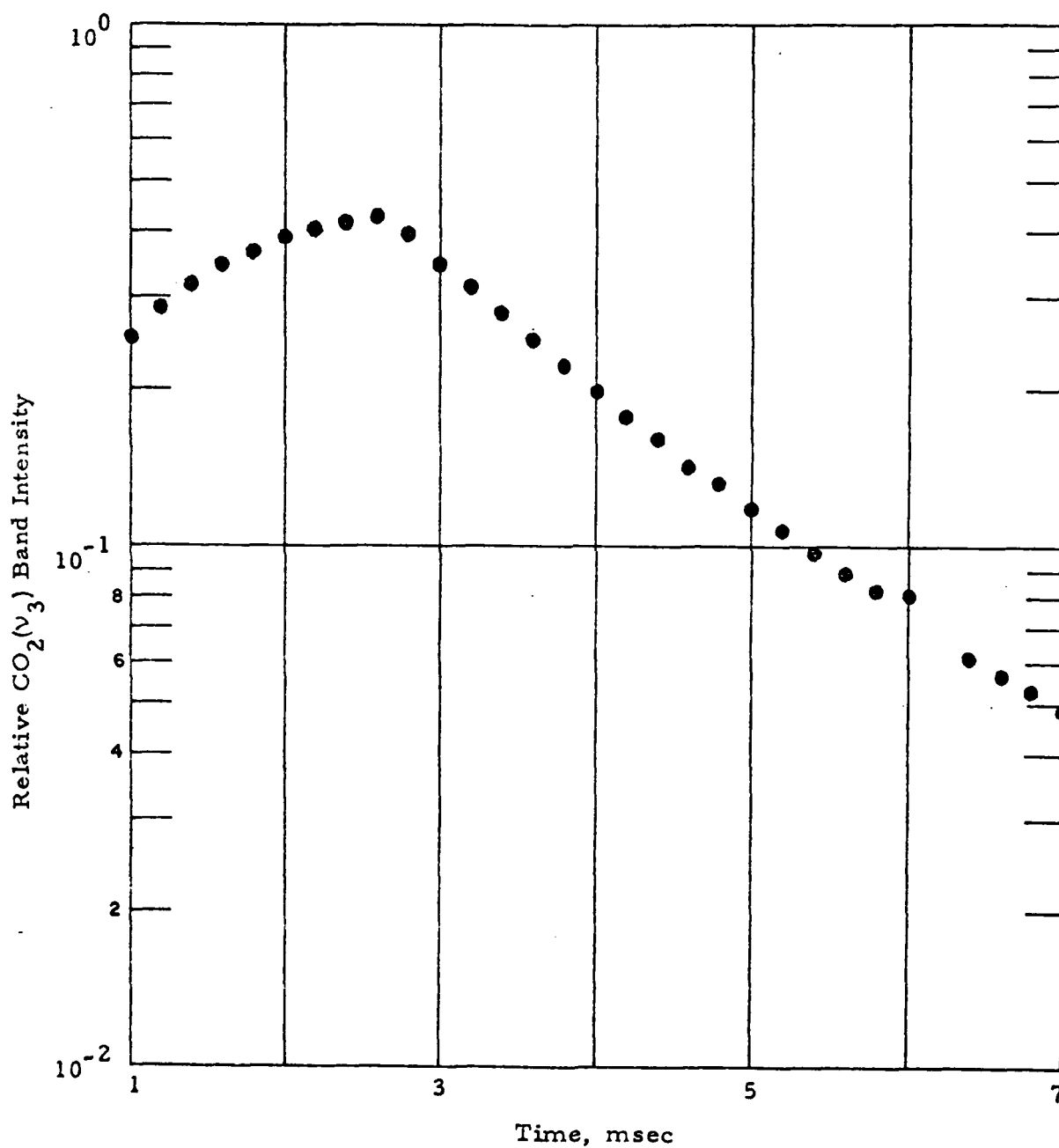
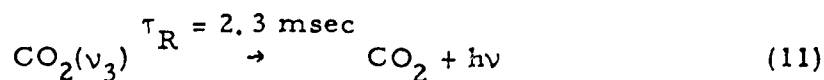


Fig. 5. Typical $\text{CO}_2(v_3)$ band intensity history. Beam termination at 2.5 msec. $P_{\text{Ar}} = 9$ torr, $P_{\text{CO}_2} = 0.2$ torr, $v=30$ kV.



is unimportant inasmuch as the test chamber gas is severely optically thick to ν_3 band radiation². From reactions (9) - (11) it can be readily shown that the total $\text{CO}_2(\nu_3)$ concentration within the field-of-view while the beam is on is given by the relationship

$$N_{\nu_3} = R_{\nu_3} \tau_{\nu_3} [1 - \exp(-t/\tau_{\nu_3})] \quad (12)$$

where R_{ν_3} is the global excitation rate within the field-of-view for reaction (8) and

$$\tau_{\nu_3} = (k_9[\text{Ar}] + k_{10}[\text{CO}_2])^{-1} \quad (13)$$

After beam termination at $t = t_b$ the ν_3 concentration will be given by

$$N_{\nu_3} = N_{\nu_3}(t_b) \exp(-(t - t_b)/\tau_{\nu_3}) \quad (14)$$

Note that the observed decay time of the fluorescence shown in Fig. 5 is 1.7 msec. This value is in excellent agreement with τ_{ν_3} as evaluated from Eq. (13) using the measured rate constants⁶ for k_9 and k_{10} . Given the total measured band intensity I_{ν_3} and the observed value of τ_{ν_3} the total rate of electron excitation R_{ν_3} may be deduced from Eq. (12) through use of the relationship

$$I_{\nu_3} = N_{\nu_3} h\nu f / (4\pi \tau_R) \quad (15)$$

where $h\nu$ is the energy of a ν_3 band photon and f is the specific transmittance of the $\text{CO}_2(\nu_3)$ band along the optical path.

The ultimate goal of this analysis is to determine the absolute efficiency of the electron beam for promoting $\text{CO}_2(\nu_3)$ excitation. As previously discussed² this may be deduced directly from the quantity R_{ν_3} . The prime difficulty in this analysis is in evaluating the quantity f , inasmuch as the $\text{CO}_2(\nu_3)$ fluorescence is not only severely self absorbed within the test chamber, but is also affected by absorption by atmospheric CO_2 along the 45 cm optical path from the chamber window to the detector. The major portion of this section is dedicated to a careful evaluation of the quantity f .

A. The Transmission Function for an Individual Transition

Previously, the transmitted emission from the $\text{CO}_2(\nu_3)$ band was calculated considering the spectral lines to be exclusively Doppler or Lorentz-collisionally broadened. It was noted, however, that the actual shape of the fluorescent lines has contributions from both broadening mechanisms, and that the transmission losses in the chamber for the real line-shape would be intermediate to the two previous calculations. Accordingly, in the present work, a transmission algorithm has been developed for the Voigt profile and used to predict the spectral emission at the chamber window. Furthermore in the earlier analysis the effect of atmospheric CO_2 absorption of the fluorescence was taken into account by means of a low-resolution correction to the experimental data, which will be described more fully later. In the present work, this correction was not applied to the data, but rather, the predictions were corrected to include this effect. As a result, the CO_2 spectral data presented here will be different in appearance than the "corrected" experimental data presented previously. The uncorrected data in both cases is very similar in appearance. Thus, the present approach

is to present the experimental spectrum obtained from the on-detector intensities and compare it with predictions which are corrected for the various transmission losses.

From the electron beam shape shown in Fig. 3, it is seen that the radiating gas will be mainly localized in the field-of-view. For the present predictions, the simplifying assumption has been made that the vibrationally excited gas is located in a plane perpendicular to the detection system optical axis at the center of the chamber. The fluorescence must then travel on average through 11 cm of room temperature vibrationally equilibrated gas prior to reaching the chamber window.

The radiation per unit length from an optically thin source with an emitter concentration of N_R molecules cm^{-3} is

$$I_\nu = k_\nu N_R I_{BB} \quad \text{W/cm}^3 \text{-sr-cm}^{-1} \quad (16)$$

where I_{BB} is the blackbody radiation function and k_ν is the absorption coefficient at frequency ν for the appropriate lineshape. Attenuation of this radiation over a distance L is given by

$$I'_\nu = k_\nu N_R I_{BB} \exp(-KNL) \quad (17)$$

where K is the total absorption coefficient at frequency ν due to all transitions (of all absorbers present) which overlap the emission, i. e.,

$$KN = \sum_i k_{\nu_i} N_i \quad (18)$$

The fractional transmission of a single fluorescence line is given by

$$\tau = \frac{\int_{-\infty}^{\infty} I'_v dv}{\int_{-\infty}^{\infty} I_v dv} = \frac{\int_{-\infty}^{\infty} I_{BB} u(v) \exp(-KNL) dv}{\int_{-\infty}^{\infty} I_{BB} u(v) dv} \quad (19)$$

where $u(v)$ is the functional form of the absorption coefficient frequency dependence relative to its centerline value.

Evaluation of the transmission function for the band requires knowledge of all k_{v_i} at frequency intervals small compared to the molecular linewidth and the solution of Eq. (19) at a large number of frequencies for each emission line. This rigorous approach is both costly and time consuming. However, if the absorption of each emitted line is assumed to occur only by the same CO_2 transition which gave rise to the radiation, then the summation of Eq. (18) is not required, considerably simplifying the calculation. In this limit because the blackbody function is essentially constant over the molecular linewidth, Eq. (19) reduces to

$$\tau = \frac{\int_{-\infty}^{\infty} u(v) \exp(-k_v N_R L) dv}{\int_{-\infty}^{\infty} u(v) dv} \quad (20)$$

In the last report,² this transmission function was evaluated for $\text{CO}_2(v_3)$ band transitions for both Doppler and Lorentz broadened lineshapes. The enhanced emission in the wings of the collision-broadened lineshape resulted in a significantly different fractional transmission than for Doppler lines, about a factor of five greater for a chamber pressure of 1 torr CO_2 .

9 torr argon. Because of this large difference, development of a more detailed transmission prediction for a lineshape more closely approximating the true emission lineshape was warranted.

Doppler and collisional broadening are entirely independent processes and a composite lineshape in which both contribute may be viewed as one in which each frequency element of the inhomogeneously broadened collisional (Lorentz) distribution is broadened by a Doppler distribution. The resultant lineshape, referred to as a Voigt profile, is defined by

$$k_v = k_{v_{CL}} \frac{a}{\pi} \int_{-\infty}^{\infty} \frac{\exp(-y^2)}{a^2 + (\xi - y)^2} dy \quad (21)$$

where $k_{v_{CL}}$ is the centerline absorption coefficient for a Doppler broadened line with a linewidth of b_D (half width at half maximum, HWHM) which may be specified by the relation

$$k_{v_{CL}} = \frac{S}{b_D} \sqrt{\ln 2 / \pi} \quad (22)$$

where S is the integrated linestrength for a single vibration rotation transition in units of cm/molecule. The quantity a in Eq. (6) is the ratio of the Doppler and collisional half widths

$$a = \frac{b_c}{b_D} \sqrt{\ln 2} \quad , \quad (23)$$

y is specified by

$$y = \frac{\sqrt{\ln 2}}{b_D} (\nu' - \nu_{C_L}) \quad (24)$$

and ξ , which represents the doppler lineshape variation with frequency, is defined as

$$\xi = \frac{\sqrt{\ln 2}}{b_D} (\nu - \nu_{C_L}) \quad (25)$$

Integration over the dummy frequency ν' , permits the inclusion of contributions from all Doppler-shifted transitions in the total absorption coefficient at frequency ν .

The room temperature Doppler broadening of the CO_2 molecular lines at the ν_3 transition frequency is $2.2 \times 10^{-3} \text{ cm}^{-1}$ HWHM. Collisional broadening of the lines will include contributions from Ar at 9 torr ($5.8 \times 10^{-4} \text{ cm}^{-1}$ HWHM) and CO_2 self-broadening ($1.3 \times 10^{-5} - 1.3 \times 10^{-4} \text{ cm}^{-1}$ HWHM) for 0.1 - 1.0 torr of CO_2 . Their sum is the collisional half-width, b_c , for a given experiment.

Equation (21) provides the functional form of $u(\nu)$ and substitution into Eq. (20) yields

$$\tau = \frac{\int_{-\infty}^{\infty} d\nu \left[\int_{-\infty}^{\infty} dy \frac{e^{-y^2}}{a^2 + (\xi - y)^2} \exp \left(-k_{\nu_{C_L}} N_R \frac{La}{\pi} \int_{-\infty}^{\infty} dy' \frac{e^{-y'^2}}{a^2 + (\xi - y')^2} \right) \right]}{\int_{-\infty}^{\infty} \left[\int_{-\infty}^{\infty} \frac{e^{-y^2}}{a^2 + (\xi - y)^2} dy \right] d\nu} \quad (26)$$

which is the fractional transmission for an optically thin Voigt-broadened emission source attenuated by resonant non-overlapping Voigt absorbers.

Direct evaluation of Eq. (26) would require integration over the dummy variable ν' at many values of frequency ν over each rotational line. Numerical tabulations of exact Voigt profiles exist but closed-form approximations which permit calculations of the lineshape are more generally applicable. Several algorithms have been developed to permit numerical evaluation of k_ν for Voigt lines.⁷⁻⁹ Whiting's approximation⁷ to the true lineshape has been applied to analyze the present experiments. The Voigt linecenter intensity was first calculated as

$$k_{\nu C_L} = \frac{S}{2b_\nu [1.065 + 0.447d + 0.058 d^2]} \quad (27)$$

where d is the ratio of the Voigt and collisional halfwidths, b_c/b_ν , and

$$b_\nu = \frac{1}{2} [b_c + (b_c^2 + 4b_D^2)^{1/2}] \quad (28)$$

Equation (27) is analogous to Eq. (22) which is for Doppler lines. Equations (27) and (28) have been found to be accurate to within 0.5% of the exact Voigt linewidths and centerline intensity. The Voigt absorption coefficient at any frequency ν relative to line center is approximated by the empirical relation

$$\begin{aligned} \frac{k_\nu}{k_{\nu C_L}} = & (1-d) \exp \left[-2.772 \left(\frac{z}{2b_\nu} \right)^2 \right] + \frac{d}{1 + \left(\frac{z}{b_\nu} \right)^2} \\ & + 0.016(1-d)d \left\{ \exp \left[-0.4 \left(\frac{z}{2b_\nu} \right)^{2.25} \right] - \frac{10}{10 + \left(\frac{z}{2b_\nu} \right)^{2.25}} \right\} \end{aligned} \quad (29)$$

where z is $(\nu - \nu_{CL})$. This expression has been determined to be accurate to within 2.5% of the exact Voigt profile for all ν and is an empirical representation of Eq. (21). Substitution of Eqs. (27) - (29) into Eq. (26) results in a considerable simplification, i. e.,

$$\tau = \frac{\int_{-\infty}^{\infty} k_{\nu}/S \exp[-(SN_R L)(k_{\nu}/S)] d\nu}{\int_{-\infty}^{\infty} k_{\nu}/S d\nu} \quad (30)$$

The fractional transmission of a single rotational line over its entire bandpass may now be calculated as a function of S , the linestrength. A plot of τ vs. $SN_R L$ using Whiting's approximation for the true Voigt lineshape is given in Fig. 6. In addition to the Voigt fractional transmission, the previously derived Doppler and Lorentz transmission functions are also plotted. It is seen that the Voigt transmission shares an asymptote with the Doppler prediction for small values of $SN_R L$. At large values of $SN_R L$, the wings of the lineshape become important and the Lorentzian component of the Voigt profile dominates the dependence of the fractional transmission on line-strength. These transmission predictions were used in conjunction with molecular linestrength calculations, which will be described next, to generate predicted emission spectra at the chamber window.

B. Transmission of the $\text{CO}_2(\nu_3)$ Band Within the Test Chamber

The frequencies and linestrengths were calculated for rotational transitions of the fundamental ν_3 asymmetric stretch of the $\text{O}^{16}\text{C}^{12}\text{O}^{16}$ (626) molecules. Also included in the synthesized spectrum were hot-band transitions with $\Delta\nu_3 = 1$ involving all significantly thermally populated

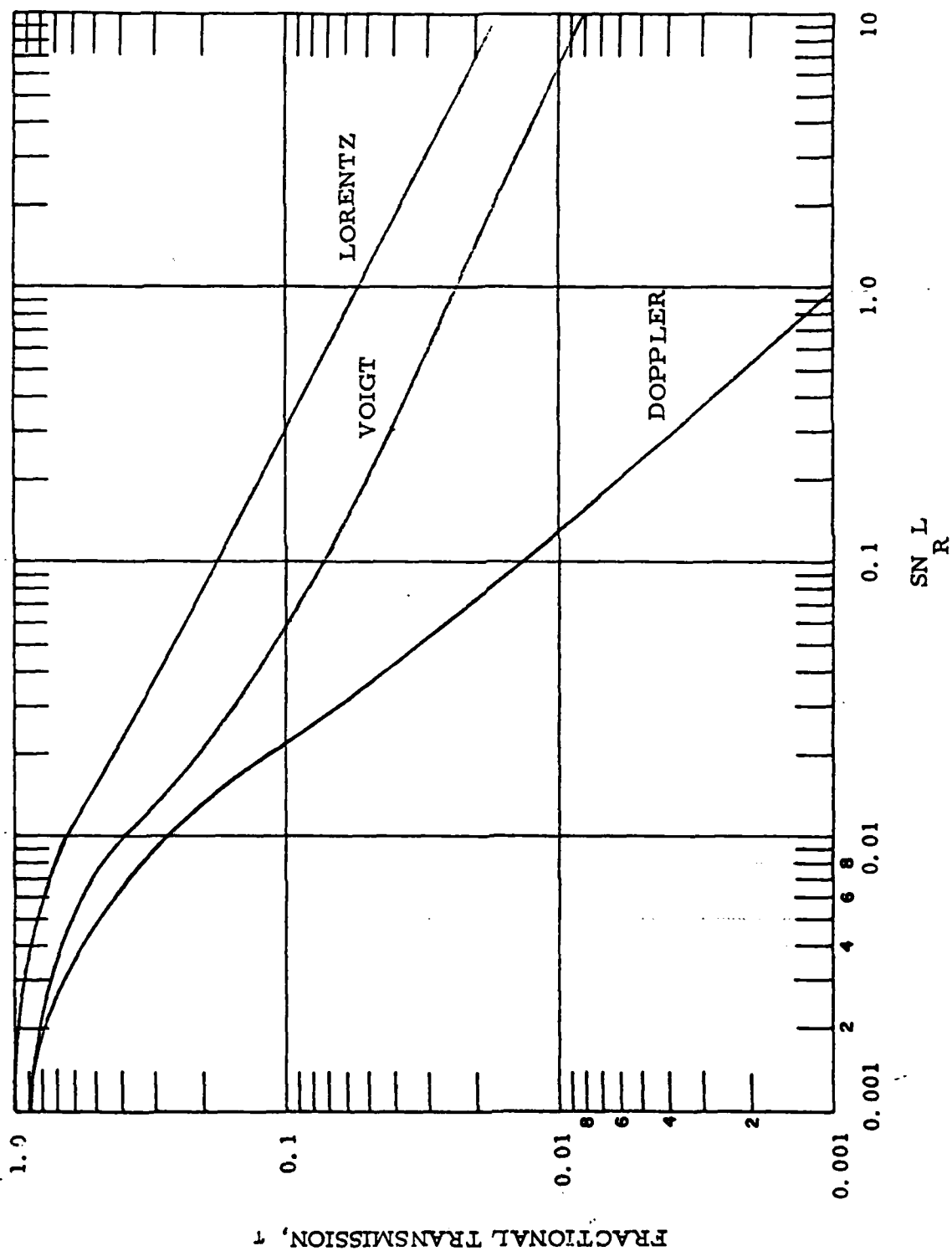


Fig. 6. Fractional transmission as a function of rotational line strength times column density for Doppler, Voigt, and Lorentz calculations. $P_{Ar} = 9$ torr

vibrational modes, as well as the fundamental and hot-band transitions of the $C^{13}O_2^{16}$, $O^{16}C^{12}O^{18}$, and $O^{16}C^{12}O^{17}$ isotopic species. The band center frequencies and integrated vibrational band intensities are given in Table I for all the transitions included in the calculation. The detailed spectroscopic modeling of the rotational line spacings and degeneracies involved in the spectral synthesis has been described previously² and will only be outlined here. The constants on which the calculations are based were taken from the AFCRL Atmospheric Line Parameters Compilation¹¹.

The total integrated bandstrength, S_v , is partitioned among the allowed rotational transitions according to the formula

$$S = \frac{S_v S_J}{Q_{rot}} \exp - \left\{ \frac{J'(J'+1)}{Q_{rot}} \right\} \frac{\nu_{CL}}{\nu_b} \quad (31)$$

where S is the individual rotational linestrength, Q_{rot} is the rotational partition function, J' is the rotational level from which the transition originates, and S_J are the linestrength factors given by the Hönl-London formulae.¹² The emitted intensity per molecule, I , can then be defined for each rotational line by integrating Eq. (16):

$$I = \int_{-\infty}^{\infty} (I_v/N_R) dv = \int_{-\infty}^{\infty} I_{BB} k_v dv = I_{BB} S (W/\text{molecule-sr}) \quad (32)$$

where the relation $S = \int_{-\infty}^{\infty} k_v dv$ has been utilized. The fractional transmission, τ of each line through the Voigt broadened absorbing gas was calculated from Eq. (30) over the range of 0.0 - 1.0 torr CO_2 pressure. The total emitted intensity at the chamber window was obtained as the sum of contributions from each rotational line from all the bands.

TABLE I
CO₂(v₃) SPECTRAL PROPERTIES

Isotope	Transition Ground State $\nu_1 \nu_2^l \nu_3$	S_v^* cm/molec.	ν_{band}^* cm ⁻¹	Branches	Rotational Levels J
626	00 ⁰ 0	9.598E-17	2349.146	P, R	even J only
626	01 ⁰ 0	7.66E-18	2336.637	P, Q, R	all J, c odd
636	00 ⁰ 0	9.602E-19	2283.490	P, R	even J
628	00 ⁰ 0	3.33E-19	2332.112	P, R	all J
626	02 ² 0	3.08E-19	2324.148	P, Q, R	all J, c even
626	02 ⁰ 0	1934E-19	2327.432	P, R	even J
626	10 ⁰ 0	1.183E-19	2326.594	P, R	even J
636	01 ¹ 0	8.18E-20	2271.763	P, Q, R	all J, c odd
627	00 ⁰ 0	6.37E-20	2340.01	P, R	all J
628	01 ¹ 0	2.58E-20	2319.738	P, Q, R	all J, c&d each
626	03 ³ 0	1.22E-20	2311.675	P, Q, R	all J, c odd
627	01 ¹ 0	4.97E-21	2327.575	P, Q, R	all J, c&d each
636	02 ² 0	3.46E-21	2260.045	P, Q, R	all J, c even

* From Ref. 11

This prediction for the total transmitted intensity per molecule is plotted in Fig. 7 as a function of CO₂ pressure. Also displayed are the predictions from previous calculations² for both Lorentz and Doppler broadened absorbers. As expected the predicted Voigt intensity falls between the values of the two earlier calculations at low CO₂ pressures, but follows more closely the pressure dependence of the Lorentzian case. The lower solid curve in the figure will be discussed shortly. As required in the limit of no attenuation (very low CO₂ pressure),

$$\sum_j \sum_i I_{ij} \tau_{ij} = \sum_j S_{v_j} I_{BB}(v_{b_j}) \quad (33)$$

where the summation over i includes all rotational lines and j includes all transitions considered.

The relative contributions of the hot bands and isotopic transitions included in the calculation is demonstrated in Figs. 8 and 9. In Fig. 8, the fractional Voigt transmissions ($\sum_i \tau_{ij}$) are shown as a function of CO₂ pressure for four of the strongest transitions in Table I: the 626 fundamental and first and second excited bending mode transitions (01¹1 and 02²1) and the 636 isotopic fundamental. Although all transitions suffer attenuation which increases with CO₂ pressure, the 626 ν_3 fundamental band radiation will be very severely attenuated, only 3% transmitted at 1 torr pressure. The weaker bands (not shown) will undergo only slight self-absorption and thus will be enhanced relative to the fundamental.

Accordingly, even though the 626 fundamental contains 93% of the total bandstrength of all the transitions (as given by the right hand side of Eq. (33)), it will be responsible for only about 50% of the emission incident on the chamber window as is seen in Fig. 9. The predicted fraction of the total radiation intensity which is due to each band is plotted in this figure as a function of CO₂ pressure for the four bands listed. The strongest hot

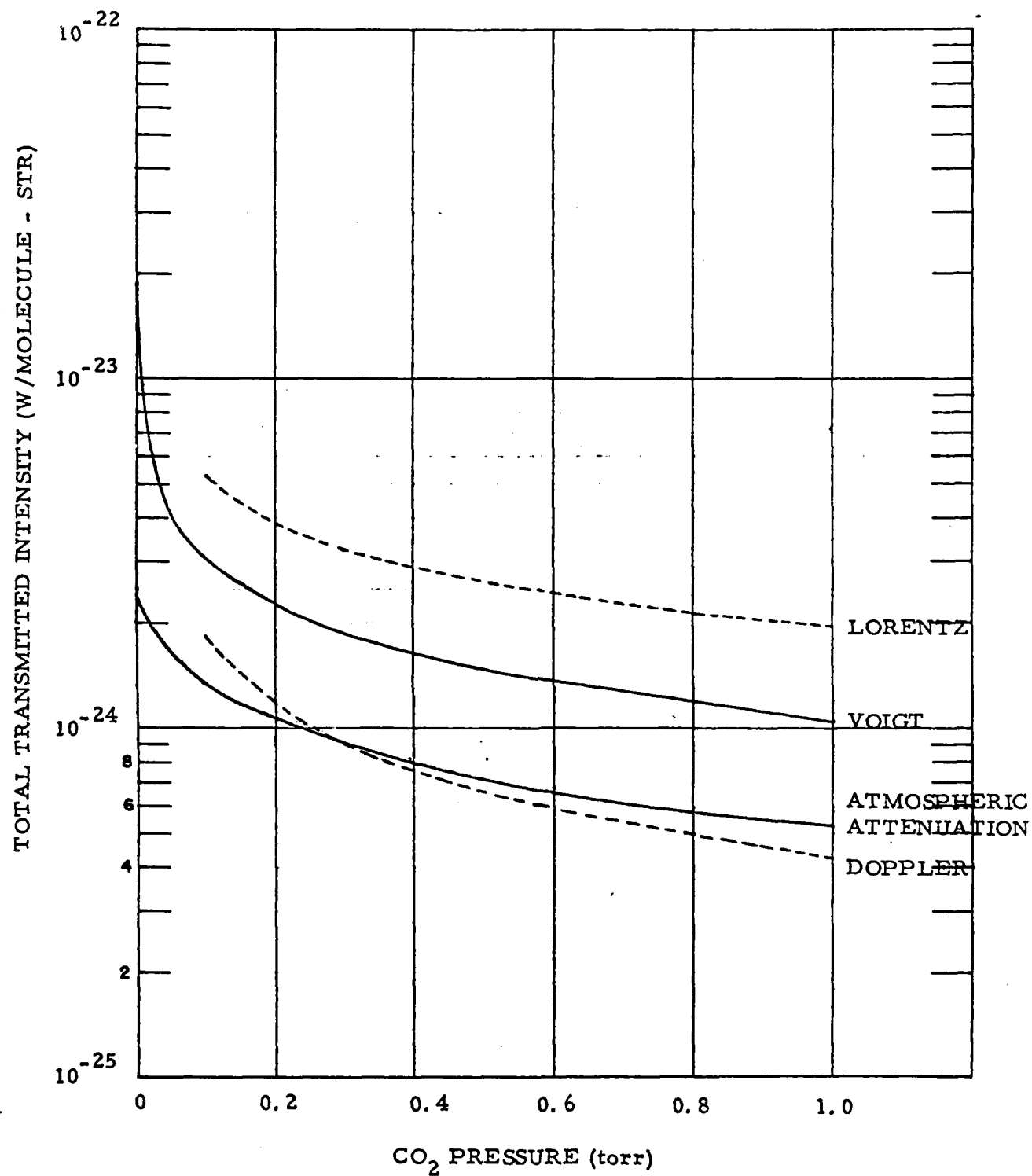


Fig. 7. Total transmitted intensity for all bands as a function of CO₂ pressure for Voigt (solid), Doppler and Lorentz (broken) transmission functions. The lower solid curve is the Voigt prediction corrected for atmospheric CO₂ attenuation. P_{Ar} = 9 torr, L = 11 cm.

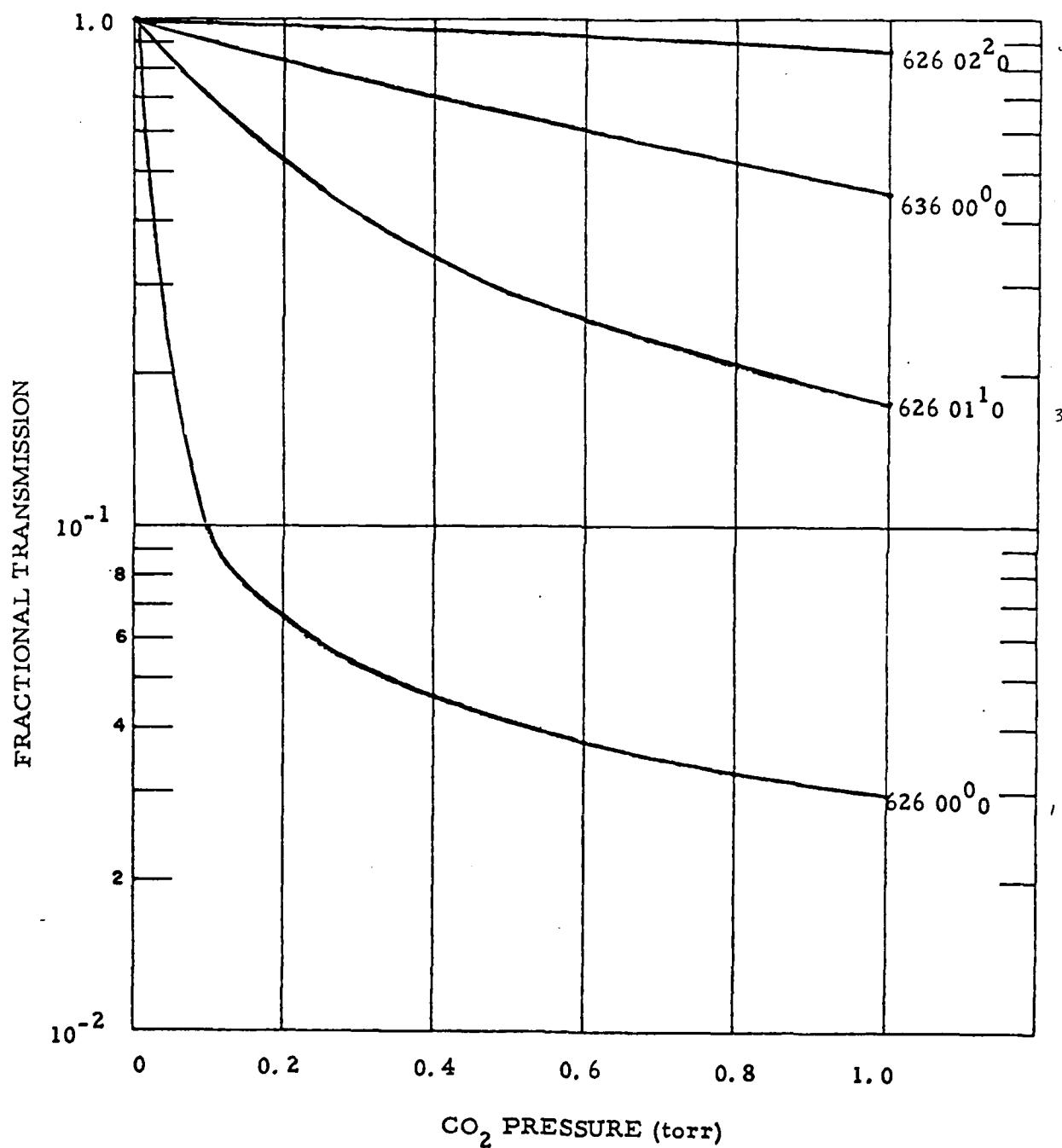


Fig. 8. Fractional transmission of four of the strongest bands as function of CO_2 pressure for the Voigt - broadened absorbers. $P_{\text{Ar}} = 9$ torr, $L = 11$ cm.

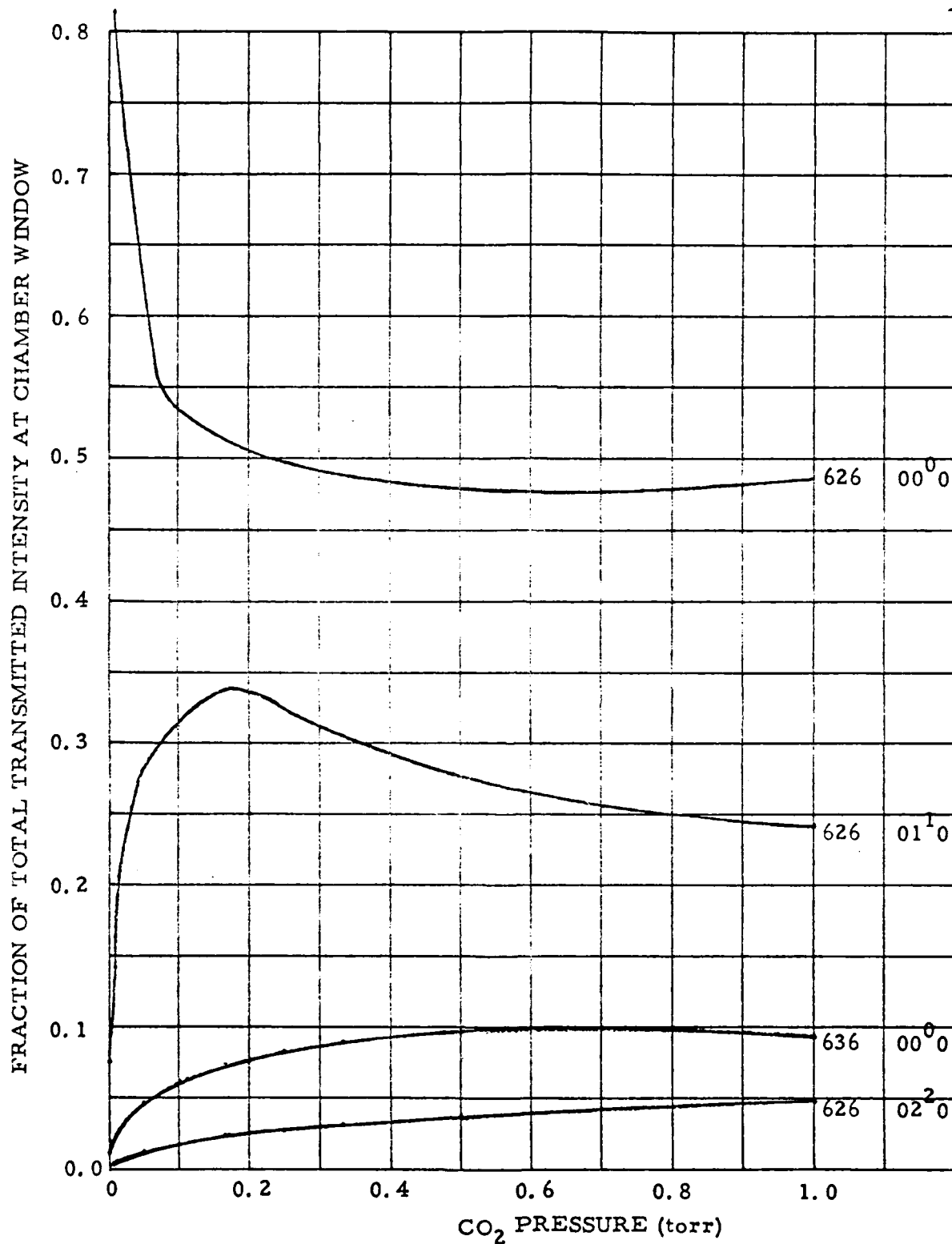


Fig. 9. Relative contributions of four of the strongest bands to the total transmitted intensity at the chamber window as a function of CO₂ pressure. $P_{Ar} = 9$ torr, $L = 11$ cm.

band transition is greatly enhanced relative to its unattenuated value, comprising one-quarter to one-third of the total radiation over most of the pressure range. It is seen that even hot-band self-absorption becomes significant at pressures greater than 0.2 torr.

C. The Effect of Atmospheric CO₂

The absorption by ambient CO₂ present in the laboratory air in the 45 cm optical path from the window to the detector was taken into account previously² by simply modifying the experimental spectral data using a blackbody spectrum which included this atmospheric absorption feature. This correction (with 10 cm⁻¹ resolution) operated more or less uniformly on all the emitted lines. In reality, however, absorption of the fluorescence exiting the chamber window by Lorentz-broadened room air CO₂, will occur only when spectral overlap occurs. The collisional broadening of CO₂ by nitrogen has been measured¹⁰ as 0.07 cm⁻¹ atm⁻¹. Only fluorescence lines occurring within approximately an cm⁻¹ of strong atmospheric lines are significantly absorbed. Because the Voigt linewidths ($b_v \sim 2.5 \times 10^{-3}$ cm⁻¹ HWHM) of the CO₂ fluorescence are much narrower than the atmospheric lines, calculation of the atmospheric absorption of this emission is greatly simplified since the Lorentzian lineshape of the absorber does not vary significantly over the width of the Voigt line. Indeed at the off-line center frequency corresponding to the maximum slope of the Lorentz lineshape, k_v for the Lorentz line changes by about 1% over the frequency range corresponding to 8 b_v (1% intensity points of the Voigt profile).

Consequently, the emission lines may be considered as delta functions in frequency space, and the atmospheric absorption determined as the amount of attenuation of each emission line by all absorbing atmospheric transitions. The effects of overlapping lines and non-resonant absorption may be included in this rigorous (Hi-tran) calculation. Although the dominant

atmospheric absorbing transition is the 626 fundamental, the first hot band and 636 fundamental transitions make significant contributions to the absorption. Inclusion of the remaining 10 atmospheric CO₂ absorption bands in Table I produced a negligible effect on the predictions. The appropriate rotational line strengths and shapes were used in the calculation for each CO₂ transition. The Lorentz broadened lineshape is given by

$$k_v = k_{v_o} \frac{b_c^2}{(\nu - \nu_o)^2 + b_c^2} \quad (34)$$

where k_{v_o} is the line center absorption coefficient

$$k_{v_o} = \frac{S}{\pi b_c} \quad (35)$$

If the concentration of atmospheric CO₂ is taken as the standard mixing ratio (0.033%), the resultant optical path column density is $3.5 \times 10^{17} \text{ cm}^{-2}$.

Atmospheric attenuation of the fluorescence was calculated for this column density over a range of CO₂ chamber pressures. The total transmitted intensity (W/molecule-cm) for all rotational lines of all the CO₂ ν_3 vibrational bands is plotted as the lower solid line in Fig. 7. This curve includes the effects on the emission of self-absorption by Voigt broadened lines in the chamber (upper solid line) and the subsequent atmospheric CO₂ attenuation, and thus represents the prediction of radiation per molecule which will reach the detector. The atmospheric attenuation is a relatively constant factor of two over most of the chamber CO₂ pressure range considered. Furthermore the predicted intensity per molecule reaching the detector varies by less than a factor of five over the chamber CO₂ pressure range 0 - 1 torr.

Relative contributions of the three strongest bands to the total predicted intensity at the detector is plotted in Fig. 10 over the range 0.0 - 0.5 torr CO₂ pressure. The 626 fundamental radiation is severely attenuated over the 45 cm optical path in the room; so much so, that the hot band (which has a band strength which is only 8% of the fundamental's) is the dominant contributor to the total radiation intensity at nearly all CO₂ pressures considered. Comparison of Figs. 9 and 10 illustrates this effect clearly. Even the 636 isotope fundamental transition will be responsible for more of the total transmitted radiation than the 626 fundamental at pressures above 0.3 torr.

Figure 10 is basically similar to the analogous Doppler predictions performed previously² which did not take into account atmospheric CO₂ attenuation. It may be seen from Fig. 7 that the previous predicted total intensity for Doppler lines differs by less than 50% from the present more rigorous calculation over all but the lowest pressures considered. Figure 7 provides proof of the previous conjecture that the effects of Voigt absorbers and ambient CO₂ would be offsetting, and that Doppler profile predictions provided a reasonable estimate of the total transmitted radiation.

The above transmission predictions are based on the CO₂ concentration in the optical path being equal to the standard atmospheric mixing ratio. In an attempt to minimize the effects of atmospheric CO₂, efforts were made to purge the optical path of CO₂. The degree of success will be evaluated later from spectral shape predictions and blackbody absorption features.

The effect of changes in the atmospheric CO₂ concentration on the total transmitted intensity predictions is shown in Fig. 11. The fraction of chamber window fluorescence transmitted to the detector is plotted as a function of chamber CO₂ pressure for a number of atmospheric CO₂ concentrations over the range 33 - 660 ppm. (The standard atmospheric mixing ratio is 330 ppm.) Note that at the lower test chamber CO₂ pressures, the

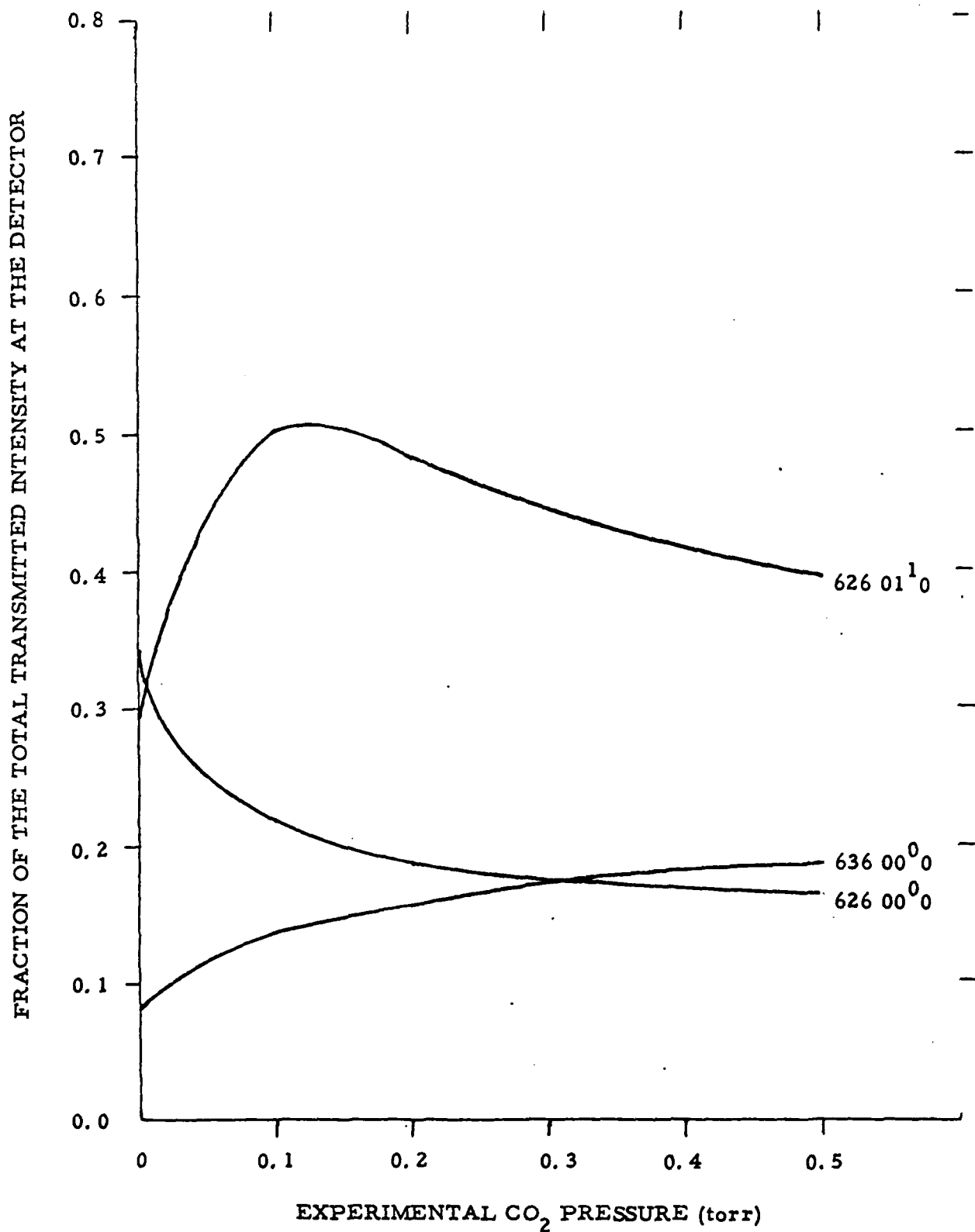


Fig. 10. Relative contributions of the three strongest bands to the total transmitted intensity after attenuation by both chamber and atmospheric CO₂, plotted as a function of chamber CO₂ pressure.

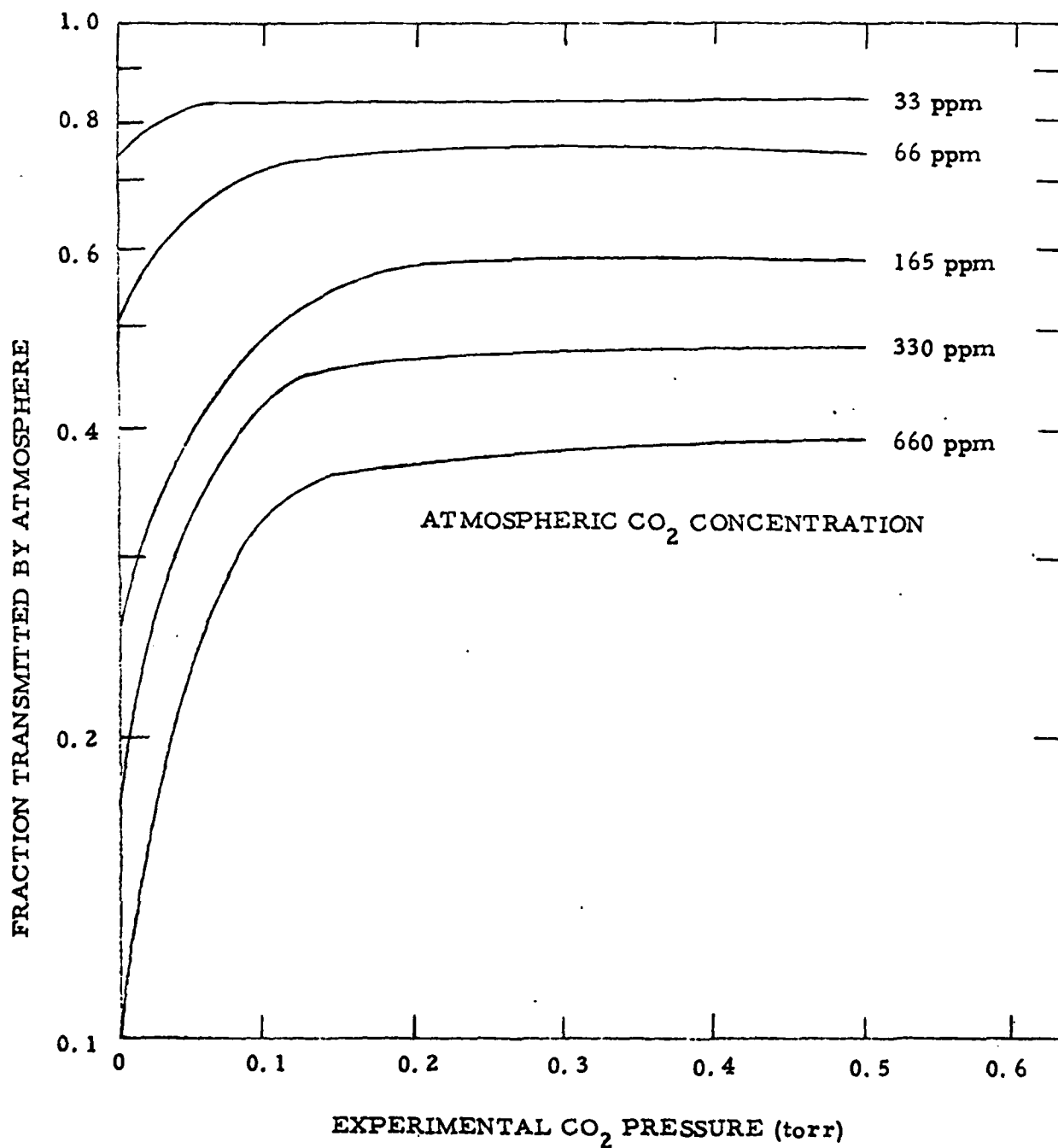


Fig. 11. The fraction of the total CO₂ fluorescence at the chamber window transmitted through an atmospheric pressure optical path containing various concentrations of CO₂ plotted as a function of the experimental CO₂ pressure.

chamber window fluorescence is dominated by the 626 fundamental radiation, which is severely resonantly absorbed by the atmospheric CO₂. As a result, the fractional transmission of the chamber window fluorescence is lowest for this extreme. Nonetheless for CO₂ pressures > 0.1 torr the fractional transmission varies by only a factor of 2 - 2.5 over the full range of atmospheric CO₂ concentrations shown and also the total additional attenuation is less than a factor of three. The total intensity incident on the detector (W/molecule-str) for a given atmospheric CO₂ pressure is calculated as the product of the attenuation of Fig. 11 and the Voigt chamber window predictions of Fig. 7.

D. Comparison With the Data Base

In order to permit comparison with the experimental spectra, the individual transmitted line intensities must be convolved with a system slit function, $g(\nu, \nu')$. The appropriate function for the LABCEDE interferometric detection system is a sinc function defined by

$$g(\nu, \nu') = \frac{0.82 \Delta\nu}{\pi |\nu - \nu'|} \sin \left(\frac{\pi(\nu - \nu')}{0.82 \Delta\nu} \right) \quad (36)$$

which determines the contribution at frequency ν from a line at frequency ν' for a system resolution $\Delta\nu$. For all experimental runs sufficient interferogram points were taken to yield 10 cm⁻¹ resolution spectra. Because the fluorescence lines are much narrower than the system resolution, only their line center separation from the convolution frequency is required. The sinc function is truncated at the second zero crossing on each side of the center frequency. All the transmission predictions for the individual ν_3 band transitions (either at the chamber window or at the detector) were sorted by frequency, summed in 0.4 cm⁻¹ cells and convolved with the sinc function to yield a predicted spectrum for comparison with the experimental data.

Spectra from sixteen runs were included in the analysis. The relevant experimental parameters for these runs are listed in Table II. The CO_2 pressures of these runs were kept in the 0.1 - 0.2 torr range in order to permit observation of CO relaxation kinetics (see Section IV). The observed CO_2 fluorescence near beam termination from a slowly purged runs is shown in Fig. 12. The dominant spectral feature is the broad peak at $\sim 2310 \text{ cm}^{-1}$ with a shoulder at slightly higher frequency. A second strong feature at 2350 cm^{-1} and the smaller peak at $\sim 2380 \text{ cm}^{-1}$ were also very reproducible from run to run. The shape of the broad feature centered at 2270 cm^{-1} varies from run to run, but its relative intensity remained constant.

The CO_2 fluorescence spectra for four runs with very similar experimental and purge conditions (11MAR2, 16MAR2, 16MAR3, and 16MAR4) are all plotted in Fig. 13 normalized to the peak of the 2310 cm^{-1} feature to demonstrate data reproducibility. For comparison, the chamber window fluorescence predictions for Voigt broadened lines are shown in Fig. 14 - 17 for experimental CO_2 pressures of 0.33, 0.2, 0.10 torr and trace amount of CO_2 respectively. It can be seen by comparison with Fig. 12 that the Voigt predictions without atmospheric attenuation are very different from the data. Figure 17 corresponds to the prediction for the case of an optically thin gas, i. e., no self absorption. In this case, the spectrum is primarily due to the P and R branches of the 626 fundamental ν_3 transition. As the absorber concentration increases, other transitions contribute significantly to the spectrum as shown in Fig. 9. The broken line curve in Fig. 14 represents the predicted spectrum when only the 626 fundamental transition is included in the calculation, clearly demonstrating that the hot band and isotopic radiation occurs at lower wavenumbers (to the red of the fundamental).

The corresponding spectral predictions, which include the effect of atmospheric CO_2 attenuation, are displayed in Fig. 18 - 21. For these

TABLE II
RUNS INCLUDED IN CO₂ SPECTRAL ANALYSIS

Date	CO ₂ Pressure (torr)	Ar Pressure (torr)	Voltage (kV)	Current (ma)	Optical Path Purging
10 Feb (1)	0.25	9.1	30	0.6	Slow flow
9 Mar (1)	0.1	9.0	30	0.59	Very fast flow
11 Mar (1)	0.2	9.1	30	0.67	Slow flow
11 Mar (2)	0.1	9.1	30	0.81	Slow flow
16 Mar (1)	0.2	8.9	30	0.84	Slow flow
16 Mar (2)	0.1	9.0	30	0.84	Slow flow
16 Mar (3)	0.1	9.0	30	0.78	Slow flow
16 Mar (4)	0.1	9.0	30	0.79	Slow flow
16 Mar (5)	0.2	11.0	40	1.26	Slow flow
16 Mar (6)	0.1	11.0	40	1.26	Slow flow
28 Mar (2)	0.3	49.7	30	0.52	Slow flow
5 Apr (2)	0.1	11.0	40	1.1	None
14 Apr (3)	0.1	9.0	30	0.8	None
18 Apr (1)	0.2	9.3	30	0.73	None
18 Apr (2)	0.3	49.7	40	0.86	None
18 Apr (3)	0.2	85.5	40	0.83	None

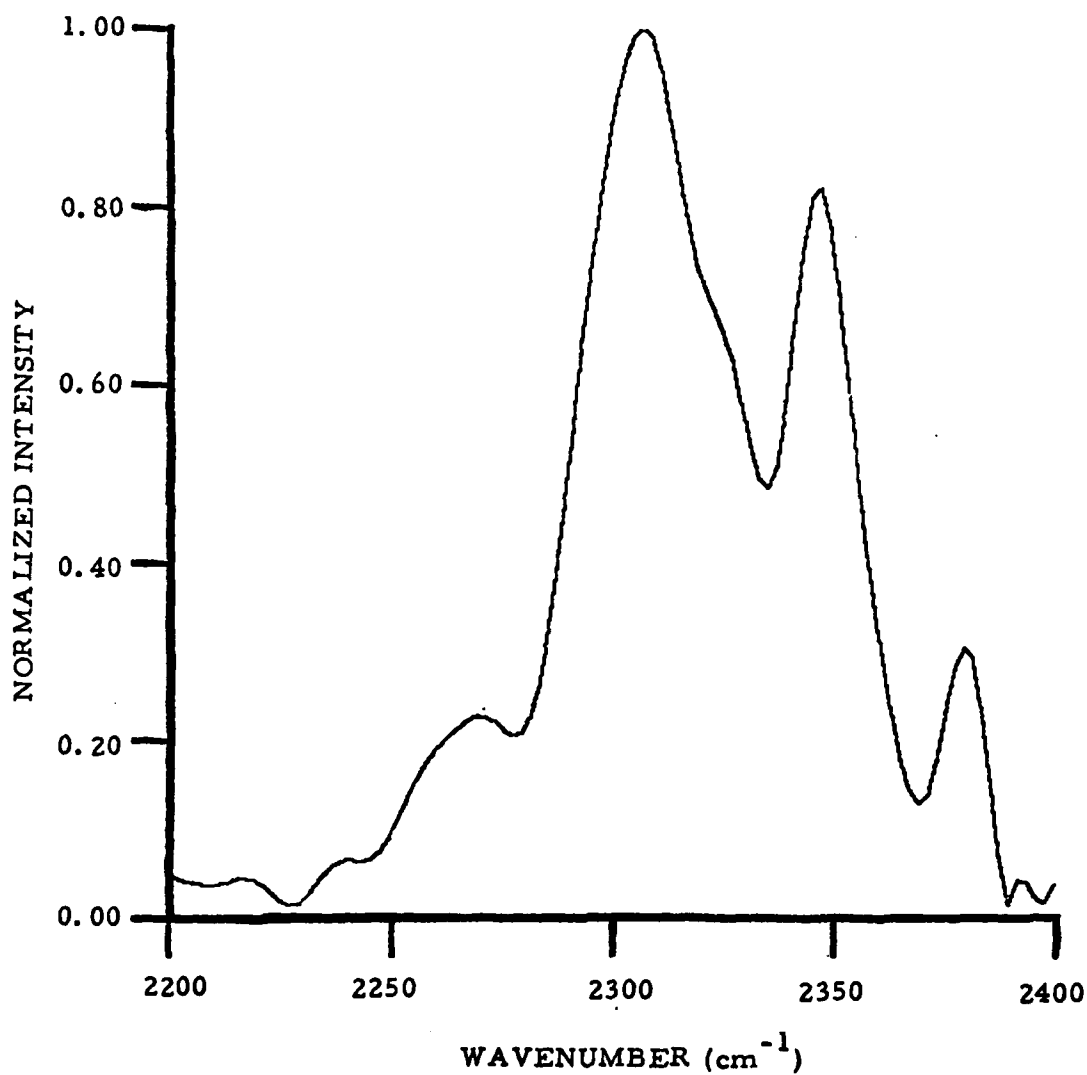


Fig. 12 Normalized experimental data from 11 MARCH RUN 2, 0.1 msec before beam termination. $P_{\text{CO}_2} = 0.1$ torr, $P_{\text{Ar}} = 9.1$ torr, $I = 0.81$ mA, $V = 30$ kV. Maximum intensity = 3.7×10^{-6} W/str-cm⁻¹.

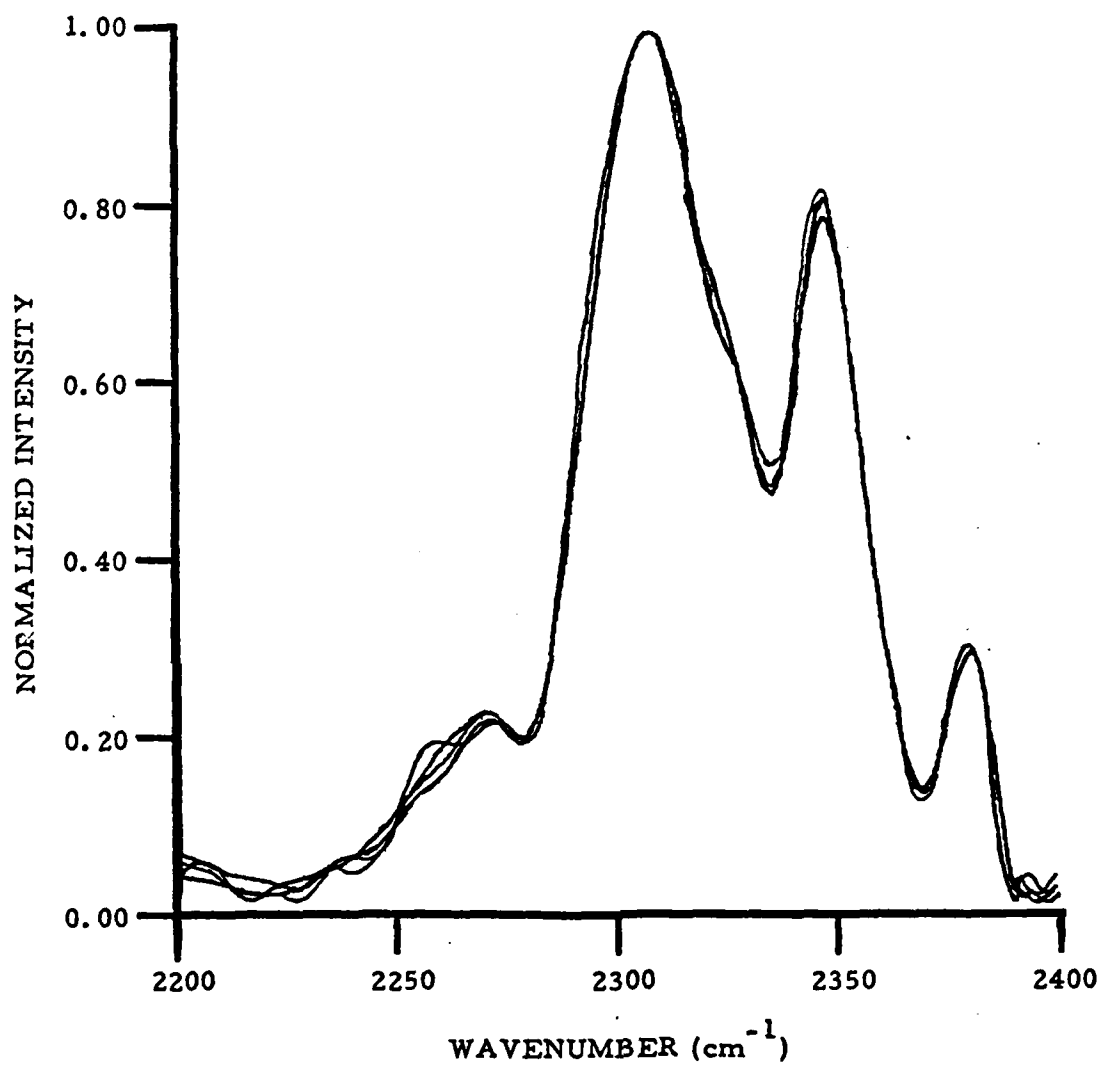


Fig. 13 Data from 11 MARCH RUN 2, 16 MARCH RUN 2, 16 MARCH RUN 3, and 16 MARCH RUN 4, 0.1 msec before beam termination, normalized to the same scale. $P_{\text{CO}_2} = 0.1$ torr, $P_{\text{Ar}} = 9$ torr, $I = 0.81 \pm 0.03$ mA, $V = 30$ kV.

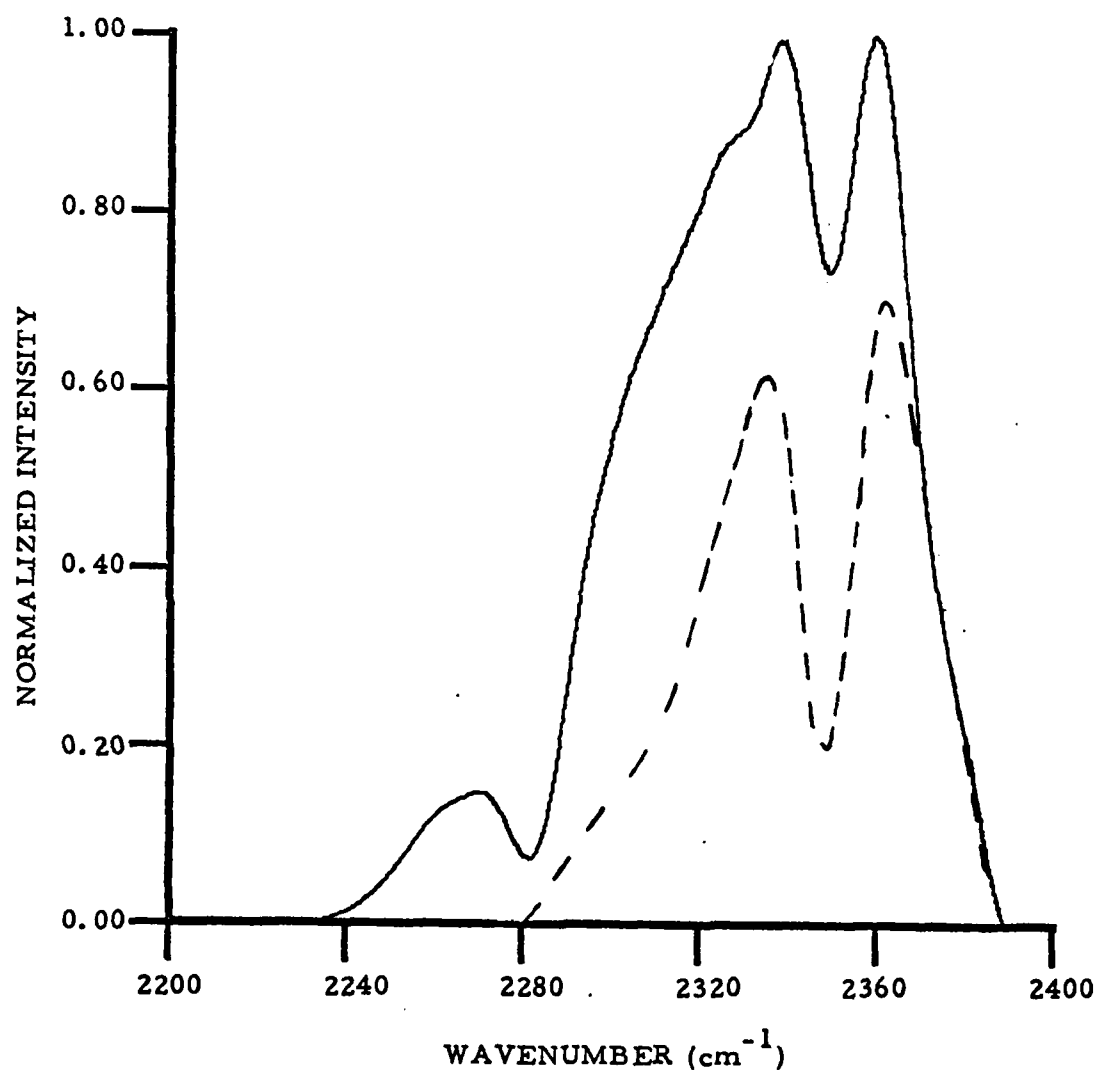


Fig. 14 Predicted fluorescence spectrum transmitted to the chamber window through Voigt broadened absorption lines. Resolution is 10 cm^{-1} . $P_{\text{CO}_2} = 0.33 \text{ torr}$. Broken curve is predicted fluorescence when only the 626 fundamental is included in the calculation. Maximum intensity = $2.28 \times 10^{-26} \text{ W/molecule-str-cm}^{-1}$.

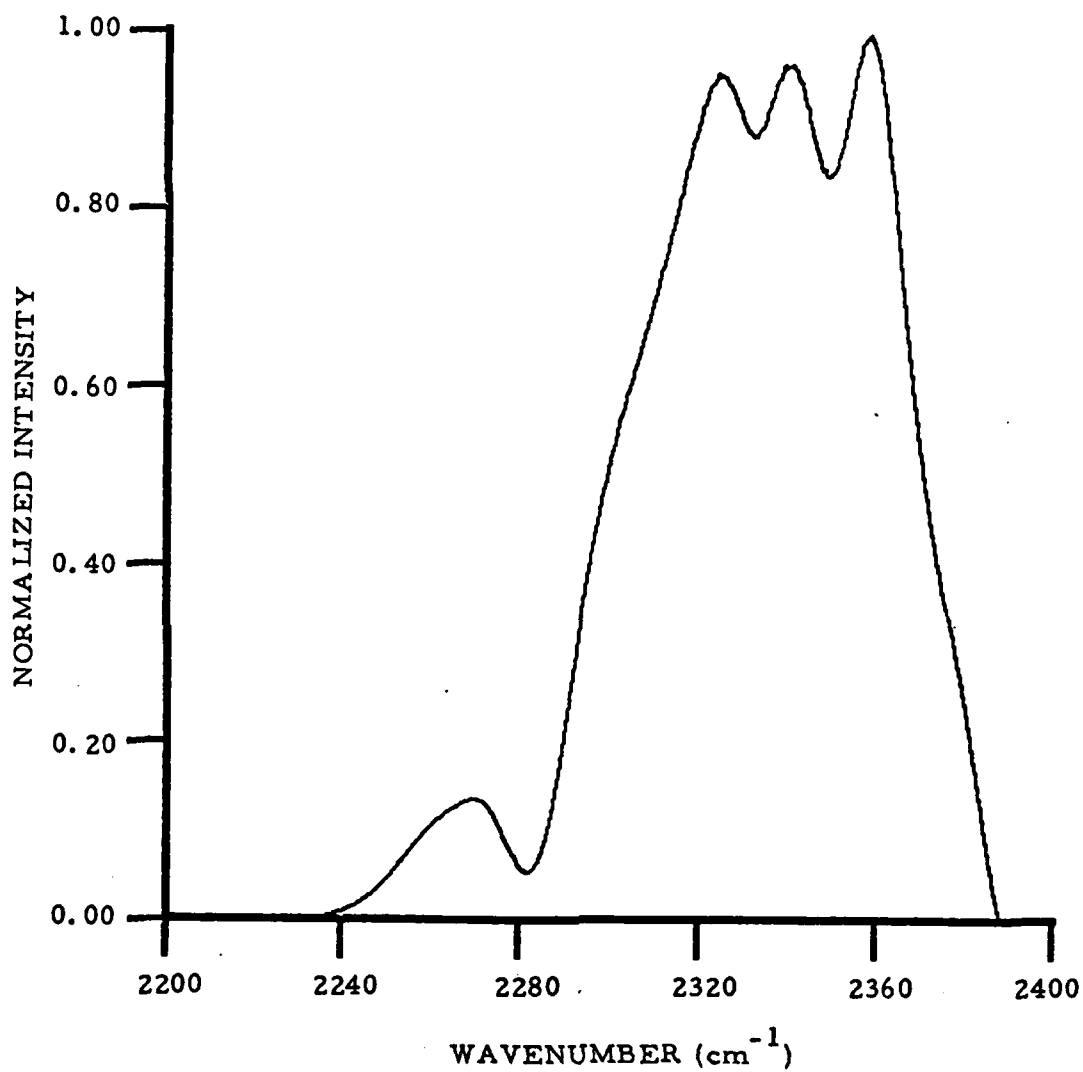


Fig. 15 Predicted fluorescence at chamber windows for Voigt lines with 10 cm^{-1} resolution. $P_{\text{CO}_2} = 0.20$ torr. Maximum intensity = $2.91 \times 10^{-26} \text{ W/molecule-str-cm}^{-1}$.

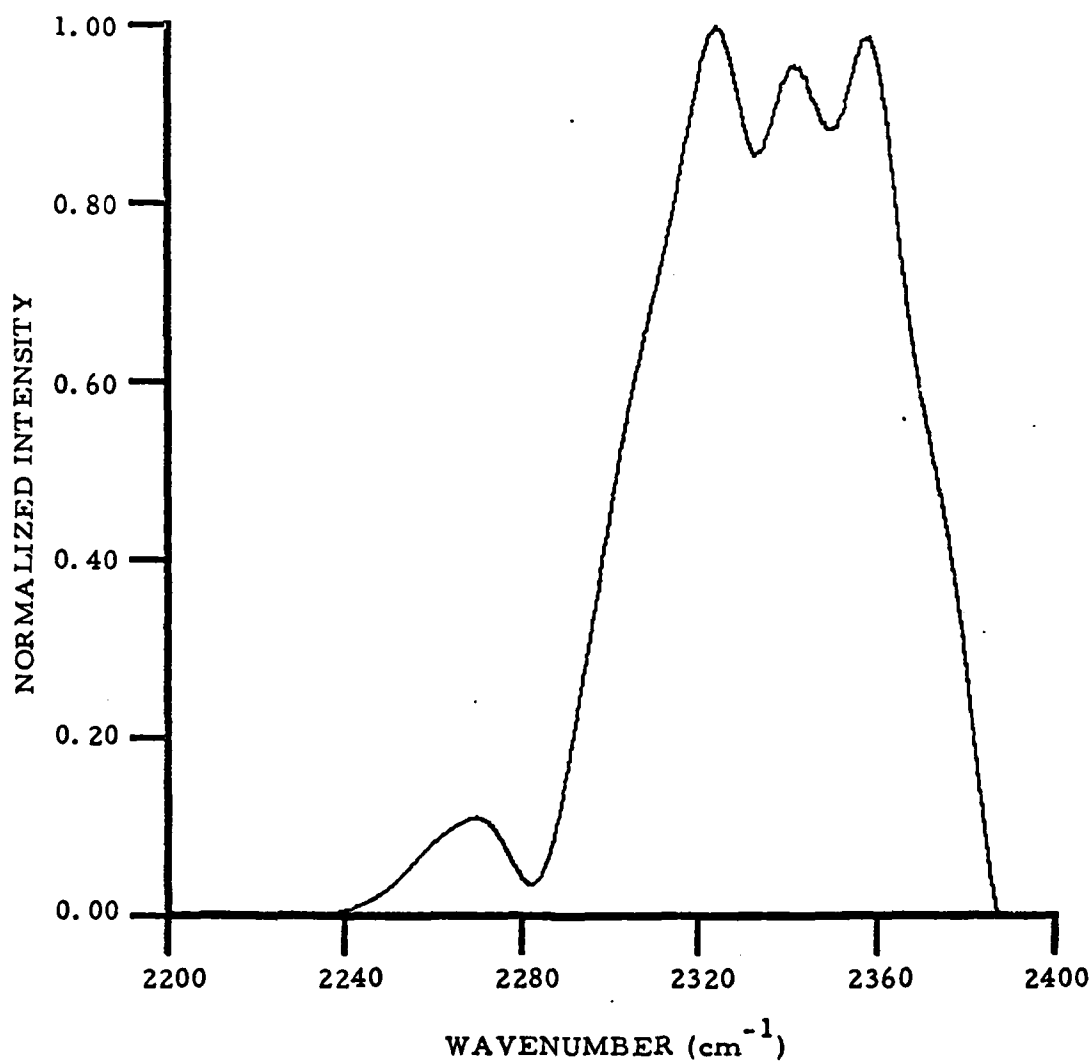


Fig. 16 Predicted fluorescence at chamber window for Voigt lines with 10 cm^{-1} resolution. $P_{\text{CO}_2} = 0.10 \text{ torr}$. Maximum intensity = $4.01 \times 10^{-26} \text{ W/molecule-str-cm}^{-1}$.

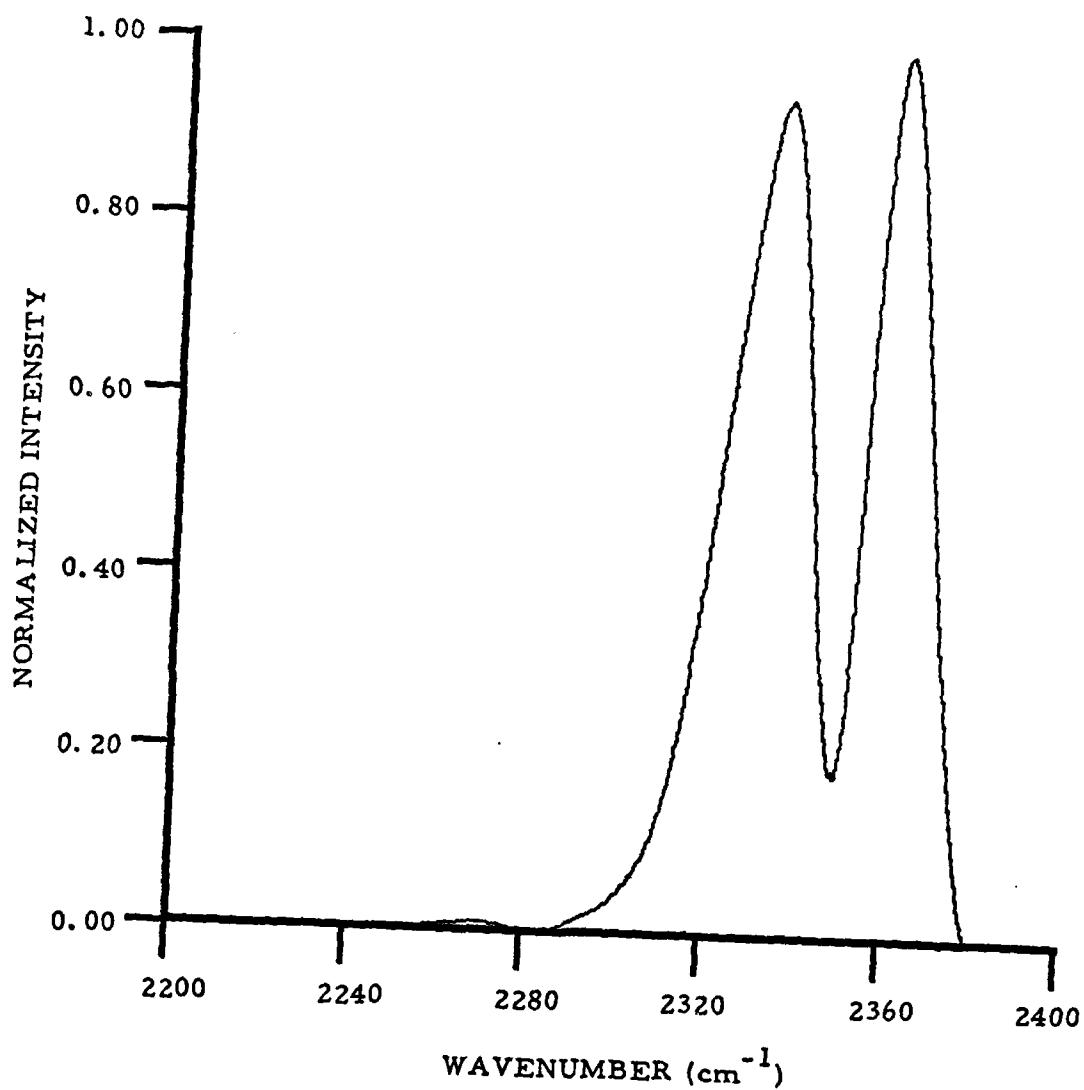


Fig. 17 Predicted fluorescence at chamber window for Voigt lines with 10 cm⁻¹ resolution. Trace amount of CO₂. Maximum intensity = 4.39×10^{-25} W/molecule-str-cm⁻¹.

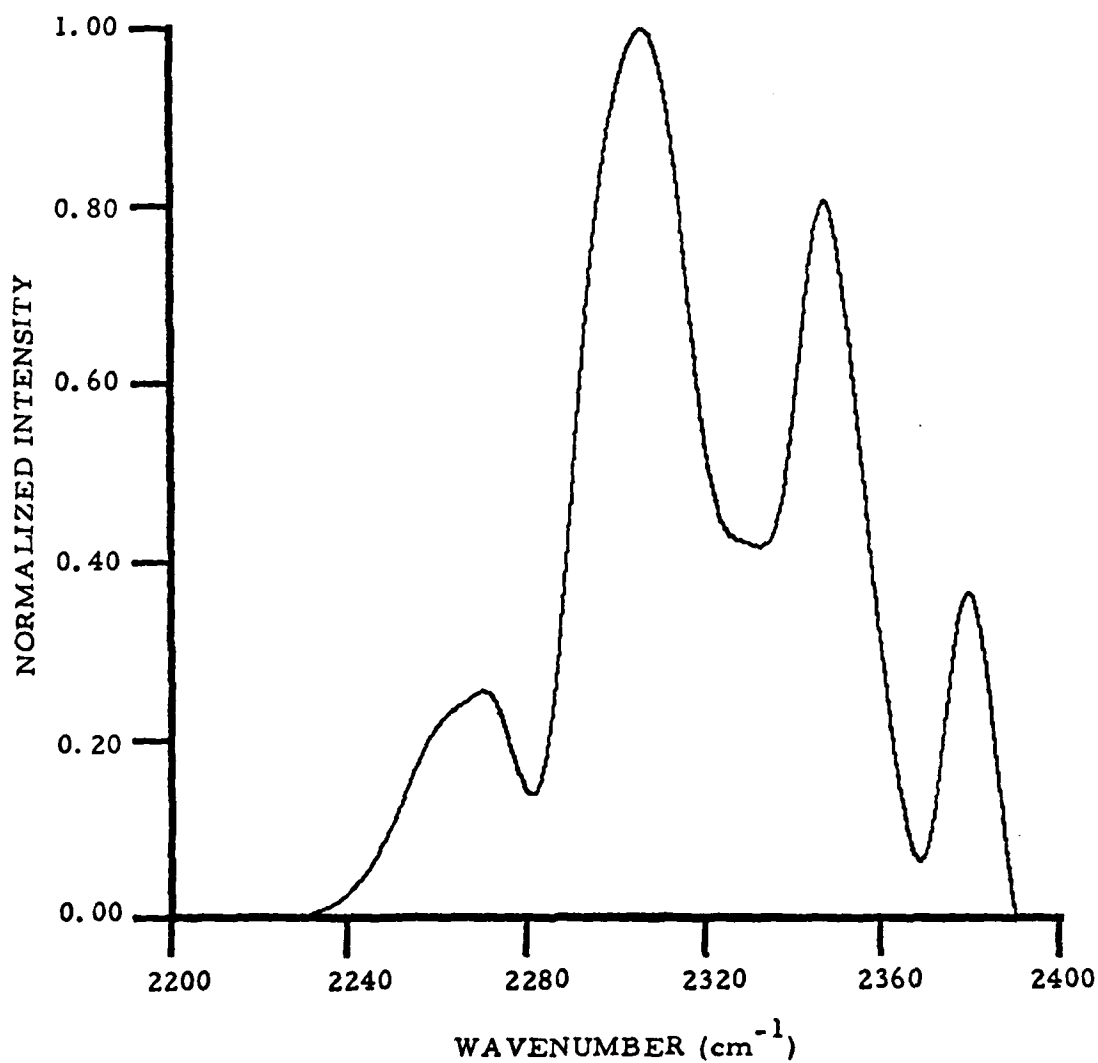


Fig. 18 Predicted fluorescence spectrum at the detector after transmission through chamber and atmospheric absorbers. Resolution = 10 cm^{-1} . $P_{\text{CO}_2} = 0.33 \text{ torr}$. Maximum intensity = $1.25 \times 10^{-26} \text{ W/molecule-str-cm}^{-1}$.

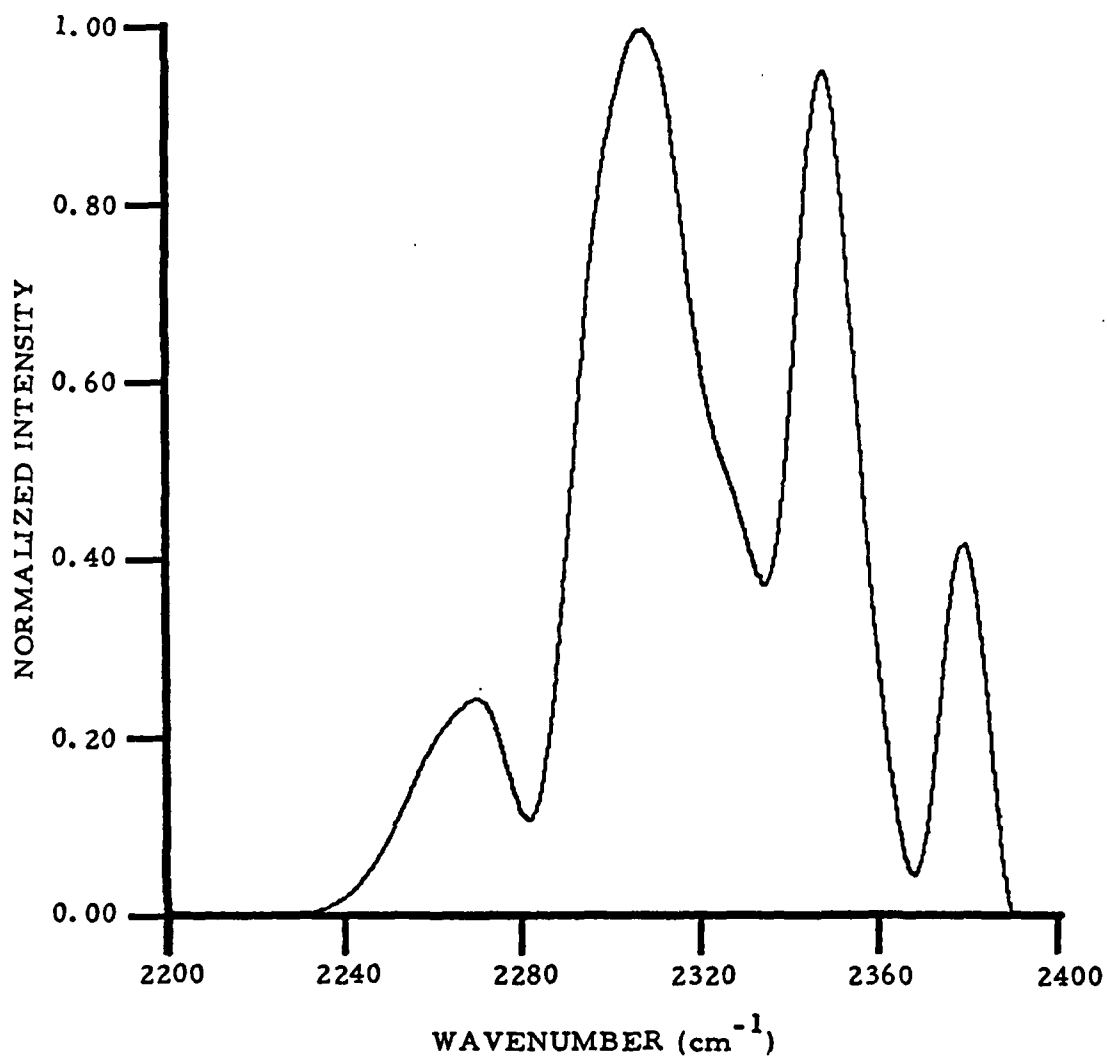


Fig. 19 Predicted spectrum at detector including effects of both chamber and atmospheric absorbers. Resolution = 10 cm^{-1} . $P_{\text{CO}_2} = 0.2 \text{ torr}$. Maximum intensity = $1.54 \times 10^{-26} \text{ W/molecule-str-cm}^{-1}$.

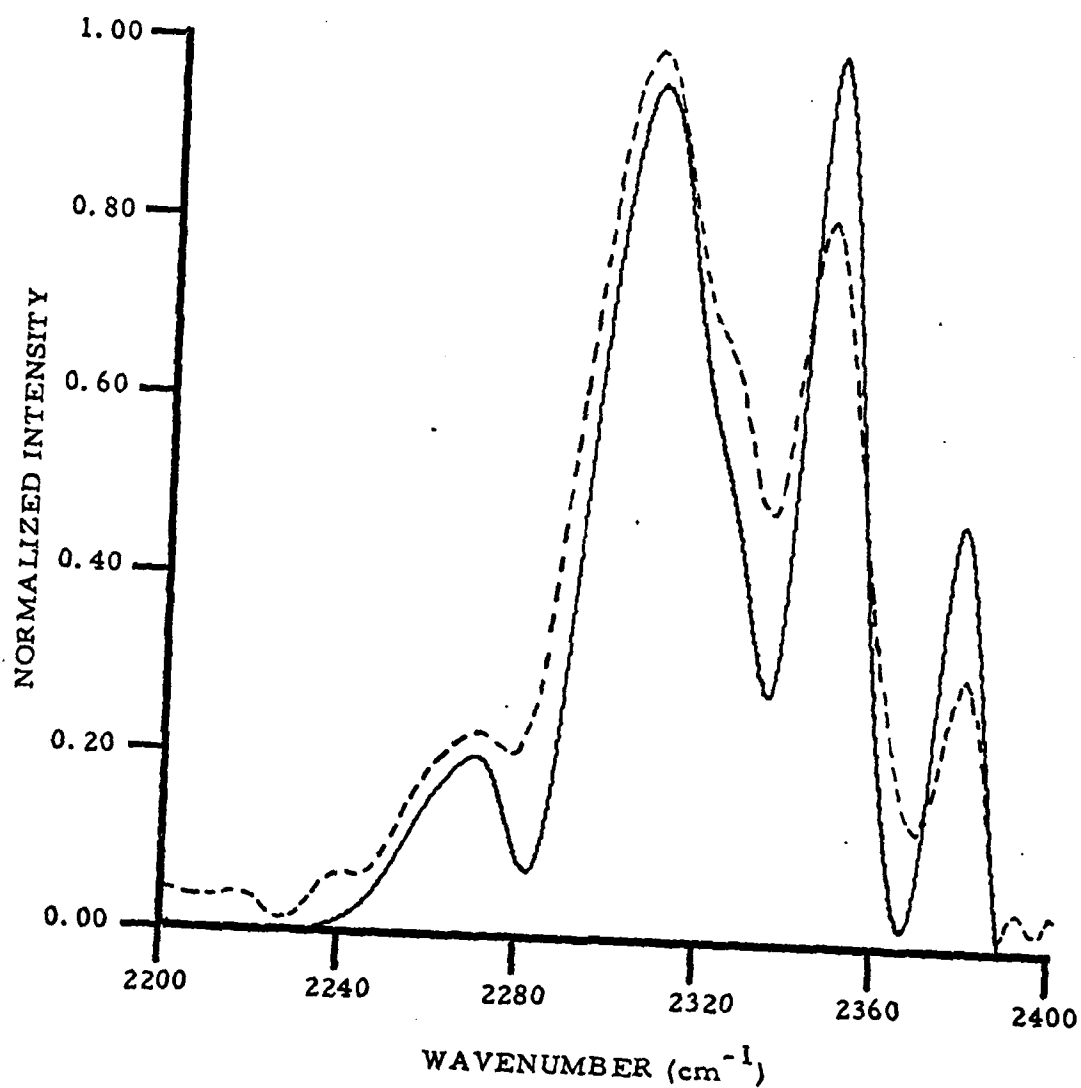


Fig. 20 Predicted spectrum at detector including effects of both chamber and atmospheric absorbers. Resolution is 10 cm^{-1} . $P_{\text{CO}_2} = 0.1 \text{ torr}$. Broken line is experimental data of 11 MARCH RUN 2. Maximum intensity = $2.09 \times 10^{-26} \text{ W/molecule-str-cm}^{-1}$.

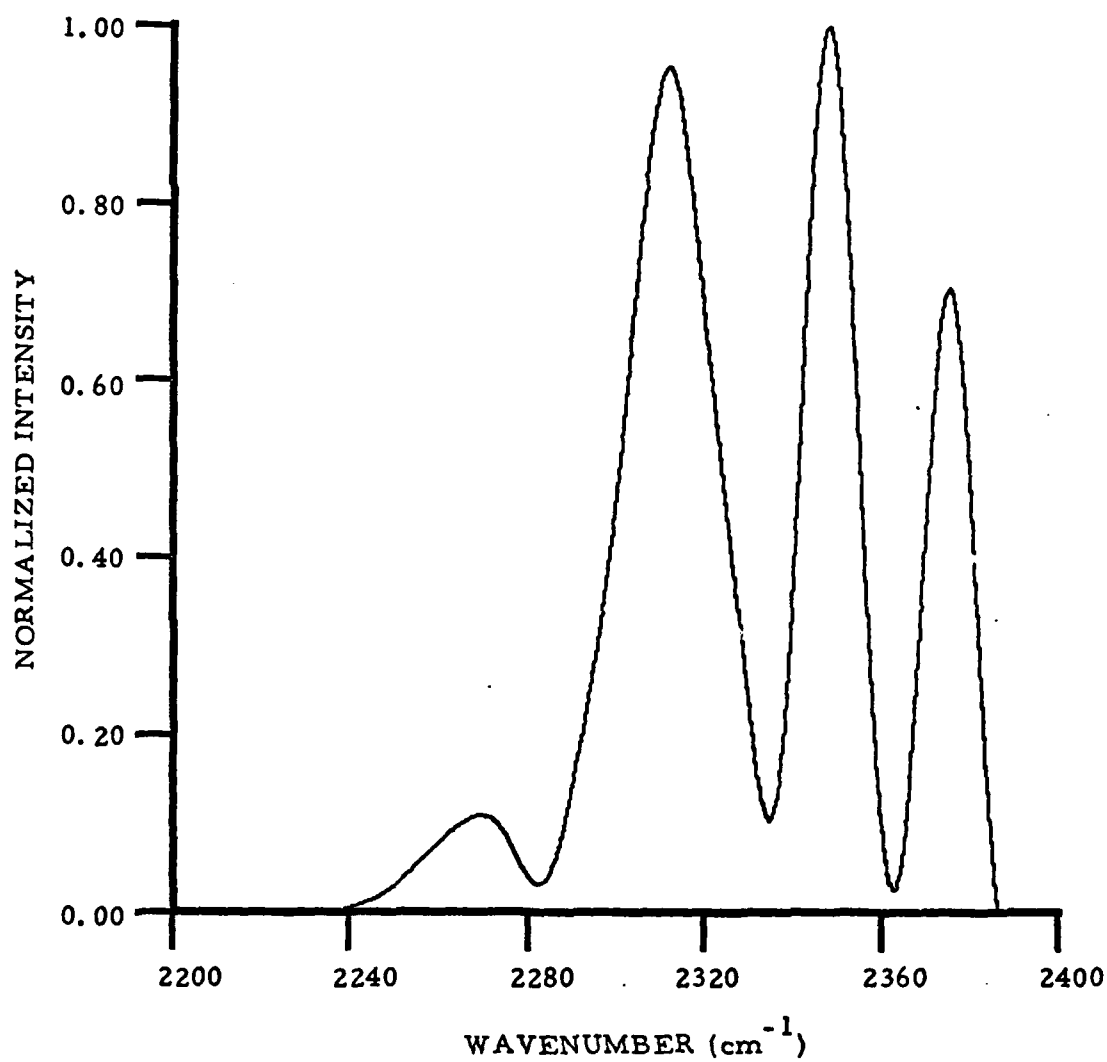


Fig. 21 Predicted spectrum at detector including effects of both chamber and atmospheric absorbers. Resolution = 10 cm⁻¹. Trace amount of CO₂. Maximum intensity = 4.36×10^{-26} W/molecule-str-cm⁻¹.

predictions the atmospheric mixing ratio of 0.033% was assumed. All spectral shapes are greatly modified from those shown in Figs. 14 - 17 even though the total transmitted intensity (W/molecule-str) changes by less than a factor of 3 for the 0.1, 0.2, and 0.33 torr cases. Note that a large fraction of the transmitted intensity occurs in the hot band and isotope emission region as predicted in Fig. 11. The predictions of Figs. 19 and 20 are very similar in appearance to the data of Fig. 12, which has been reproduced in Fig. 20 as a broken line curve. The frequencies and shapes of all spectral features are matched very well, although the relative intensity of these features are not predicted as well.

Because the optical path was being purged, the amount of atmospheric CO₂ present was uncertain. Consequently, the amount of CO₂ included in the predictions was varied in an attempt to better match the spectral data. Predicted spectra for the case of 0.1 torr CO₂ chamber pressure and a range of atmospheric CO₂ concentrations are displayed in Fig. 22. Both the relative spectral intensity and the shape of the predicted radiation change over this range. Most notably the $\sim 2310\text{ cm}^{-1}$ feature increases in relative intensity, narrows, and shifts to the red as the ambient CO₂ concentration is increased. The best spectral fit was determined to occur when the atmospheric CO₂ concentration was taken to be 0.9 that of the standard mixing ratio, 300 ppm. A comparison of the prediction for this mixing ratio and the experimental spectra of Fig. 12 are shown in Fig. 23. The position of the peak and shoulder of the 2310 cm^{-1} feature are well matched but the intensity of the shoulder is underestimated. The two peaks at high wavenumbers are still overestimated. These peaks occur in regions where the spectral line density of rotational lines of many different

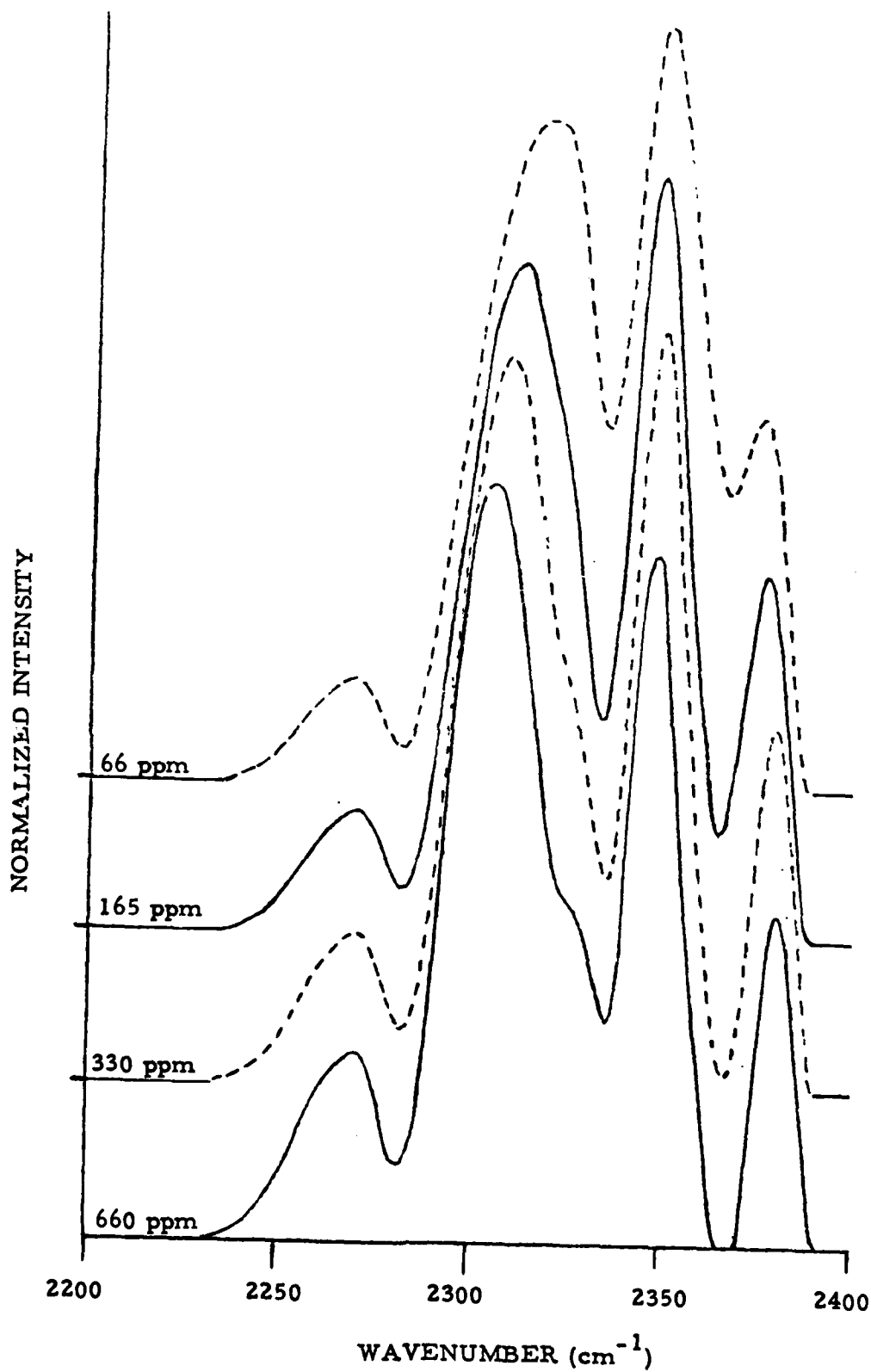


Fig. 22. Some predicted spectra at the detector for a range of atmospheric CO_2 concentrations. Experimental CO_2 pressure is 0.1 Torr. The standard atmospheric mixing ratio is 330 ppm.

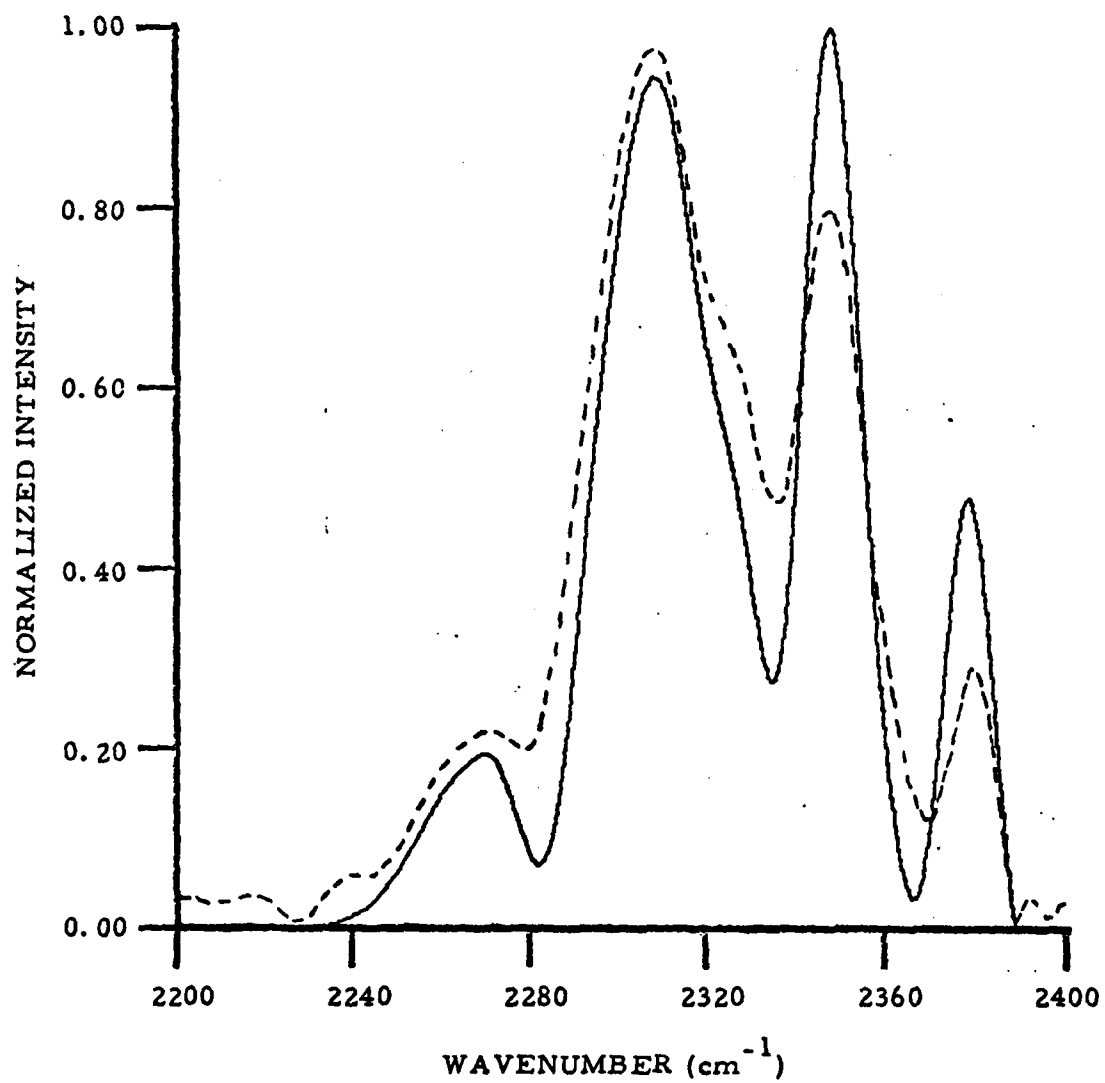


Fig. 23 Comparison of data (broken line) with prediction for 0.1 torr chamber pressure of CO₂ and atmospheric CO₂ concentration of 300 ppm.

vibrational bands is great and significant self absorption is occurring (compare with Fig. 17). A possible explanation for the overprediction of the spectral intensity in these regions might be the breakdown of the non-overlapping line approximation used in calculating the Voigt profile transmission. If significant overlap were occurring the inclusion of non-resonant absorption would result in a reduction of the predicted transmitted intensity in these regions.

Experimental data taken with nominally 0.2 torr CO_2 present in the chamber is compared in Fig. 24 with a prediction using 0.2 torr CO_2 chamber pressure and 300 ppm atmospheric concentration. Again, agreement is excellent except for the intensity of the 2350 cm^{-1} and 2380 cm^{-1} peaks. The effect of the purge under very fast flow conditions is seen in Fig. 25 where data from the 9MAR1 run is displayed. (Note that significant difference in the spectral shapes for slow and fast purge data, see Fig. 24.) For comparison, the predicted spectrum for the case of a 66 ppm CO_2 concentration in the optical path is also plotted in Fig. 25. The agreement between the synthetic and experimental spectra is outstanding, with only a slight underprediction of the intensity of the 2310 cm^{-1} peak. Thus, under very fast purging conditions, a significant reduction in the optical path CO_2 concentration may be achieved. The amount of CO_2 present in the chamber was taken to be 0.25 torr for the prediction; this adjustment, in addition to improving the spectral match, seems to be in agreement with the CO_2 concentration predicted from the CO relaxation data. (See Section IV.) It should be noted that even under these rapid purging conditions the transmitted spectral data does not resemble the chamber window fluorescence (compare with Fig. 14 and 15). Sufficient absorption still occurs in the atmosphere to modify the spectrum.

A spectrum from one of the runs taken without purging of the optical path (5APR2) is given in Fig. 26. The predicted spectrum (of

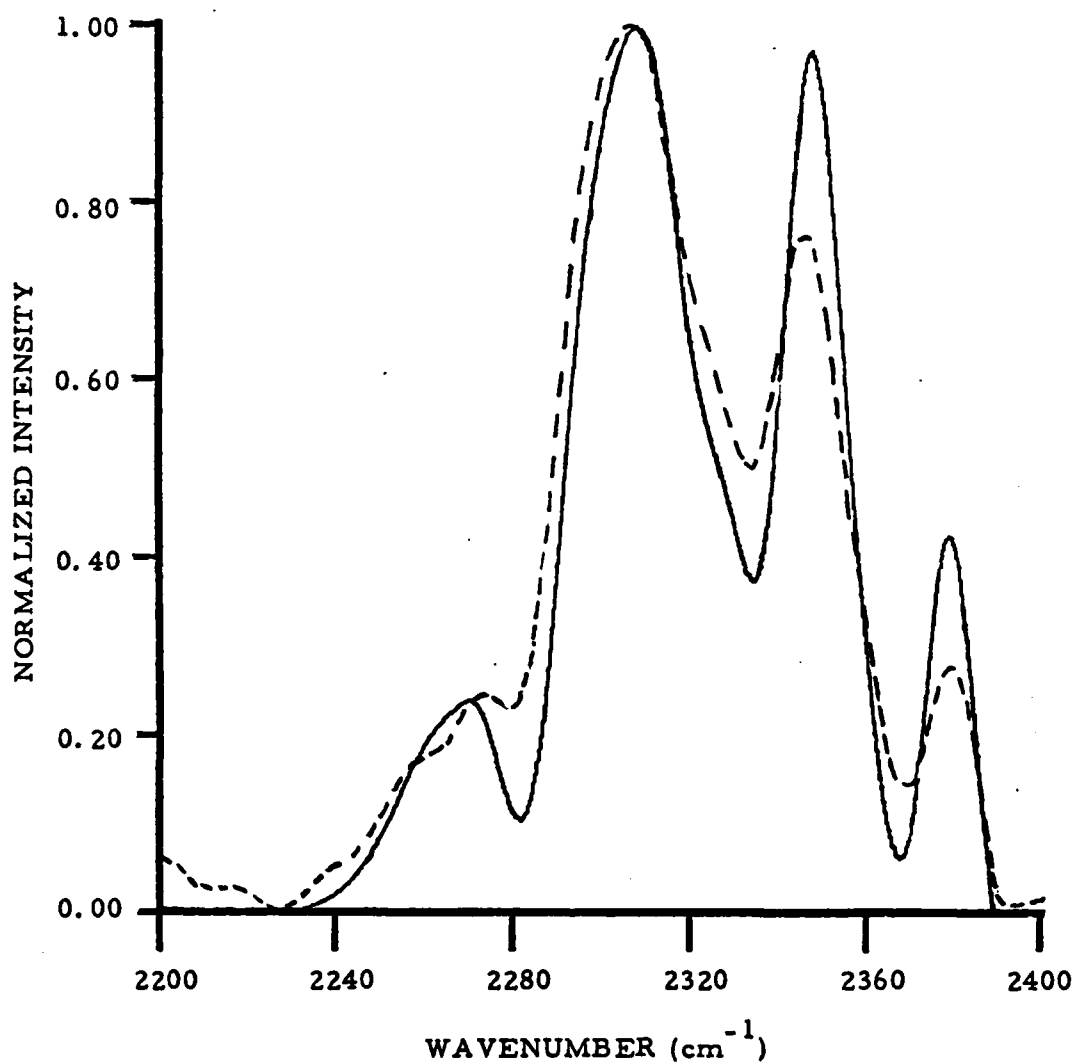


Fig. 24 Comparison of data taken 0.1 msec before beam termination with 0.2 torr CO_2 pressure (11 MARCH RUN 1) and prediction assuming the same chamber pressure and 300 ppm ambient CO_2 concentration. Data is the broken line, prediction is the solid line.

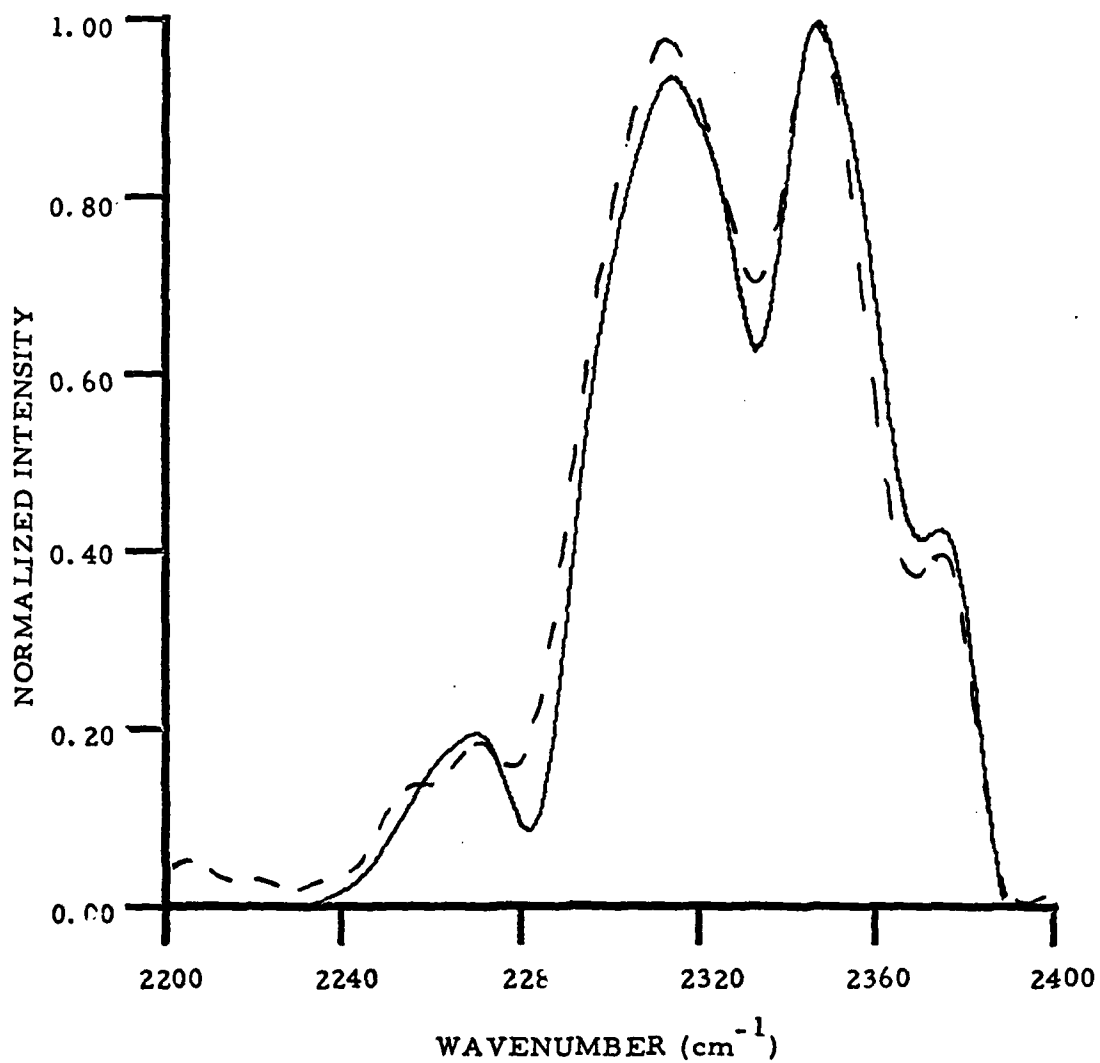


Fig. 25 Comparison of data, taken 0.1 msec before beam termination with 0.1 torr CO₂ pressure and a very fast purge, and a prediction assuming 0.25 torr CO₂ chamber pressure and 66 ppm ambient CO₂ concentration. Data is broken line, prediction is solid line.

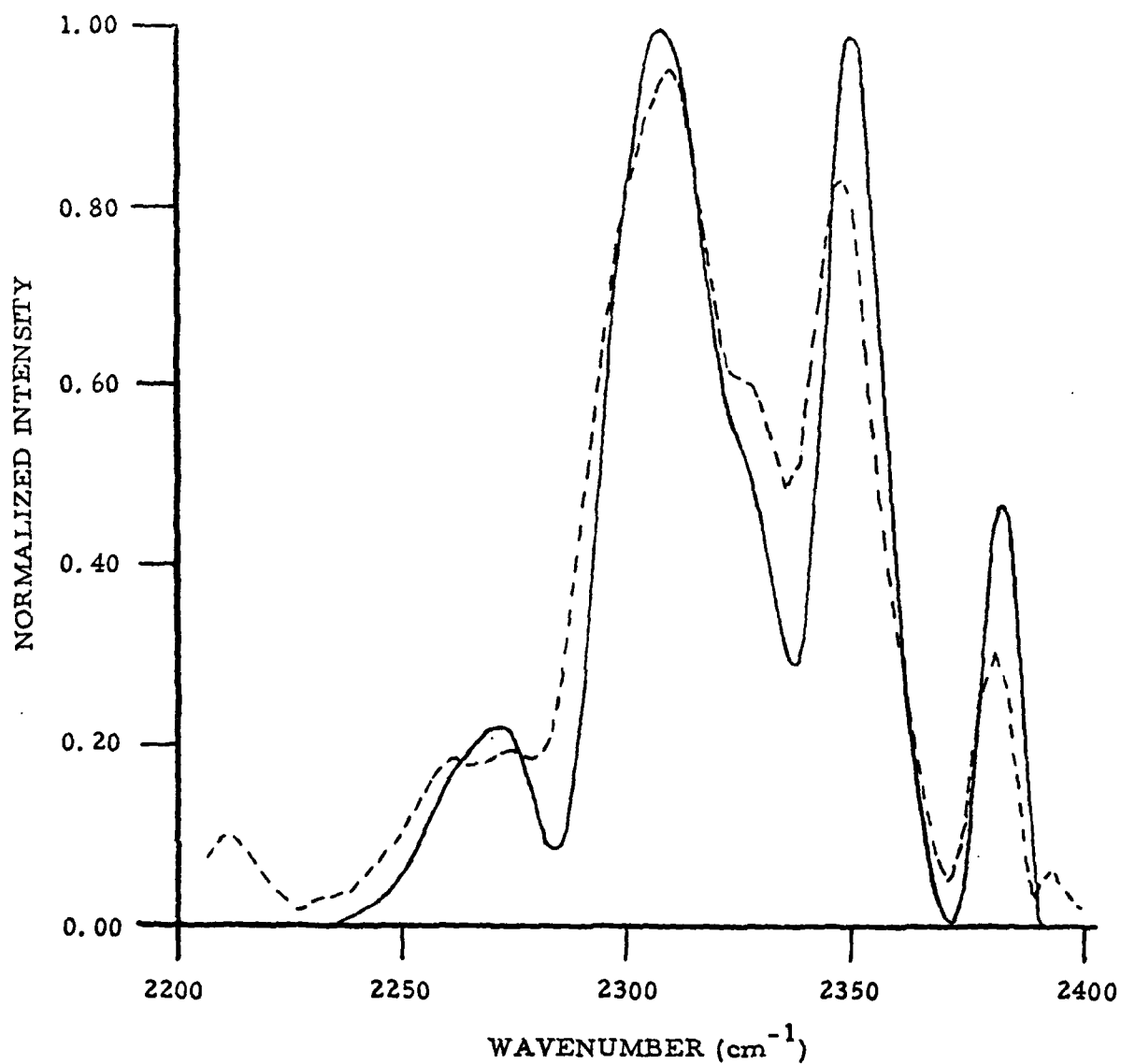


Fig. 26. Comparison of data taken 0.1 msec before beam termination with 0.1 torr CO_2 pressure and no purge (broken line) with a prediction assuming the same CO_2 pressure and 430 ppm ambient CO_2 concentration. Maximum intensity = 1.86×10^{-26} W/molecule-str-cm $^{-1}$.

0.1 torr CO₂ chamber pressure fluorescence) was found to best match the data when the atmospheric CO₂ concentration was about 1.3 times the standard mixing ratio, i. e., 430 ± 120 ppm. The predicted spectrum is presented as the solid curve in Fig. 26. Again, the frequencies of all relevant spectral features are matched, although the intensity of the 2325 cm^{-1} shoulder is underestimated. In general it is concluded that the detailed band signatures developed from the absorption modeling provide good agreement with the data base.

It is of course dangerous to rely solely on the radiation signature comparisons for determining the ambient CO₂ concentrations. Therefore a consistency check was performed using the blackbody transmission spectra taken daily with the data. To perform these calibration runs, the entire interferometer had to be rotated so that the blackbody radiator could be positioned at a distance equal to that between the chamber window and the entrance aperture of the interferometer (equalizing absorption path lengths). While rotating the interferometer, the end of the purged path was open to the room air, and additionally, due to the blackbody aperturing system, there was a 5 cm distance at the blackbody which is unpurged. As a result, for runs with a purging flow, the amount of CO₂ present in the optical path during the calibration run is felt to be at best intermediate between the true purged and atmospheric values. The CO₂ absorption feature in the blackbody spectrum is shown in Fig. 27. There was no attempt at optical path purging for this run.

In order to generate a synthetic absorption feature to compare with the calibration, a calculation of the absorption of radiation by each rotational line of the three strongest CO₂ bands of Table I was performed at frequency intervals smaller than the atmospheric CO₂ linewidth. Specifically, at one atmosphere, the collision broadened CO₂ HWHM is 0.07 cm^{-1} while the sampling interval was taken as 0.05 cm^{-1} . (It may be seen from

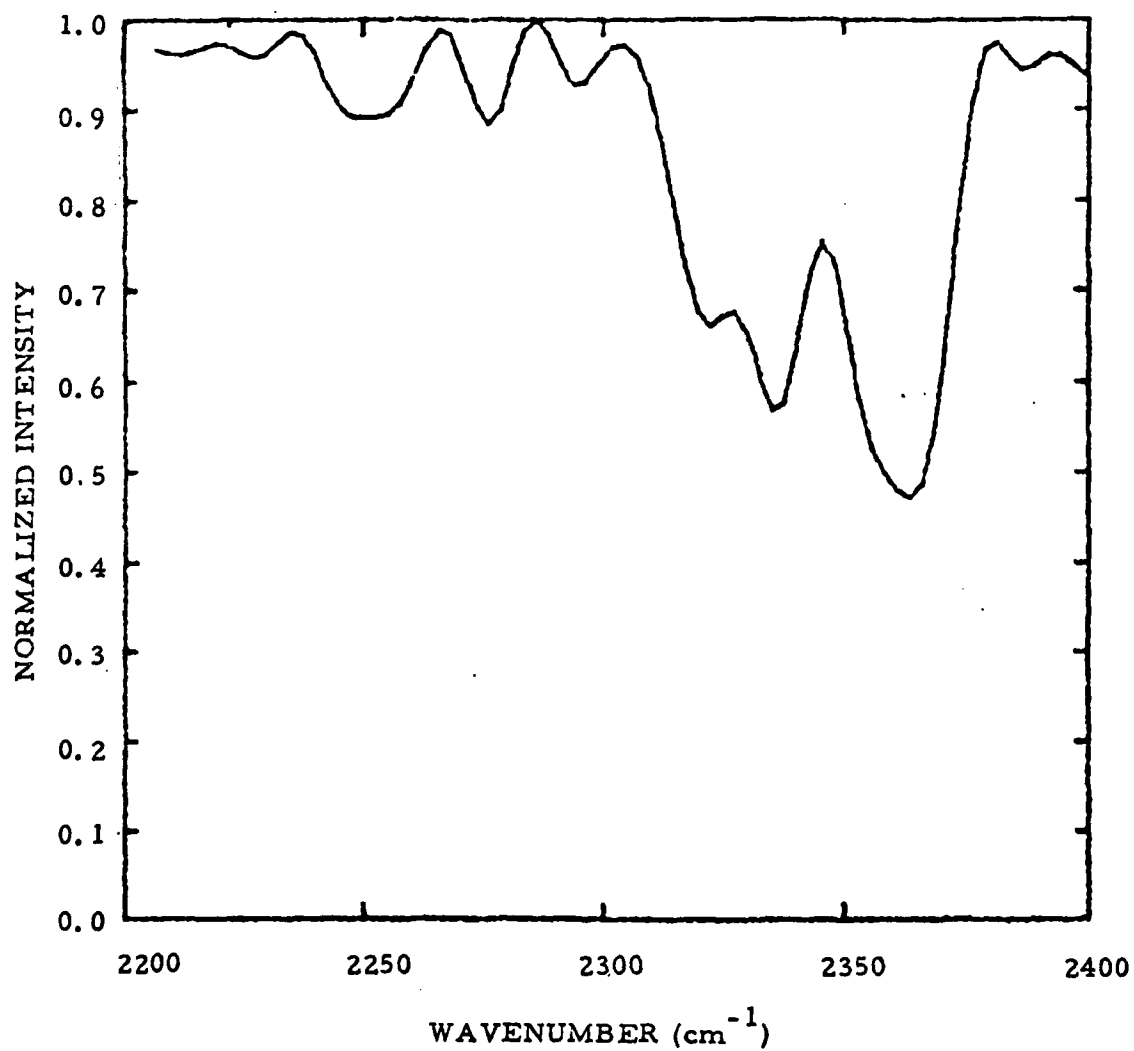


Fig. 27 CO₂ absorption feature in the spectrum of a 1173 K blackbody.
No purging of the optical path was attempted.

Eq. (34) that for this sampling interval the maximum absorption coefficient, k_v , calculated for a given transition will necessarily be within 10% of the line center value, k_{v_0} .) This calculation is rigorous in that absorption far into the wings of the transitions as well as the effect of overlapping lines are taken into account.

The predicted transmission of a blackbody source was determined for a range of atmospheric CO_2 mixing ratios. These Hi-tran type predictions were then convolved with a 10 cm^{-1} resolution sinc slit function. The predicted atmospheric CO_2 absorption features are plotted in Fig. 28 for a range of concentrations. It is seen that the fractional absorption changes rather slowly with CO_2 concentration and that the predicted curves are very similar in shape to the data of Fig. 27, with the absorption increasing and broadening as the amount of CO_2 is increased. Due to spectral noise, an exact spectral match to one of the predictions was not possible. Thus it was felt that comparison of the integrated areas of the absorptions would provide a more exact determination of the atmospheric CO_2 concentration. The observed fractional transmission of the blackbody radiation over the $2310\text{-}2380 \text{ cm}^{-1}$ range is 68% (assuming the detector exhibits a flat response over this spectral range). The predicted fractional transmissions for several atmospheric CO_2 concentrations are listed in Table III and it can be seen that, the amount of atmospheric CO_2 present in the unpurged optical path may be estimated to be ~ 410 ppm in reasonable agreement with the value deduced earlier from an analysis of the unpurged $\text{CO}_2(\nu_3)$ emission signature, see Fig. 26. (It is seen however that the fractional transmission is only a weak function of the atmospheric CO_2 mixing ratio and thus this is not a very sensitive technique for determining the mixing ratio.)

Blackbody calibrations taken with a purged optical path exhibited CO_2 absorption features of the same magnitude as those observed with unpurged

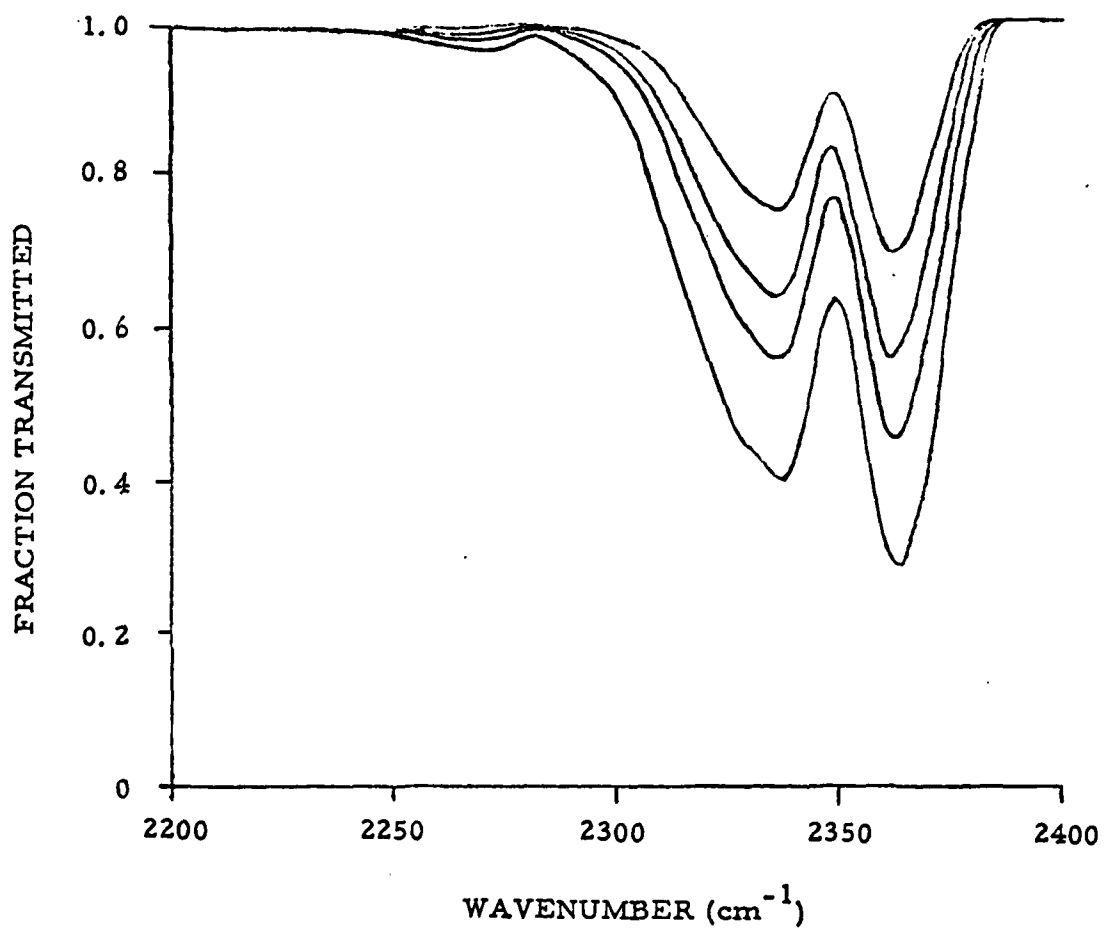


Fig. 28. Hi-tran predictions of blackbody radiation with atmospheric CO₂ absorption features for a range of CO₂ pressures. In order of increasing absorption the concentrations are 165 ppm, 330 ppm, 495 ppm and 990 ppm.

TABLE III
PREDICTED FRACTIONAL TRANSMISSIONS OF
BLACKBODY RADIATION

CO ₂ Concentration	Fractional Transmission
495 ppm	0.64
430 ppm	0.67
390 ppm	0.69
360 ppm	0.70
330 ppm	0.71
306 ppm	0.73
250 ppm	0.75
165 ppm	0.82

runs. This is probably the result of the diffusion of CO_2 from the room air into the optical path during interferometer rotation. Thus, the success of the purge in removing CO_2 can only be estimated from the emission data. Considering the agreement between unpurged concentrations deduced from the emission signatures and from the blackbody absorption data, this latter method of estimating the atmospheric CO_2 is felt to be reasonably accurate.

Finally, spectral modeling of the three high pressure runs (28MAR2, 18APR2, and 18APR3) was undertaken in order to observe the effect of increased collisional broadening on the predicted spectra. The CO_2 fluorescence observed near beam termination for the two 18APRIL runs is displayed in Figs. 29 and 30. Both spectra are similar to those observed at lower pressures. The increasing intensity at low wavenumbers is due to the onset of CO fluorescence ($v = 1$ R branch) which is the dominant spectral radiator under these conditions. Note that in comparison to the low pressure data the shoulder on the 2310 cm^{-1} feature is more pronounced, making the entire feature broader, especially for the 86 torr case (Fig. 30). The optical path was not purged during these runs.

Test chamber transmission functions were tabulated for these cases again using Whiting's⁷ approximation for the Voigt lineshapes with HWHM linewidths, b_v , of 0.0087 cm^{-1} and 0.0128 cm^{-1} , for the 50 and 86 torr cases respectively. These transmission functions are plotted against SN_R in Fig. 31 along with the predicted transmissions for the Doppler and Lorentz limits and the Voigt profile prediction for 9 torr taken from Fig. 6. The additional broadening at higher pressures produces increased intensity in the wings of lines and thus increased relative transmission. As a result, the 626 fundamental transition is the dominant contributor to the intensity. The relative contributions of the 626 fundamental band and the two strongest hot bands and of the 636 fundamental band are plotted in Fig. 32 as a function of the CO_2 pressure for the 85 torr argon case. Note that the fraction of

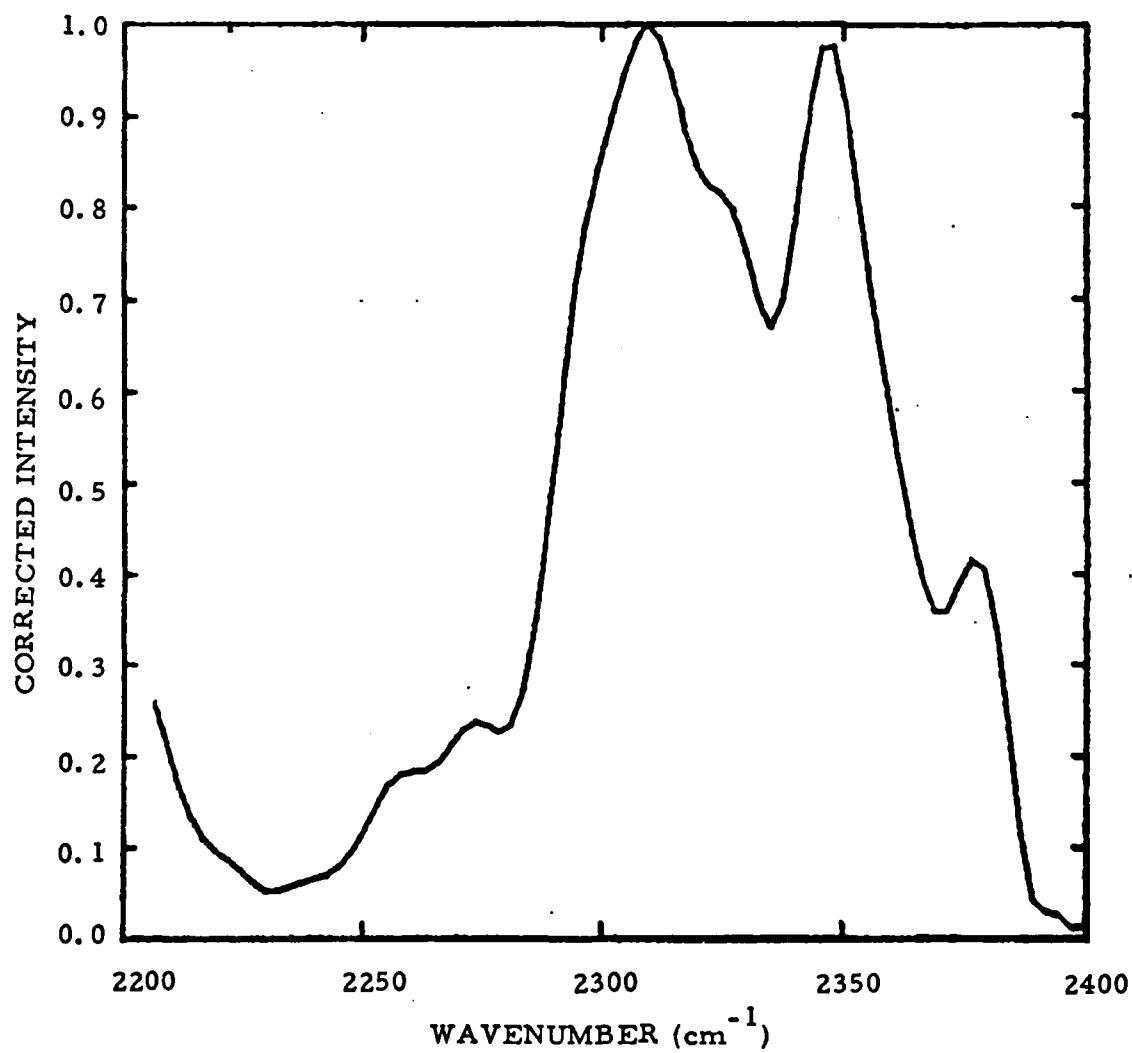


Fig. 29 Observed fluorescence, 0.1 msec before beam termination, from 0.3 torr CO₂, 49.7 torr Ar (18 APRIL RUN 2) with no optical path purge.

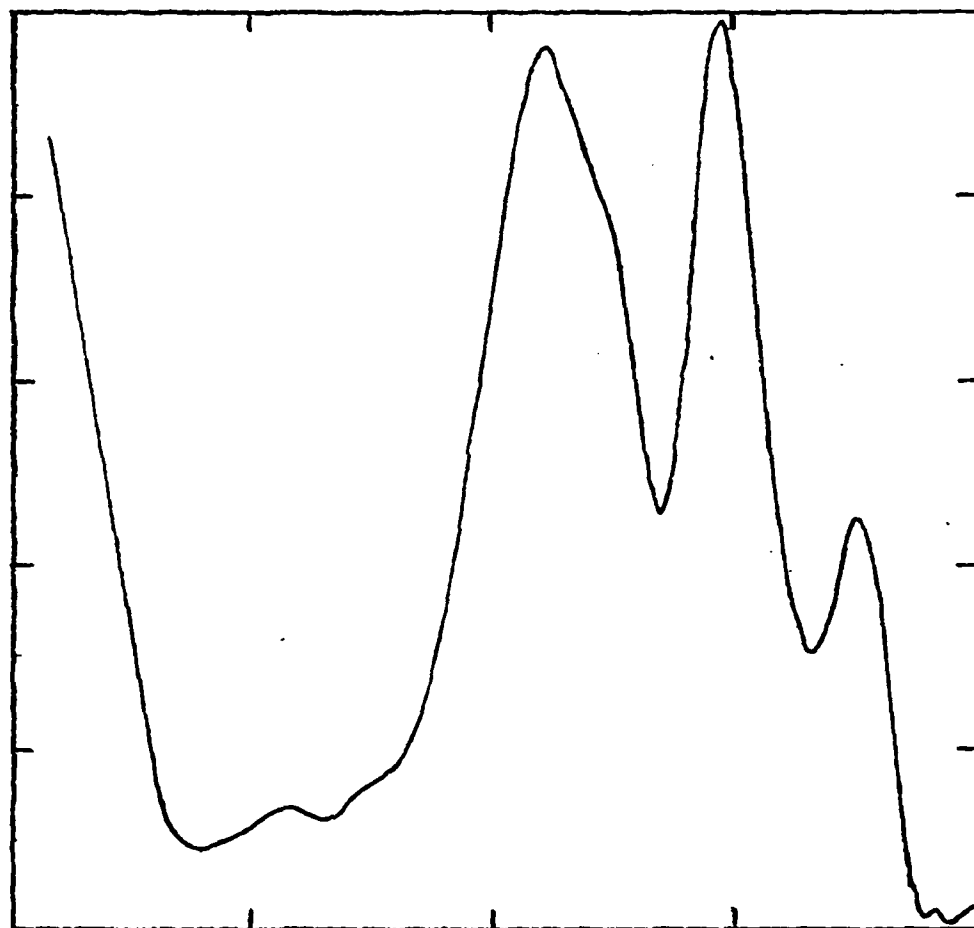


Fig. 30. Experimental data, 0.1 msec before beam termination, from a 0.2 torr CO_2 , 86 torr Ar experimental mixture (18 APRIL RUN 3). There is no purging of the optical path.

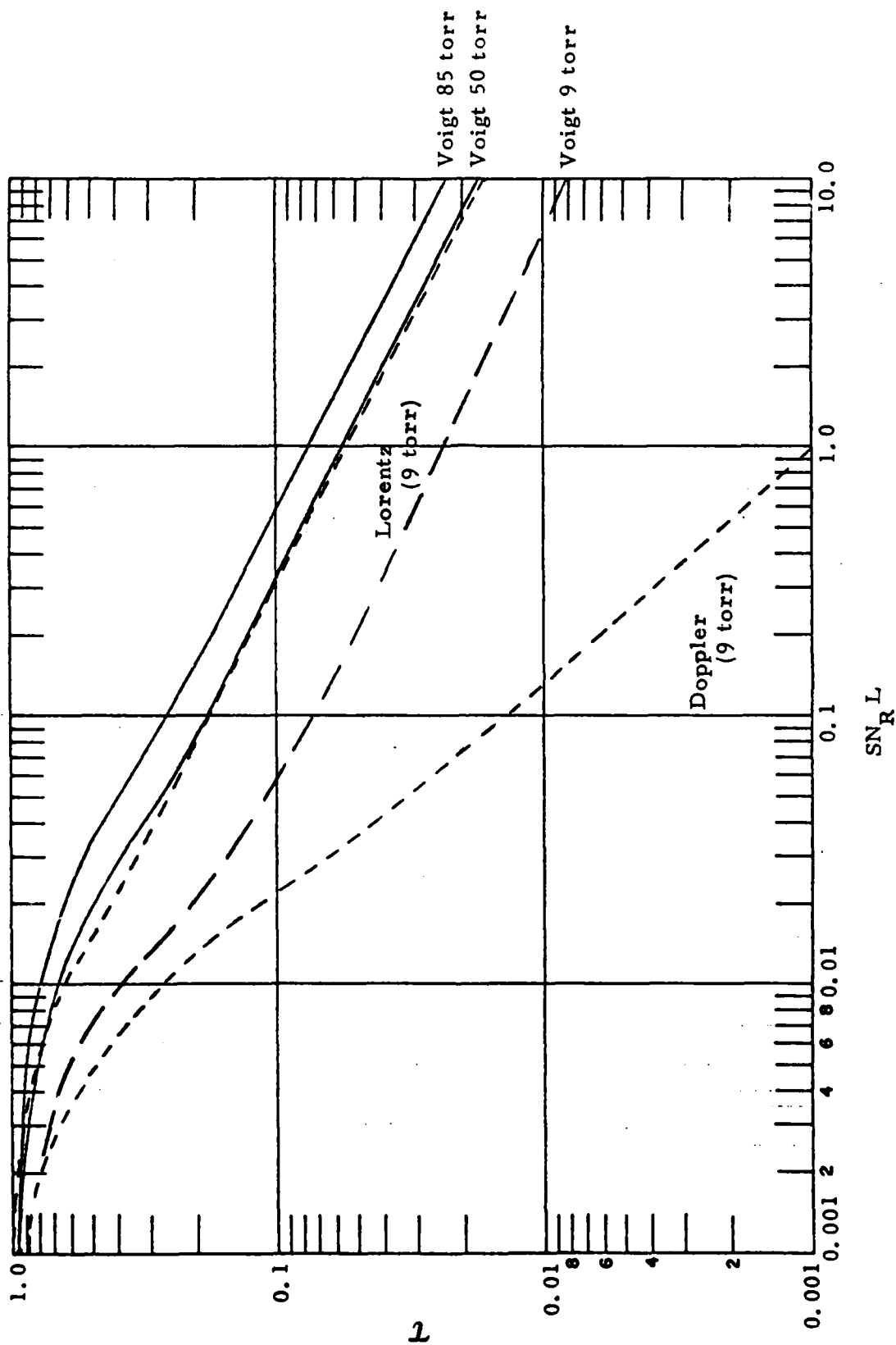


Fig. 31 Fractional transmission as a function of rotational line-strength times column density for two high pressure Voigt calculations. Previous transmission functions are plotted as broken lines for comparison.

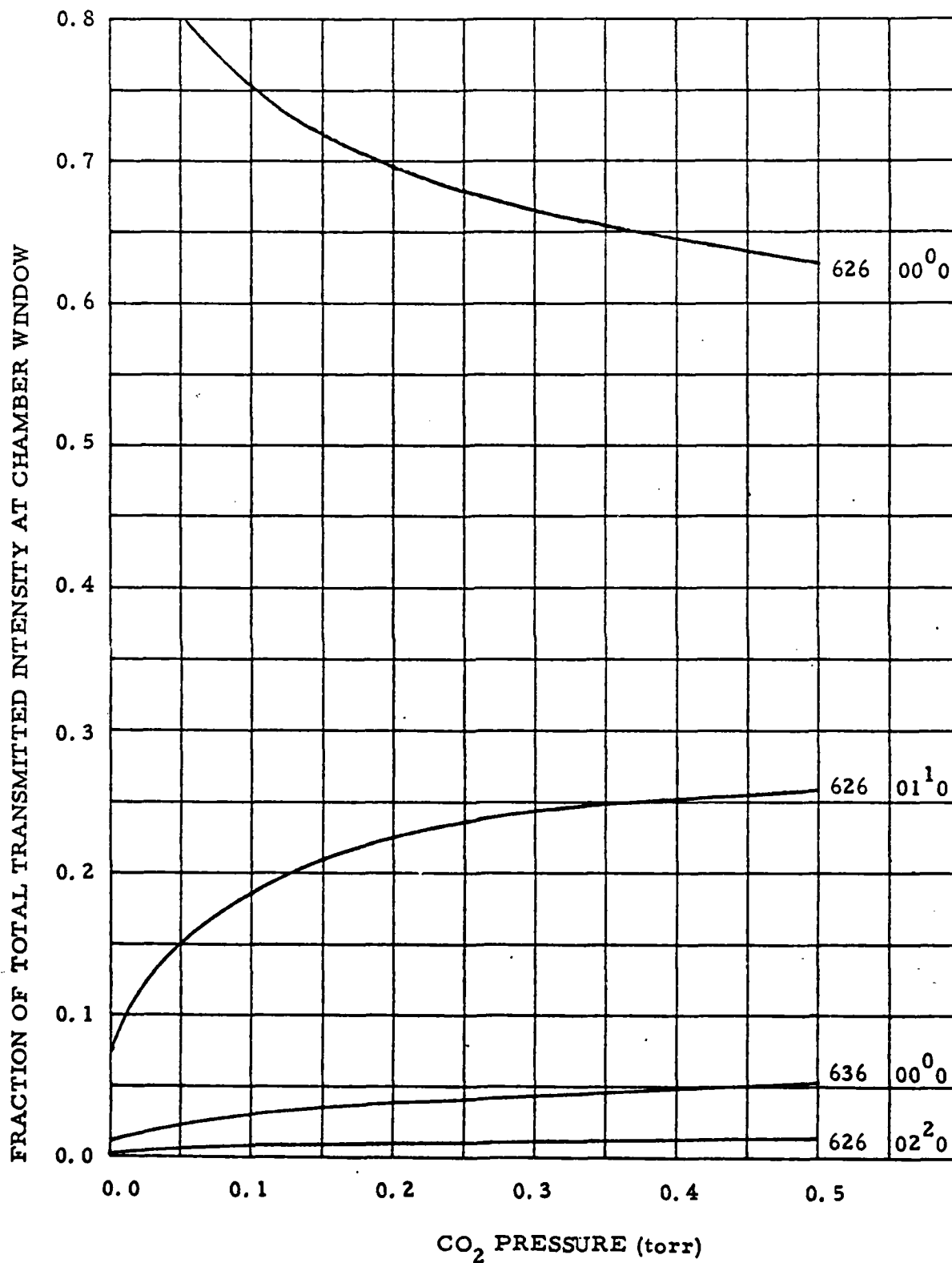


Fig. 32. Relative contributions of four of the strongest bands to the total transmitted intensity at the chamber window as a function of CO₂ pressure in 85 Torr of argon.

transmitted radiation due to transitions other than the 626 fundamental band is much smaller at this increased pressure (compare with Fig. 9). This effect is evident from the predicted chamber window spectra shown in Figs. 33 and 34 for test chamber CO₂ pressures of 0.33 and 0.10 torr; The hot-band and isotopic radiation is apparent only as a shoulder on the low wavenumber side of the fundamental transition P branch.

The total predicted CO₂(v₃) band intensity incident upon the detector, with and without the effects of atmospheric CO₂ absorption are plotted in Fig. 35; The lower curve is calculated using an atmospheric CO₂ concentration of 430 ppm. Similar predictions for 9 torr total pressure are shown for comparison. It can be seen that the transmitted intensities. For the higher pressure case are substantially greater and vary less with chamber CO₂ pressure than the 9 torr predictions.

The predicted spectrum after convolution with a 10 cm⁻¹ resolution sinc slit function is plotted in Fig. 36. This spectrum was generated assuming 0.2 torr chamber CO₂ pressure, 85 torr Ar pressure and an atmospheric CO₂ concentration of 430 ppm. Plotted for comparison is the experimental data of Fig. 30. The predicted spectrum is similar in shape to the low pressure predictions. The predicted shoulder intensity is again less than the observed. However the intensities of the 2350 and 2380 cm⁻¹ peaks are in good agreement with the data. A similar comparison between the 50 torr data and prediction is shown in Fig. 37. This prediction is for 0.33 torr of CO₂ in 50 torr of argon with an atmospheric CO₂ concentration of 430 ppm. Again, all spectral features are matched, but the intensity of the shoulder at 2320 cm⁻¹ is considerably underestimated. Considering that the non-overlapping line approximation becomes less appropriate with increasing pressure the comparison between data and prediction is reasonable.

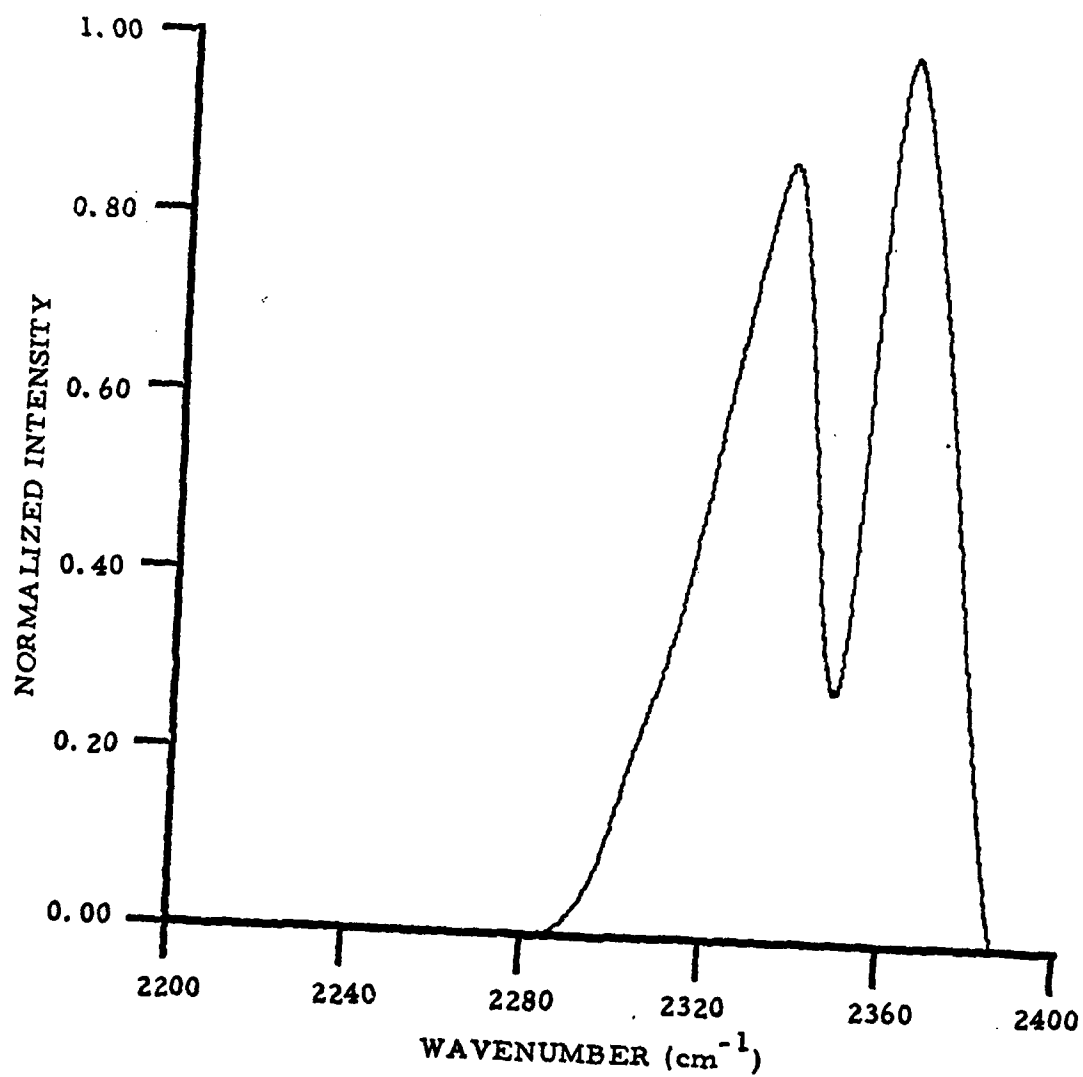


Fig. 33 Predicted fluorescence at chamber window for Voigt lines broadened by 85 torr Ar. Resolution is 10 cm^{-1} . $P_{\text{CO}_2} = 0.33 \text{ torr}$. Maximum intensity = $5.265 \times 10^{-26} \text{ W/molecule-str-cm}^{-1}$.

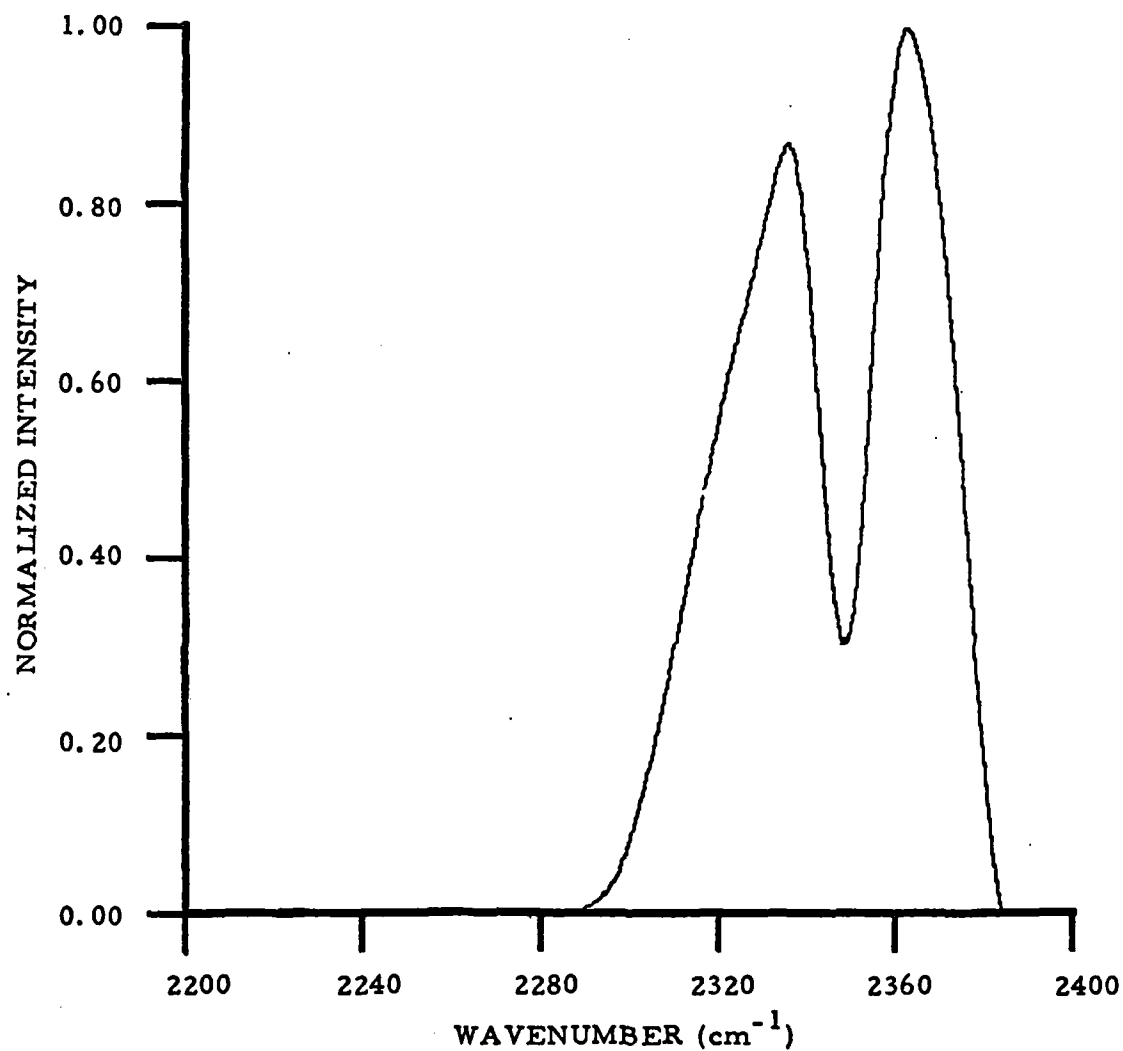


Fig. 34 Predicted fluorescence at chamber window for Voigt lines broadened by 85 torr Ar. Resolution is 10 cm^{-1} . $P_{\text{CO}_2} = 0.10 \text{ torr}$. Maximum intensity = $1.00 \times 10^{-25} \text{ W/molecule-str-cm}^{-1}$.

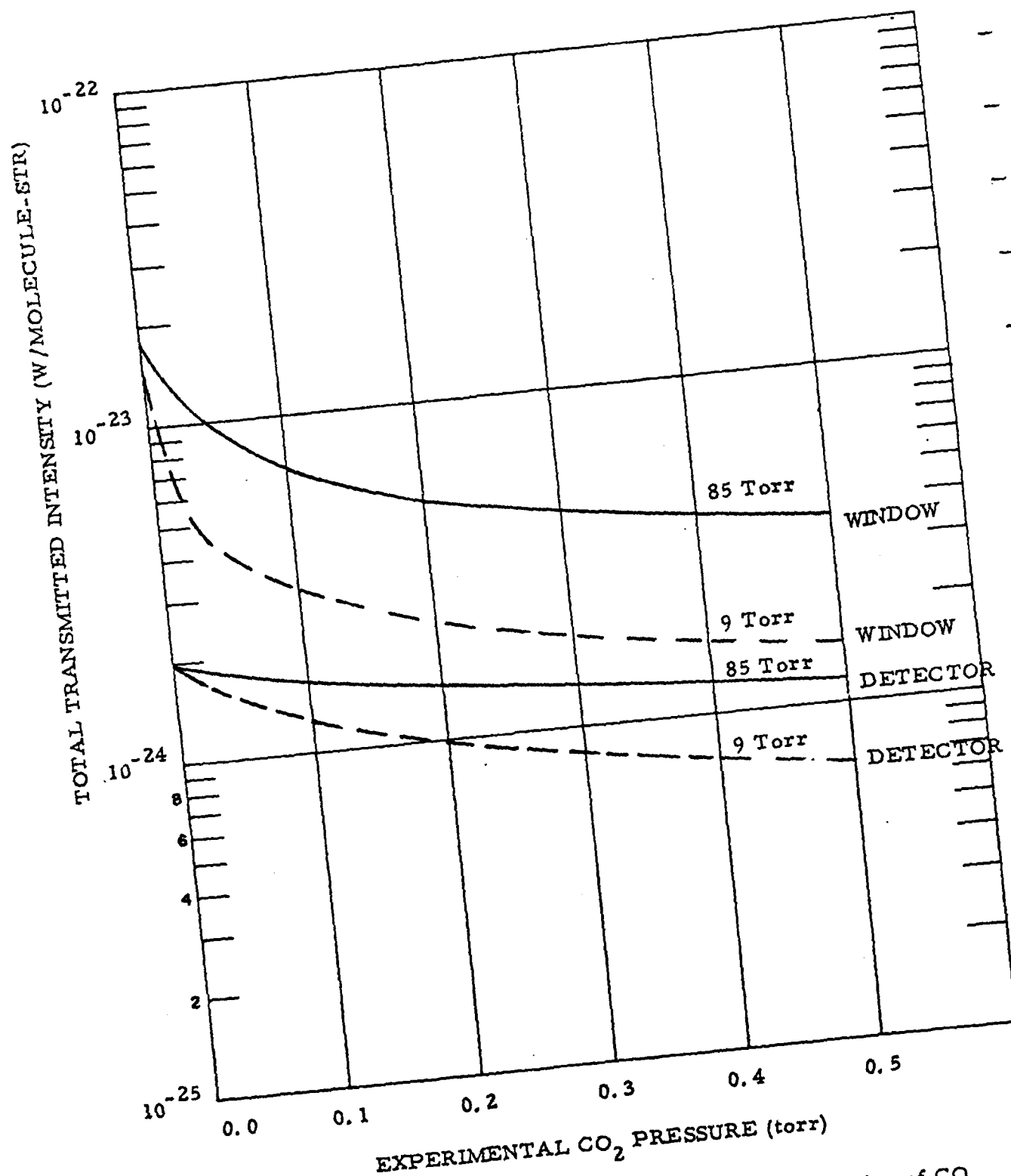


Fig. 35. Total transmitted intensity for all bands as a function of CO₂ pressure for Voigt lines broadened by 85 Torr of Argon. Lower curves include effects of 660 ppm atmospheric CO₂ attenuation. Voigt calculations for 9 torr case are shown as broken lines for comparison.

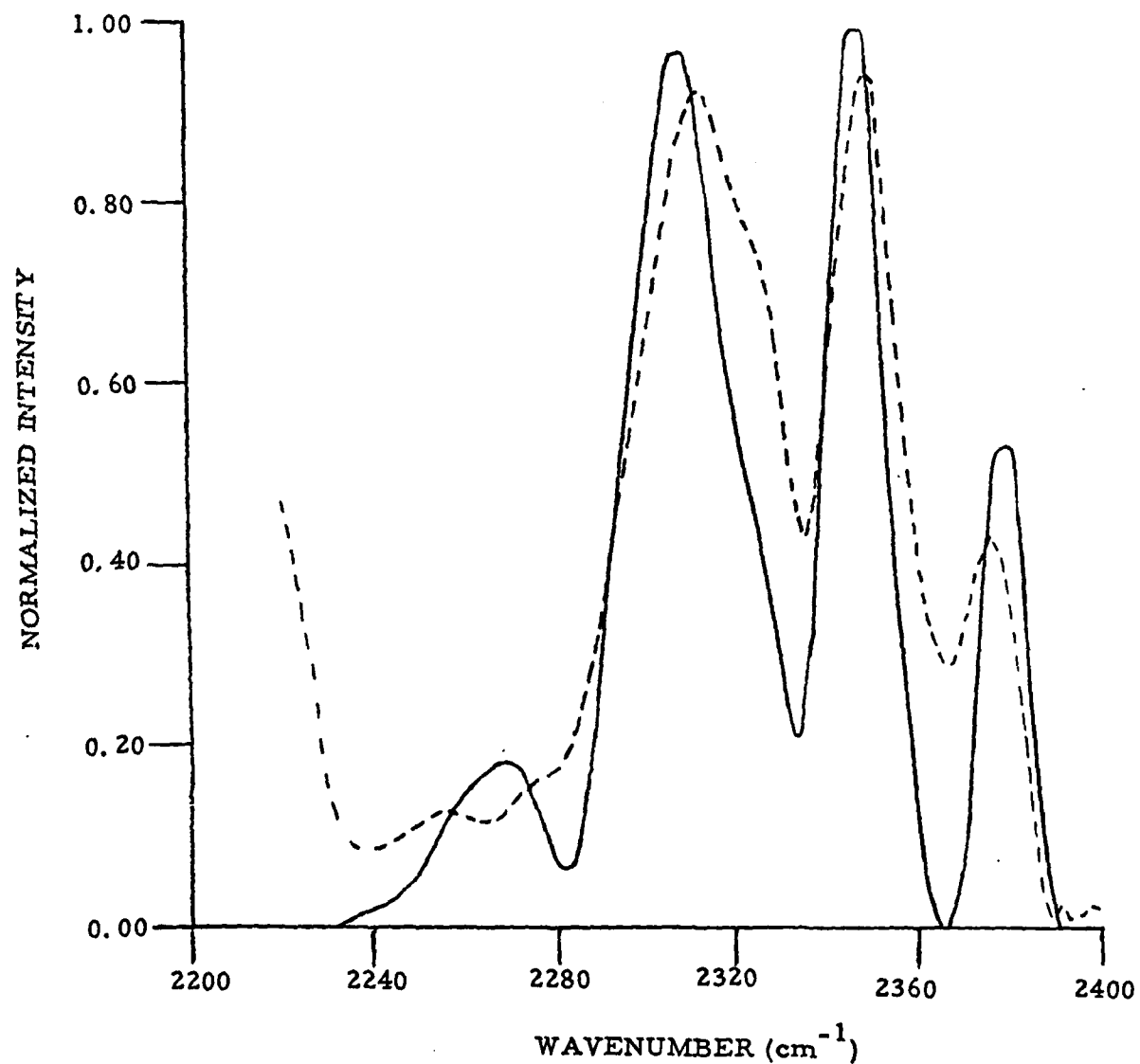


Fig. 36. Comparison of predicted spectrum using 0.2 torr CO₂, 85 torr argon and 430 ppm atmospheric CO₂ with experimental data (broken line) of Fig. 25. Resolution is 10 cm⁻¹.

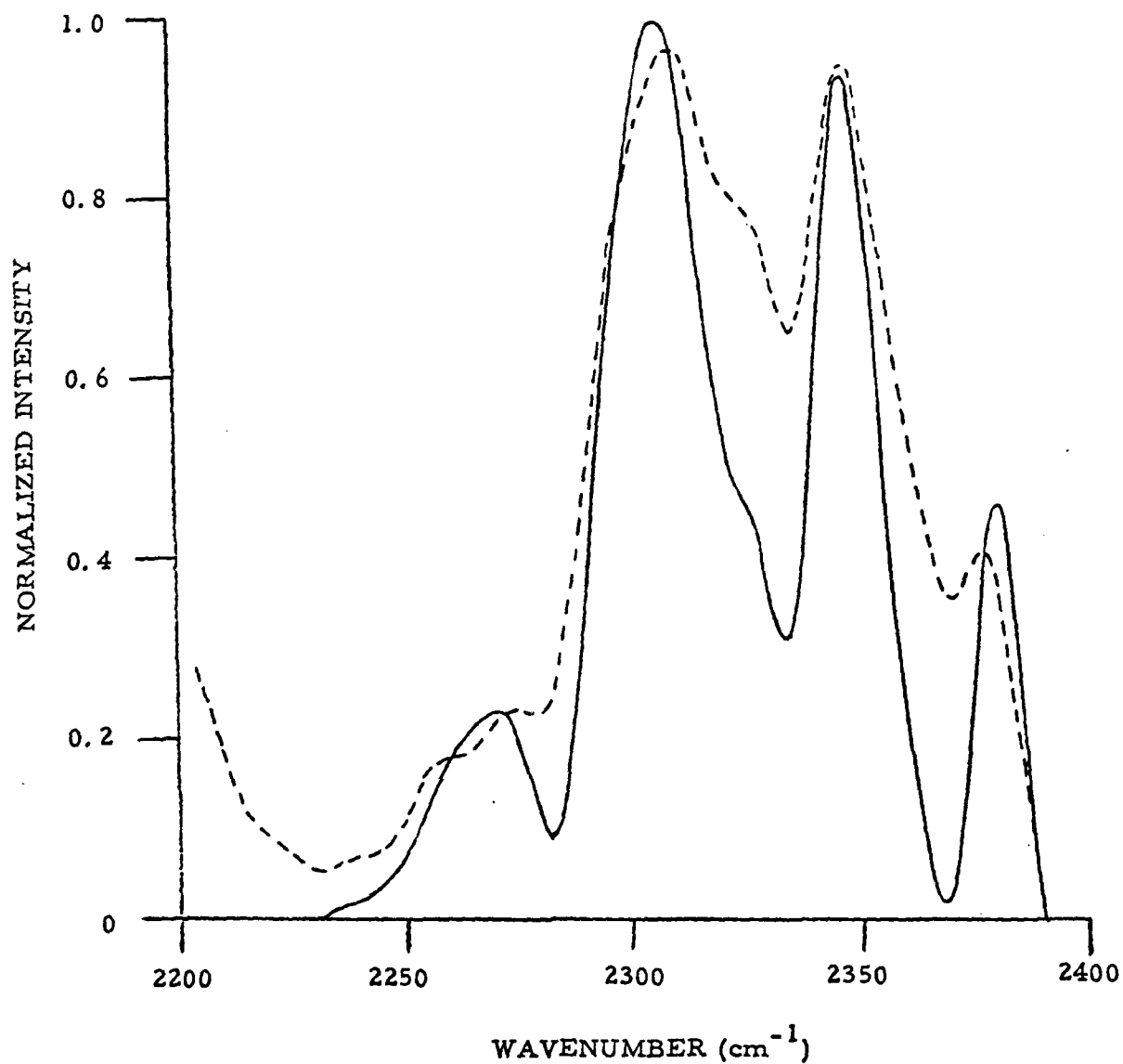


Fig. 37. Comparison of predicted spectrum using 0.33 torr CO₂, 50 torr Ar and 430 ppm atmospheric CO₂ with experimental data (broken line) of Fig. 24. Resolution is 10 cm⁻¹.

In conclusion, spectral modeling has been successful in matching the experimental CO_2 fluorescence data over a range of experimental CO_2 partial pressures, experiment total pressures, and atmospheric CO_2 concentrations through consideration of attenuation of the emission by Voigt-broadened resonant absorbers in the chamber and by Lorentz broadened absorbers in the detection system optical path. The net result of this analysis is the quantity f , the fractional transmission of the $\text{CO}_2(\nu_3)$ band fluorescence over the optical path. This quantity is shown plotted in Fig. 38 as a function of CO_2 test chamber pressure for $P_{\text{Ar}} = 9$ torr and several atmospheric CO_2 mixing ratios and may be used in conjunction with Eq. (15) to determine the total $\text{CO}_2(\nu_3)$ concentration within the field-of-view.

E. Determination of the Excitation Efficiency

Total $\text{CO}_2(\nu_3)$ concentrations observed within the field of view may now be deduced from the band intensity data through use of Eq. (15). This has been done for six cases all corresponding to an argon pressure of 9 torr and beam voltage of 30 kV and the results are displayed in Table IV. Note that many of the quantities tabulated are double valued because of uncertainties in the CO_2 partial pressure. In each case the first value tabulated is for the nominal measured CO_2 pressure which, in the existing experimental configuration, is difficult to measure accurately when CO_2 represents only a small fraction of the total gas pressure. The second value listed is for the CO_2 pressure deduced from the CO vibrational kinetic analysis presented in the next section. Fortunately, as can be seen from Fig. 38, the quantity f varies only weakly with CO_2 pressure and thus this uncertainty will not significantly effect the deduced $\text{CO}_2(\nu_3)$ concentration.

The band intensities listed in Table IV as well as the deduced values of N_{ν_3} are specific to an irradiation time of 2.4 msec, just prior to beam termination. The global excitation rate, R_{ν_3} , may be deduced from the

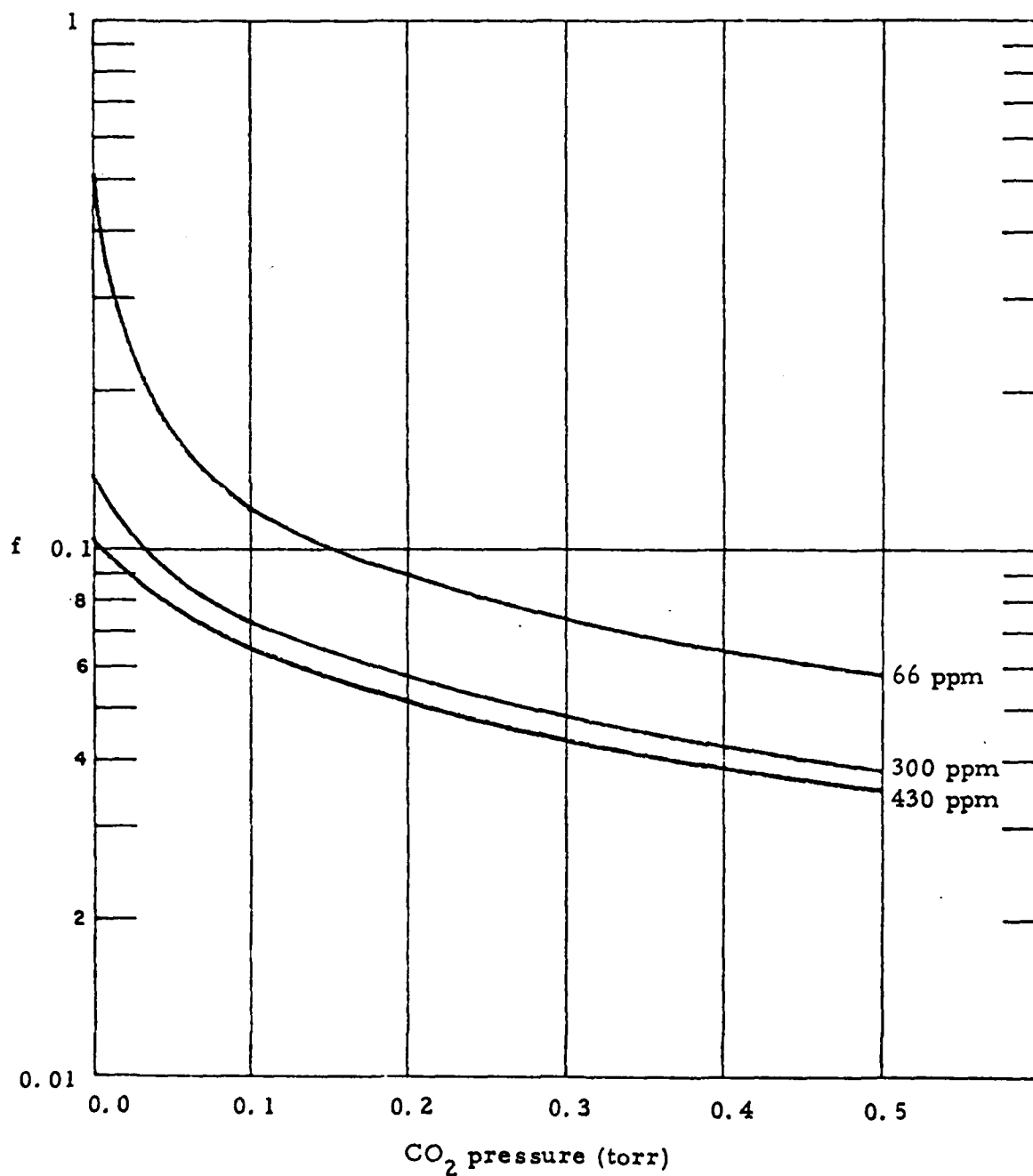


Fig. 38. The specific transmittivity as a function of experimental CO₂ pressure for different amounts of atmospheric CO₂: 66 ppm (fast purge), 300 ppm (slow purge) and 430 ppm (no purge).

TABLE IV

CO₂(v₃) CONCENTRATIONS AND EXCITATION RATES WITHIN THE FIELD OF VIEWP_{Ar} = 9 torr ; V = 30 kV

Case ID	P _{CO₂} torr	Ambient CO ₂ ppm	I(v ₃) × 10 ⁴ W/sr	f [*]	N _{v₃} [*] × 10 ⁻¹⁵ t = 2.4 msec	R _{v₃} [*] × 10 ⁻¹⁸ sec ⁻¹
9Mar1	0.1-0.21	66	3.60	0.12-0.087	1.89-2.59	1.48-2.02
11Mar1	0.2-0.23	300	2.59	0.058-0.054	2.82-2.96	2.19-2.30
11Mar2	0.1-0.12	300	3.37	0.073-0.069	2.87-3.06	2.23-2.38
16Mar2	0.1-0.15	300	3.36	0.073-0.064	2.86-3.27	2.22-2.53
16Mar3	0.1-0.15	300	3.07	0.073-0.064	2.62-2.99	2.03-2.32
16Mar4	0.1-0.14	300	3.00	0.073-0.066	2.56-2.85	1.99-2.22

* First value is for nominal case CO₂ pressure, second value is that deduced from CO kinetic analysis presented in Section IV.

$\text{CO}_2(\nu_3)$ concentrations by evaluating Eq. (12) at the appropriate irradiation time and using the observed decay time of $\tau_{\nu_3} = 1.7 \times 10^{-3}$ msec. The results of this evaluation are also tabulated in Table IV and are found to vary between $1.5 - 2.5 \times 10^{18}$ excitations/sec.

It is of fundamental interest to compare this rate of $\text{CO}_2(\nu_3)$ mode excitation to the total rate of electron beam energy deposition within the field of view. For a thin target this latter quantity may be defined as

$$P_{\text{FOV}} = I \rho \left(\frac{1}{\rho} \frac{dE}{dx} \right) L_f g' \quad (37)$$

where ρ is gas density, 2×10^{-5} gm/cm³, L_f is the diameter of the field of view, 6.4 cm, and g' is the fraction of beam energy deposited over the distance L_f which falls within the circular field of view. The quantity g' has been evaluated to be 0.773 for the appropriate beam shape, see Section II. The beam stopping power, $1/\rho \, dE/dx$, has been tabulated by Berger and Seltzer¹² as 6.5 MeV - cm²/gm for 30 keV electrons in Ar. However, it has long been recognized that the results of Berger and Seltzer should be considered as lower bounds because they do not include the effects of multiple scattering. A more accurate representation is given by the Monte Carlo electron energy deposition calculation performed using the ELTRAN computer code. The beam stopping power at the center of the field of view predicted from use of this code was 14.5 MeV - cm²/gm. The beam stopping power does vary across the field of view and in integrated value would present a more accurate representation. This variation will be included in future analyses.

The rate of beam energy deposition within the field of view for the six cases of Table IV are tabulated in Table V. These listed values are

TABLE V

ELECTRON EXCITATION EFFICIENCY FOR $\text{CO}_2(\nu_3)$ MODE $P_{\text{Ar}} = 9$ torr ; $v = 30$ kV

Case ID	I mA	P_{FOV}^* watts	P_{ν_3} watts	Excitation Efficiency (%)
9Mar1	0.59	.85	.068-.092	8.0-10.8
11Mar1	0.67	.96	.101-.107	10.5-11.1
11Mar2	0.81	1.16	.104-.110	9.0-9.5
16Mar2	0.84	1.21	.102-.117	8.4-9.7
16Mar3	0.78	1.12	.094-.107	8.4-9.6
16Mar4	0.79	1.13	.092-.102	8.1-9.0
			Average	8.7-10.0

* Calculated using the beam stopping power of Ref. 13.

** First value is for nominal CO_2 pressure, second value is that deduced from CO kinetic analysis presented in Section IV.

specific for the Monte Carlo code value of the beam stopping power at the center of the field-of-view. Also listed in Table V are the beam currents for each case. The total rate, within the field-of-view, of feeding electron energy to the $\text{CO}_2(\nu_3)$ mode is defined as

$$P_{\nu_3} = R_{\nu_3} (h\nu) \quad (38)$$

where $h\nu$ is the energy of a ν_3 quanta. The total electron excitation efficiency for the $\text{CO}_2(\nu_3)$ mode is then just the ratio P_{ν_3}/P_{FOV}

The resulting values of P_{ν_3} and the electron excitation efficiency are also shown in Table V for the excitation rates listed in Table IV. The deduced efficiencies do not vary significantly from case to case and average between 8.7-10% depending on the choice of CO_2 pressures. Note that the fast purge case (9Mar1), which has a band transmission correction f about a factor of two larger than those of the other cases, exhibits an efficiency in good agreement with the other data. Furthermore there does not seem to be any significant difference in electron excitation efficiency over the factor of two variation in CO_2 pressure. A large error bar of $\pm 4\%$ must be associated with these efficiencies due to uncertainties in the beam energy deposited and instrument misalignment errors. The effects of interferometer misalignment on absolute intensity require further definition.

There does not appear to be any other measurements to which these CO_2 excitation efficiencies can be compared. There is however a computer model available which was developed for determining the relative allocation of electron energy deposited in gas mixtures. This code uses a set of parameterized cross sections for each gas to determine the apportionment of absorbed electron energy among the various possible paths of atomic and

molecular excitations and ionizations. The calculations are performed using the continuous slowing down approximation and include the effect of the total decay (to thermalization) in primary electron energy as well as the effect of all additional excitations/ionizations caused by secondary and higher order electrons. This computer model is well documented¹⁴ and has been previously used to provide electron energy allocation predictions in pure Ar¹⁵ and pure CO₂¹⁶ among other gases. Furthermore the parameterized cross sections required as input to the model are now available¹⁷ for nine gases: Ar, H₂, H₂O, O₂, N₂, O, CO, CO₂ and He.

Energy allocation predictions have been made with this code for various mixtures of CO₂/Ar; typical results are shown in Figs. 39 - 40 for the case of 1% CO₂ in Ar. The predicted excitation efficiencies for various inelastic processes in Ar are shown in Fig. 39 as a function of primary electron energy. Similar results for CO₂ are presented in Fig. 40. (Notation is as in Refs. 15 and 16.) These excitation efficiencies, which are the fraction of primary electron energy partitioned into all relevant ionization, electronic state and vibrational excitation processes, are seen to asymptote for primary electron energies greater than one keV and thus the efficiencies for 30 keV primaries will be the same as those shown for 10 keV primaries.

The predicted excitation efficiency for the CO₂(v₃) mode is found to be 17.1% which is nearly twice as large as the measured values of ~9% listed in Table V. Furthermore the predicted efficiency is found to vary only slightly with CO₂ mole fraction, being 16.8% for a 10% CO₂/90% Ar and 14.1% in pure CO₂. As will be discussed in Section IV, the CO fluorescence that is observed may be due to the dissociative recombination reaction



The beam created species CO and O remain in the field of view for several pulses, and should be included in the gas mixture composition for energy allocation predictions. Inclusion of these species decreases the predicted CO₂

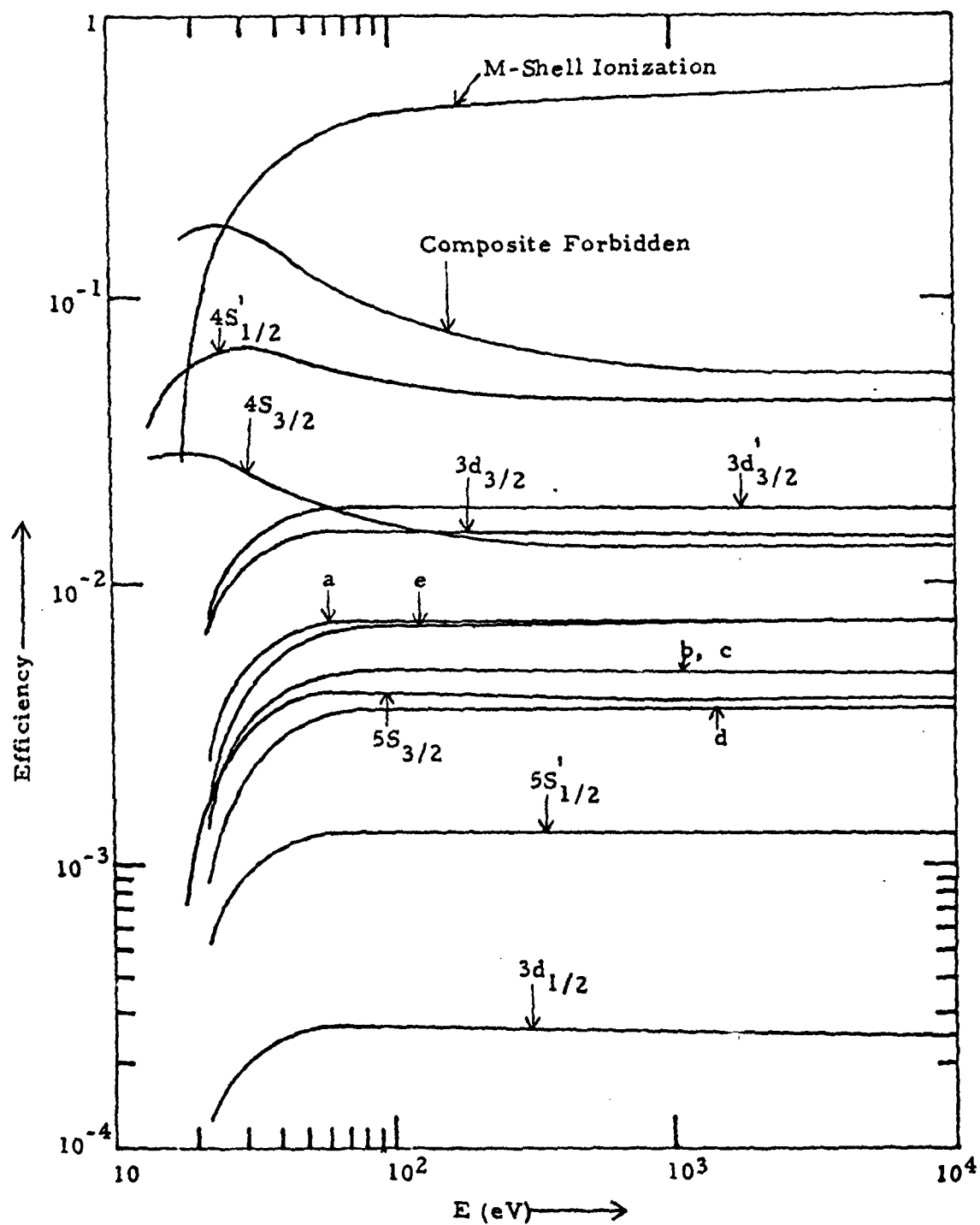


Fig. 39. Argon excitation efficiencies as a function of primary electron energy for a 1% CO₂/99% Ar mixture.

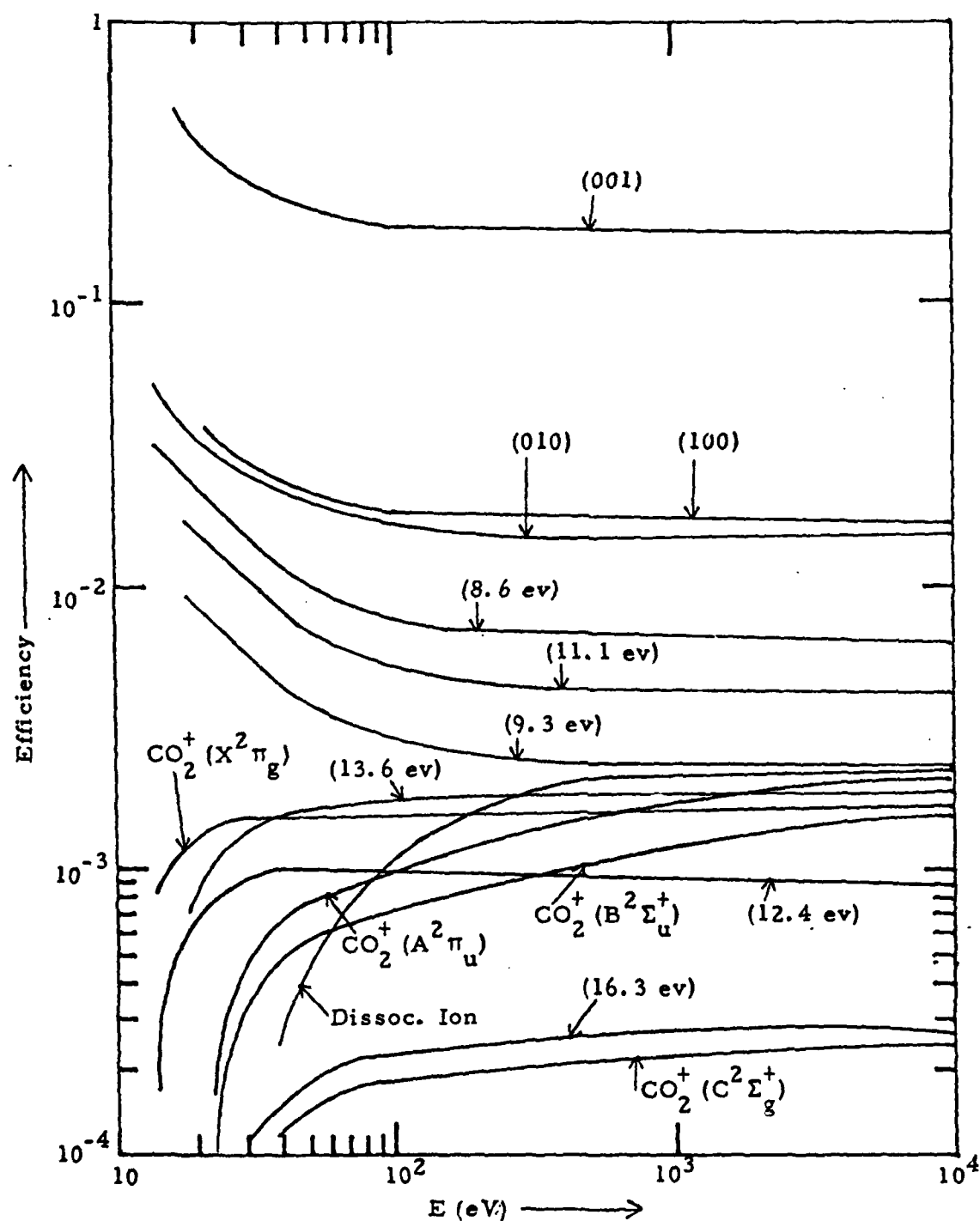


Fig. 40. CO_2 excitation efficiencies as a function of primary electron energy for a 1% CO_2 /99% Ar mixture.

(ν_3) excitation efficiencies. For example, at concentrations of 0.03 torr beam created CO and O would have the effect of reducing the predicted ν_3 efficiency to the observed $\sim 9\%$ value. At present there is no way to quantitatively estimate the concentration of beam created species. Additionally, the CO excitation cross-sections used in the computer predictions are incomplete. Thus the theoretical predictions and experimental observations may be reconciled, but accurate verification will require future analysis.

The CO_2 pressure has only been varied slightly in the present study, however in previous² work the ν_3 fluorescent intensity was measured over a factor of ten range in CO_2 concentration. As an example it was observed in the earlier work (see Fig. 60 of Ref. 2) that the relative $\text{CO}_2(\nu_3)$ band intensity per unit beam current decreased by a factor of 0.55 as the CO_2 pressure was increased from 0.1 to 0.5 torr. From Fig. 38 it may be seen that the predicted band transmission function f also decreases approximately by a factor of 0.55 over that pressure range. Thus the data, in agreement with prediction, are consistent with a relatively constant $\text{CO}_2(\nu_3)$ excitation efficiency over at least a factor of five range in CO_2 pressure. Additional runs over a wide CO_2 pressure range should be performed to substantiate this observation.

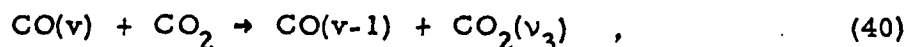
IV. CO DATA ANALYSIS

The dominant infrared fluorescent feature observed in electron irradiated mixtures of CO_2/Ar is the fundamental vibration/rotation band of CO. Fluorescence from at least the first fourteen vibrational levels of CO is observed and the vibrational distributions are highly non-Boltzmann in nature. The kinetic interpretation of this data has been considered in great detail in Ref. 2 and will only be discussed briefly here.

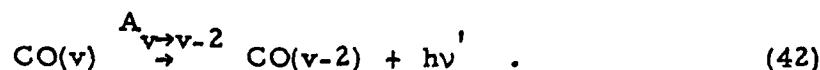
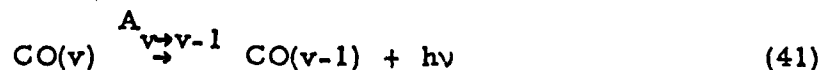
CO is not present in the test gas and thus must be formed chemically through reactions involving electron beam created species. One such possible source would be to the dissociative recombination reaction



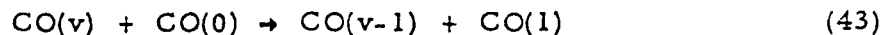
Once the vibrationally excited CO is formed it is subject to various deactivation reactions, dominantly vibrational exchange with CO_2



and radiative decay



It is also possible for the vibrationally excited CO to react with electron beam created species which can build up in concentration within the test chamber. The most important of these would be



where the vibrationally cold CO is the cumulative result of all beam pulses occurring during the test gas residence time within the field of view. The possible effects of reaction (43) have been examined in some detail² and efforts have been made to take data under conditions where this process will be unimportant.

A preliminary analysis and interpretation of a relatively large CO fluorescence data base will be presented in the following pages. The ultimate goals of this analysis are: (a), the determination of the vibrational level dependent rate constants for reaction (40), (b), the deduction of the rates for CO(v) production within the field of view, and (c), the specification of the electron beam efficiency for producing vibrationally excited CO.

The techniques used in the data reduction and interpretation have been discussed previously² and will only be briefly reviewed here. These techniques have been used to analyze the large data base accumulated during the present reporting period. Only preliminary analysis has been performed on the complete data base. More detailed work is currently in progress, and methods of increasing the reliability of the deduced populations of high lying vibrational levels are being investigated. The eight experimental runs which have a suitable combination of CO₂ pressure, flow rate, and signal level to permit modeling of CO kinetics are presented in Table VI along with the relevant experimental conditions. As can be seen several of the runs differ only in the gas residence time in the field of view. No variation in the kinetic relaxation rate was observed between these runs, suggesting that cold CO does not play a significant role in the relaxation of the vibrationally excited CO.

Because the vibrational distributions are non-Boltzmann, determination of the populations must be made by comparison of the intensity data

TABLE VI

EXPERIMENTAL CONDITIONS FOR RUNS INCLUDED IN CO ANALYSIS

Date	Pressure (torr)		Voltage kV	Current mA	Residence Time f. o. v. (sec)	Time Interval (msec)	Deduced CO ₂ pressure
	CO ₂	Ar					
9MARCH 1	0.1	9.0	30	0.59	0.13	0.2-8.2	0.21
11MARCH 1	0.2	9.1	30	0.67	0.17	0.2-8.2	0.23
11MARCH 2	0.1	9.1	30	0.81	0.26	1.0-12.6	0.12
16MARCH 2	0.1	9.0	30	0.84	0.13	1.0-8.2	0.15
16MARCH 3	0.1	9.0	30	0.78	0.17	1.0-8.2	0.15
16MARCH 4	0.1	9.0	30	0.79	0.21	1.0-8.2	0.14
16MARCH 5	0.2	11.0	40	1.26	0.16	1.0-8.2	0.22
16MARCH 6	0.1	11.0	40	1.26	0.16	1.0-8.2	0.14

with a synthesized spectrum which is the sum of unit concentration radiation predictions (basis functions) for each vibrational transition, $v \rightarrow v-1$. This comparison is made using previously developed² non-linear regression analysis techniques. The synthesized spectrum at any wavenumber, $I_p(v)$, is the weighted sum of these fundamental transition basis functions, $\xi_v(v)$

$$I_p(v) = \sum_v n_v \xi_v(v) \quad (44)$$

where the quantity n_v is the total CO population in level v in the detector field of view, and v is the spectral wavenumber. To properly match the spectral data, the basis functions must be convolved over a slit function representative of the optical detection system. Minimization of the squares of the difference between the data, $I(v)$, and the synthetic spectrum, i.e., $(I_p(v) - I(v))^2$, permits determination of the quantities n_v once the basis functions are specified.

The basis functions are comprised of the individual vibrational/rotational transitions of the ground state CO molecule. The intensities of these lines are given by the relationship

$$I_{J \rightarrow J \pm 1}^{v \rightarrow v-1} = \frac{hc v_{v \rightarrow v-1}^4 S_{J \rightarrow J \pm 1} A_{v \rightarrow v-1}}{(2J+1) v_{v \rightarrow v-1}^3} N_{v,J} \quad (45)$$

where v is fixed for each basis function and J ranges over all thermally populated levels. In Eq. (45) h is Planck's constant, c the speed of light, $S_{J \rightarrow J \pm 1}$ is the Honl-London factor,¹² $A_{v \rightarrow v-1}$ is the Einstein coefficient, J is the rotation quantum number, $v_{v \rightarrow v-1}$ is the line center wavenumber of the transition, $v_{v \rightarrow v-1}$ is the wavenumber of the band origin and $N_{v,J}$ is the population of the radiating state. The quantity $N_{v,J}$ may be rewritten as¹⁸

$$N_{v,J} = N_v \frac{hc B_v}{kT} (2J+1) \exp(-F(v,J) hc/kT) \quad , \quad (46)$$

where B_v is the rotational constant for vibrational level v , defined as

$$B_v = B_e - \alpha_e (v + 1/2) \quad (47)$$

and

$$F(v,J) = J(J+1) B_v - D_e J^2 (J+1)^2 \quad . \quad (48)$$

The line and band origin wavenumbers were calculated using the anharmonic oscillator-vibrating rotor approximation, using the latest spectroscopic constants of CO available:¹⁹ $\omega_e = 2169.812$, $\omega_e x_e = 13.289$, $\omega_e y_e = 1.059 \times 10^{-2}$, $B_e = 1.93127$, $\alpha_e = 1.7459 \times 10^{-2}$, and $D_e = 5.6268 \times 10^{-6}$, all in cm^{-1} . The Einstein coefficients represent the least accurately known quantity in Eq. (45). The values of Docken²⁰ have been used in the present analysis. The intensity of a given transition per vibrationally excited molecule, i. e., $I_{J \rightarrow J \pm 1}^{v \rightarrow v-1} / N_v$ may then be found from Eqs. (45) - (48). Summation of these intensities over the system slit function $g(v, v')$ permits construction of the basis functions:

$$\xi_v(v) = \frac{1}{n_v} \sum_J g(v, v_{v \rightarrow v-1}, J \rightarrow J \pm 1) I_{J \rightarrow J \pm 1}^{v \rightarrow v-1}(v_{v \rightarrow v-1}, J \rightarrow J \pm 1) \quad , \quad (49)$$

where the slit function is as defined in Eq. (36) of Section III. Because beam heating of the gas is negligible,² 300 K was chosen as the temperature in generating the basis functions.

AD-A112 253

PHYSICAL SCIENCES INC WOBURN MA

LABCEDE AND COCHISE ANALYSIS II.

FEB 80 B D GREEN, G E CALEDONIA

PSI-TR-207B

VOLUME II.(U)

F/G 7/4

F1962R-77-C-0089

NL

UNCLASSIFIED

AFSL-TR-80-0063(II)

2 4 2

2242

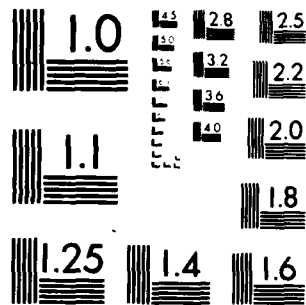
END

DATE

FORMED

4 82

DTIC



MICROCOPY RESOLUTION TEST CHART
NATIONAL BUREAU OF STANDARDS-1963-A

Typical experimental spectra from 16MARCH2 (see Table VI) are plotted in Fig. 41. The spectra are plotted at 0.2 msec intervals, and cover the temporal range of 2.8 - 7.5 msec, i. e., beginning 0.3 msec after beam termination. Note that the spectral position of peak fluorescent intensity shifts from 2040 to 1970 cm^{-1} over this time span; furthermore, the total intensity has dropped an order of magnitude. The fluorescence spectra occurring during the beam pulse are displayed in Fig. 42. In this figure time is increasing toward the rear of the plot. During this displayed time period, 1.0 - 2.4 msec, the spectral shape changes, with the 2000 - 2100 cm^{-1} region increasing in intensity more rapidly than the rest of the spectrum. The rise in intensity above 2220 cm^{-1} is due to the onset of $\text{CO}_2(\nu_3)$ radiation (see Section III). The response of the PbSe detector used in these experiments decreased rapidly below 1900 cm^{-1} . As a result the response corrected fluorescence signal becomes increasingly noisy below 1830 cm^{-1} .

The noise level in the signal between 1830 and 2200 cm^{-1} is sufficiently small to permit accurate fitting to the data over that frequency range for all times displayed in the figures. The signal to noise level in this data is significantly improved over that analyzed previously. An improvement in the differential pumping rate resulted in a reduction of the degree of beam spread prior to entrance into the chamber thus increasing the electron beam current (and the energy deposited in the field of view). Additionally, a solid state pulsing network was used to improve beam pulse current reproducibility. As a result, the noise level does not dominate the signal until below 1780 cm^{-1} , and evaluation of the populations of CO vibrational levels up to $v = 14$ could be attempted.

Curve fits for all the cases were generated over the spectral range 1780 - 2220 cm^{-1} and for the time intervals shown in Table VI. The time increment between curve fit spectra was 0.2 msec. Data is available for times 0.2 - 15.0 msec at 0.1 msec intervals for more detailed analysis

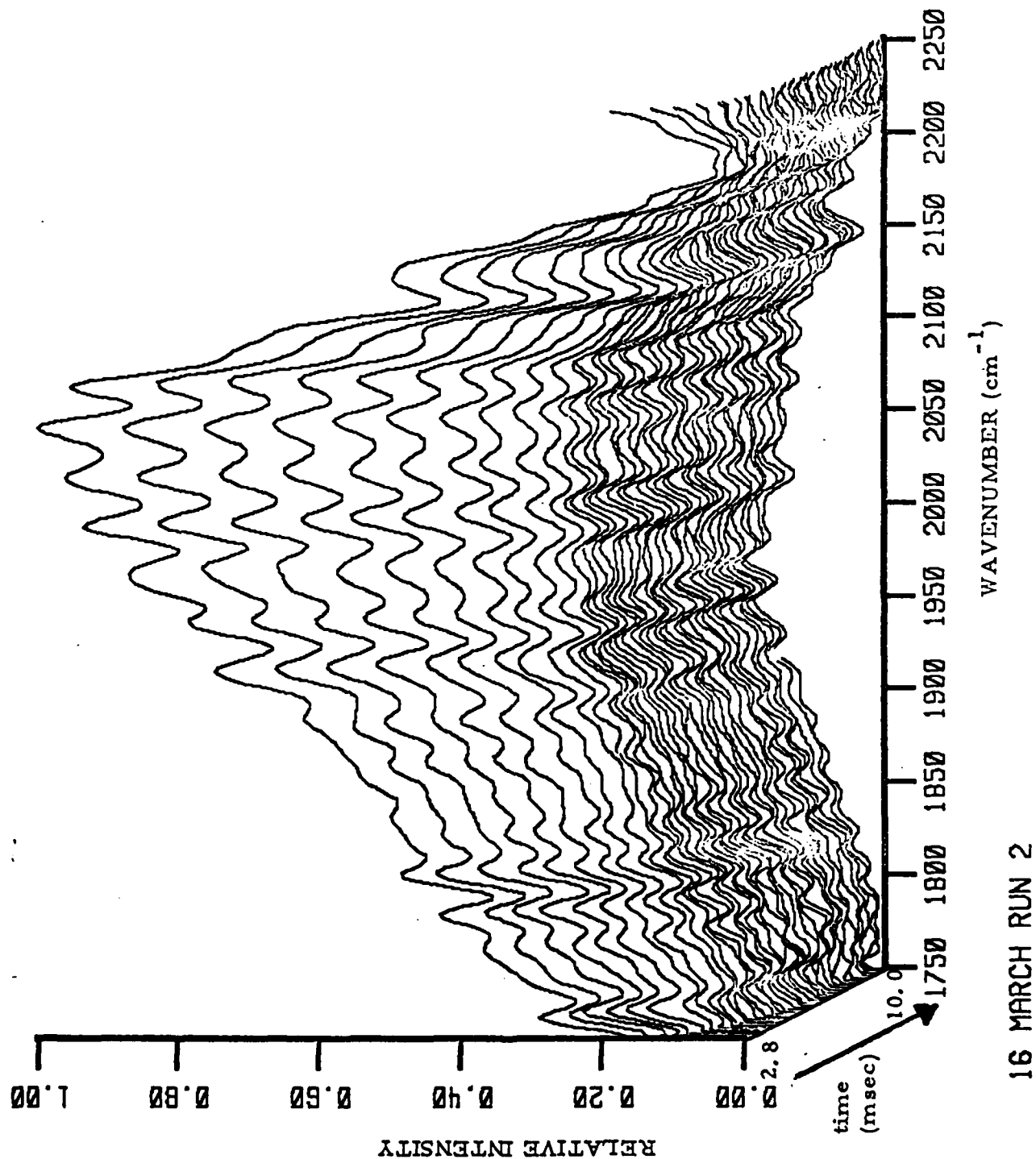


Fig. 41. CO fluorescence spectra after beam termination plotted every 0.2 msec from 2.8 - 10.0 msec for 16MARCH RUN 2.

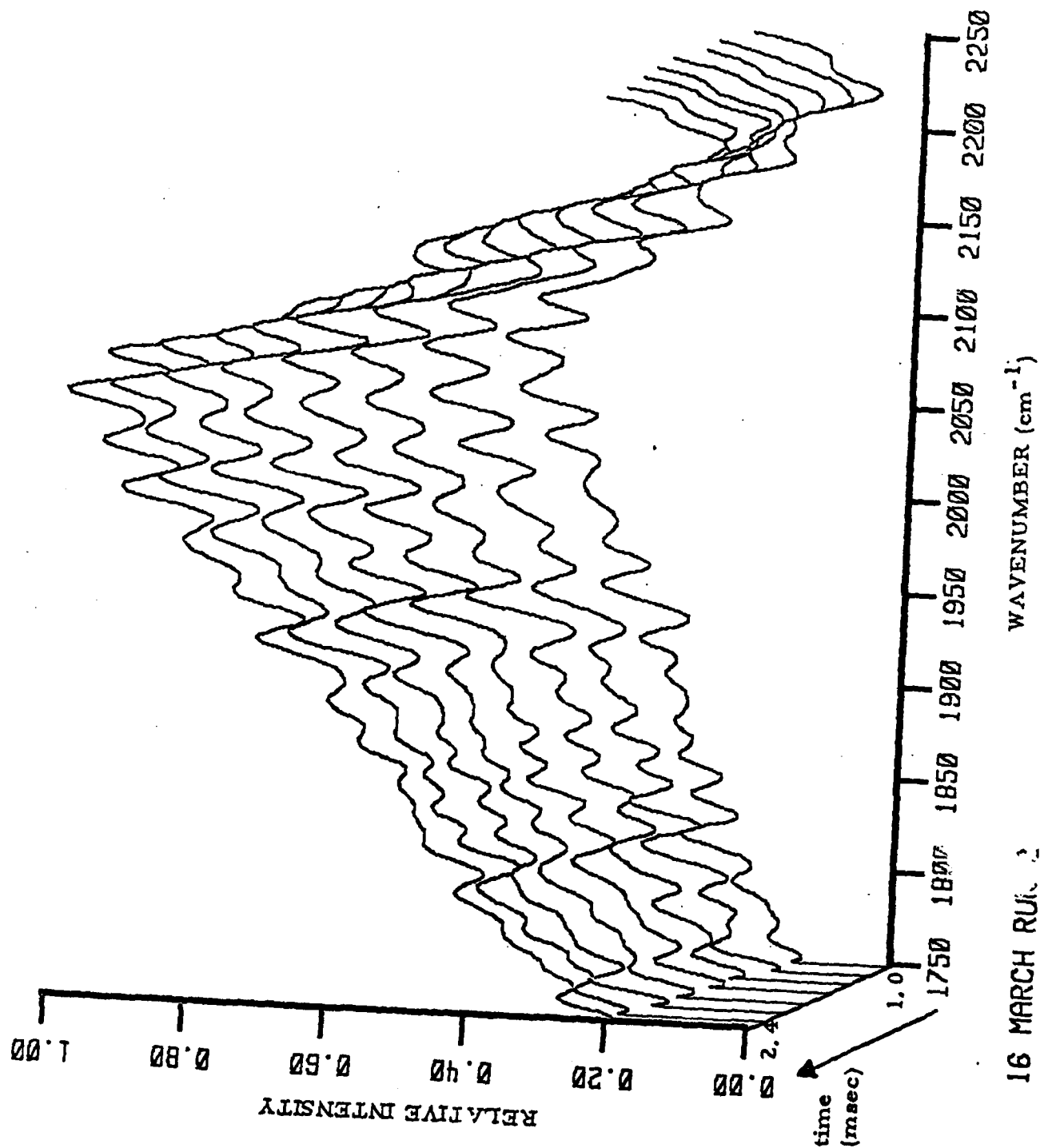


Fig. 42. CO fluorescence spectra during beam pulse plotted at 0.2 msec intervals between 1.0 and 2.4 msec for 16MARCH RUN 2. The time axis is reversed from the previous figure.

if required. Curve fits to the data of 11MARCH2 are representative and are shown in comparison to the data in Figs. 43 - 47 for different times after beam termination. The individual basis functions are plotted along the bottom of each figure and represent the relative contribution of each transition to the total intensity. It is seen that agreement is excellent not only for times near beam termination (Fig. 43) but even at times as long as 9.3 msec after beam termination (Fig. 47).

The spectral oscillations in the data are excellently matched in the $1900 - 2200 \text{ cm}^{-1}$ region of Figs. 43 - 45. The noise level in the signal prevents exact matching in the $1780 - 1900 \text{ cm}^{-1}$ region, but the intensity envelope is well matched. Transitions with $v=11-14$ fall in this region, and although the calculated populations are reasonably accurate, the estimated errors are larger than for the lower, better fit levels. At long times (Figs. 46 and 47) the intensity has decreased sufficiently so that some noise is evident even in the $1900 - 2200 \text{ cm}^{-1}$ range, degrading the quality of the fit slightly. The excellent agreement of the fits and data in the region of the non-overlapped $v = 1$ R branch transition tends to substantiate the choice of 300°K as the Boltzmann rotational temperature.

Attempts at fitting the data down to 1700 cm^{-1} yielded poorer results due to non-convergent oscillations in the predicted populations. These arise due to the overlapping of the basis functions and are an artifact of the non-linear regression analysis. The effect of these large errors in the deduced populations of $v = 15 - 17$ propagates back to lower vibrational states. The present preliminary analysis represents a compromise between maximum use of spectral information and minimum error propagation, and n_{14} is the maximum value used in all subsequent analysis. Improved fitting methods are currently being investigated to permit an increase in the reliability of the deduced populations of $v > 14$. The value of n_{14} is somewhat uncertain,

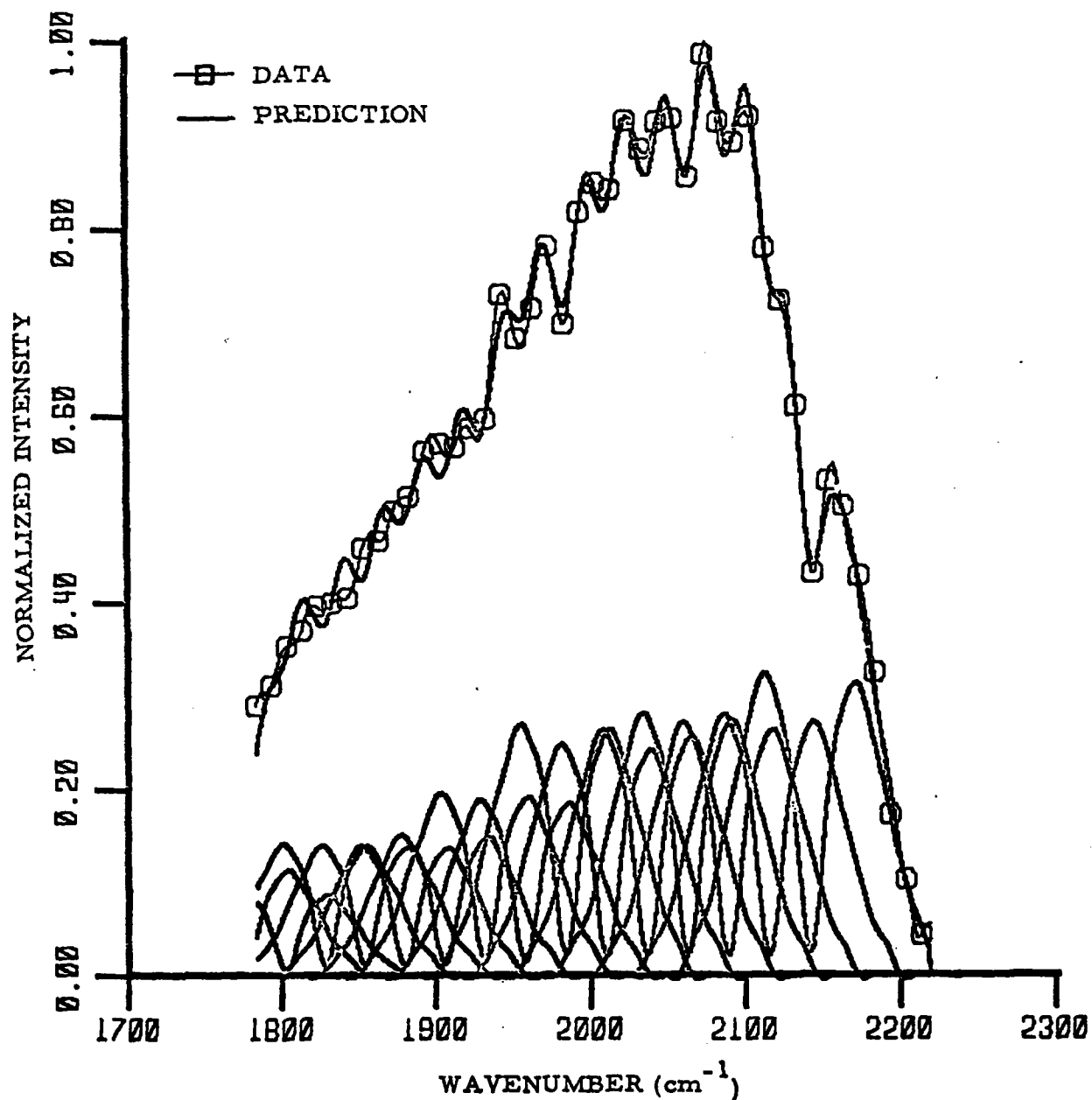


Fig. 43. Curve fit to data of 11MARCH RUN 2 at 0.3 msec after beam termination. Fit is performed over the spectral range 1780 - 2220 cm^{-1} . The basis functions are displayed along the bottom axis. Resolution is 10 cm^{-1} . The maximum intensity of the data is $4.33 \times 10^{-6} \text{ W/str-cm}^{-1}$.

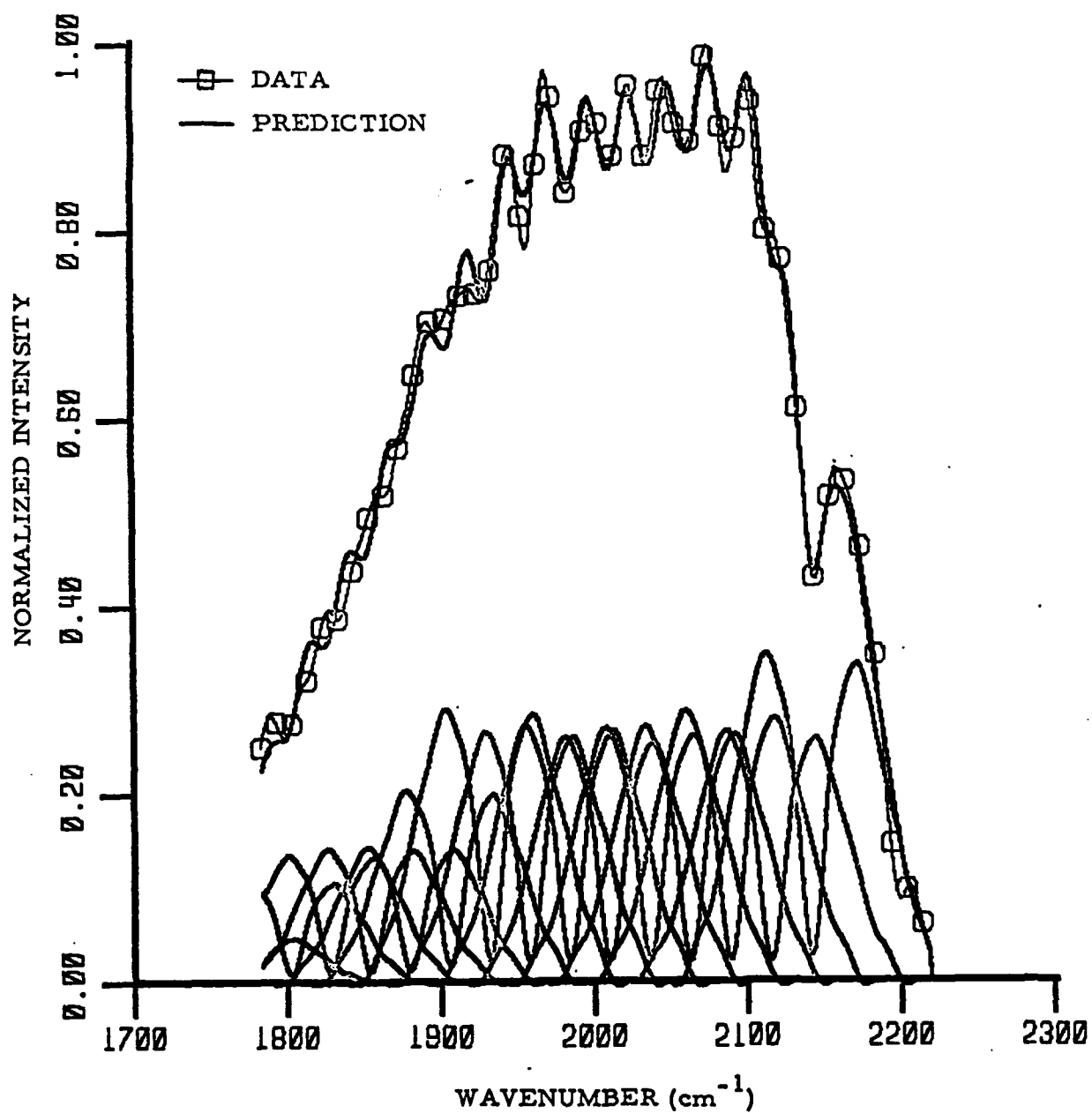


Fig. 44. Curve fit to data of 11MARCH RUN 2 at 2.5 msec after beam termination conditions as in Fig. 43. The maximum intensity of the data is $1.54 \times 10^{-6} \text{ W/str-cm}^{-1}$.

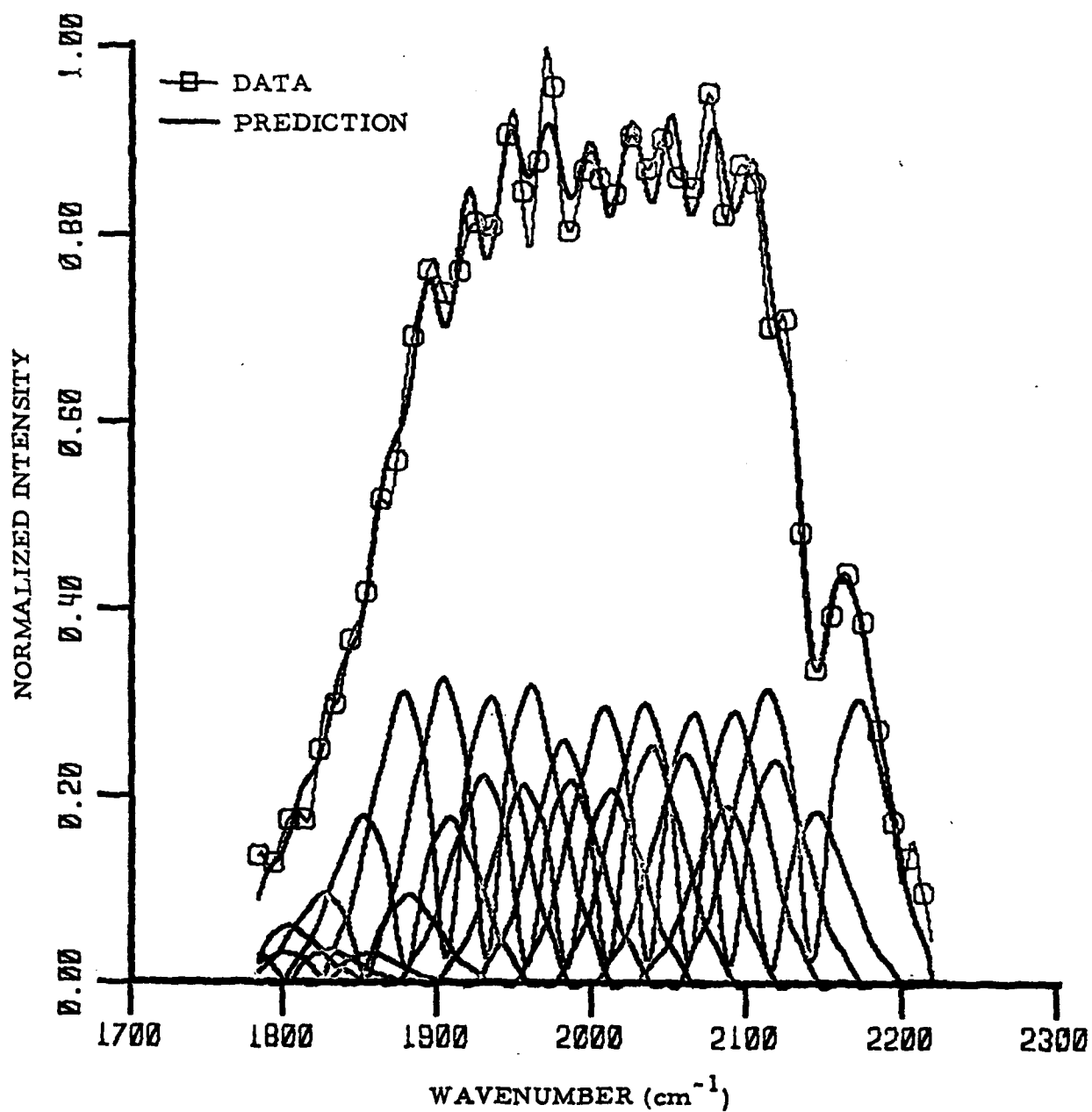


Fig. 45. Curve fit to data of 11MARCH RUN 2 at 4.7 msec after beam termination conditions as in Fig. 43. The maximum intensity of the data is $1.22 \times 10^{-6} \text{ W/str-cm}^{-1}$.

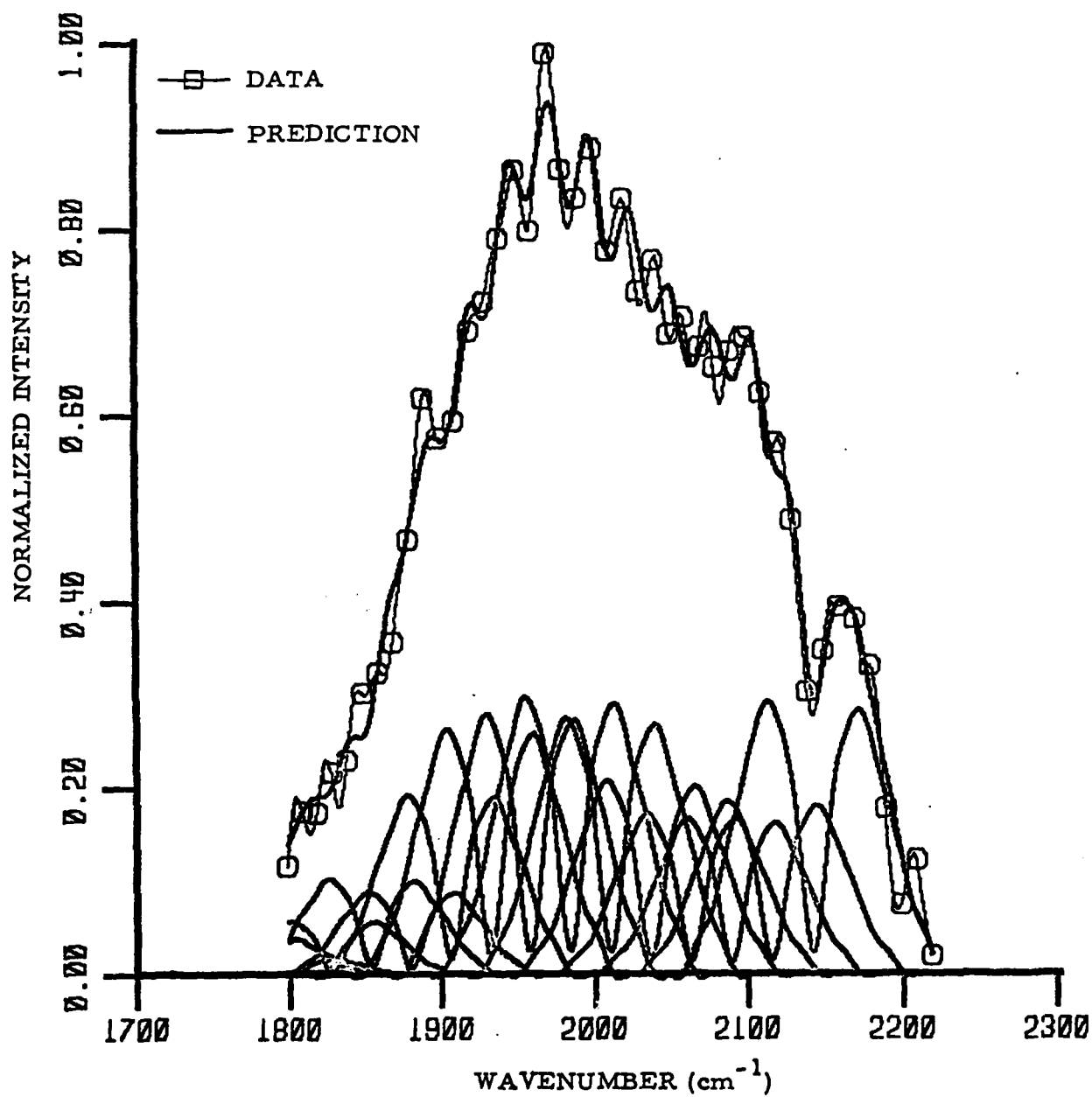


Fig. 46. Curve fit to data of 11MARCH RUN 2 at 7.9 msec after beam termination conditions as in Fig. 43. The maximum intensity of the data is $1.1 \times 10^{-6} \text{ W/str-cm}^{-1}$.

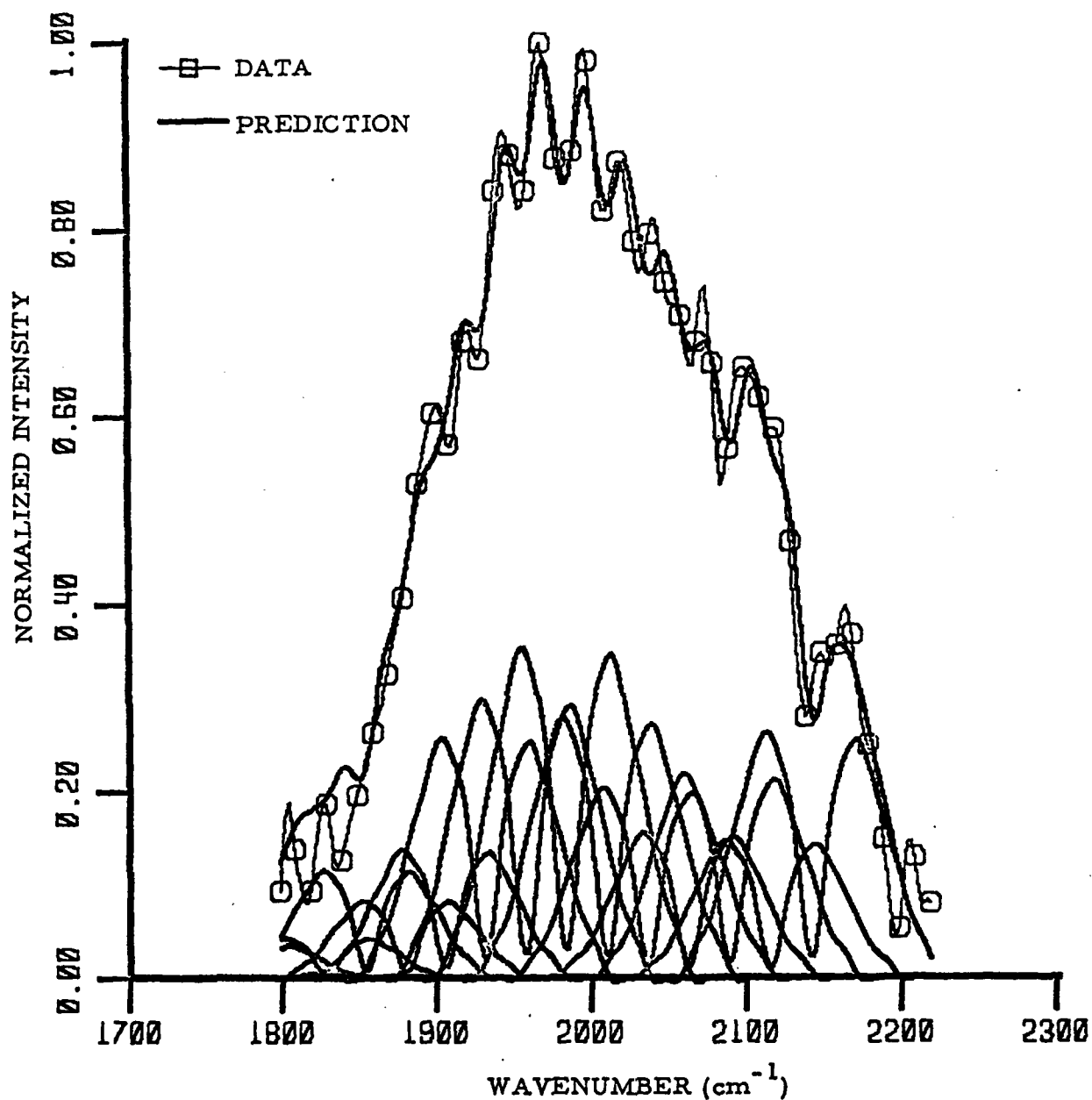


Fig. 47. Curve fit to data of 11MARCH RUN 2 at 9.3 msec after beam termination conditions as in Fig. 43. The maximum intensity of the data is $7.7 \times 10^{-7} \text{ W/str-cm}^{-1}$.

in the present state of the analysis, but small in magnitude. It is believed that higher lying levels would have even smaller populations and thus may be neglected.

As observed previously,² both the highest and lowest vibrational levels decay more rapidly than the middle levels. This is graphically evident in the intensity data as may be seen by comparison of Figs. 43 and 47. The relative decays are more clearly illustrated in Fig. 48 where the calculated populations of the levels are plotted at various times for the 11MARCH2 case. At the earliest time plotted, 2.8 msec (cf Fig. 43), the population density monotonically decreases with increasing v . With increasing time the population of level 7 decays more slowly than the surrounding levels, and a relative population inversion over levels 4 - 6 is observed at the longest times shown.

The calculated population histories as a function of time are shown in Figs. 49 and 50 for the 16MARCH3 case. The populations are plotted at 0.8 msec intervals (every fourth fit). The first five levels decay linearly with time, indicating a first order exponential decay rate. The broken line represents the calculated population of level 1 of the data of 11MARCH1. This data was taken with a nominal experimental CO_2 pressure of 0.2 torr and the CO fluorescence decay of this case is observed to be approximately twice as fast as the 16MARCH RUN 3 data which was taken with 0.1 torr nominal CO_2 pressure. Note that levels 4 - 7 are found to decrease more slowly with time than the lower vibrational levels and that n_6 is approximately equal to n_5 at long times. In Fig. 50 it is seen that levels 8 - 10 decay very slowly. Furthermore competition between loss to lower levels and feeding by the higher levels is evident; the population of level 9 actually increases at times below 4.2 msec as a result of feeding from higher levels. The highest levels shown, 11 - 14, are not fed by quanta from still higher levels and thus slowly decay (although population fluctuations due to spectral

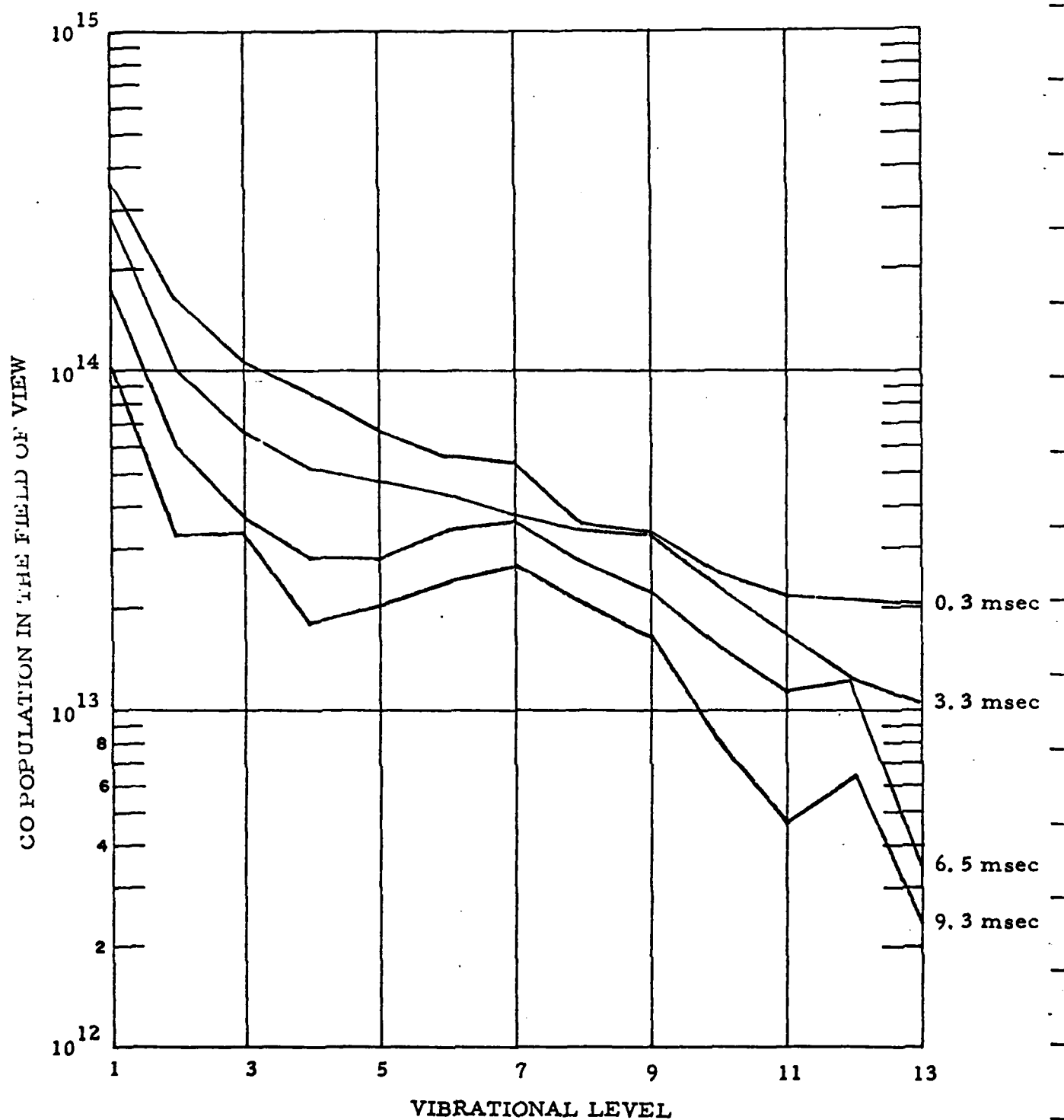


Fig. 48. Population of vibrationally excited CO in the field of view as a function of vibrational level for several different times after beam termination for 11 MARCH RUN 2 case.

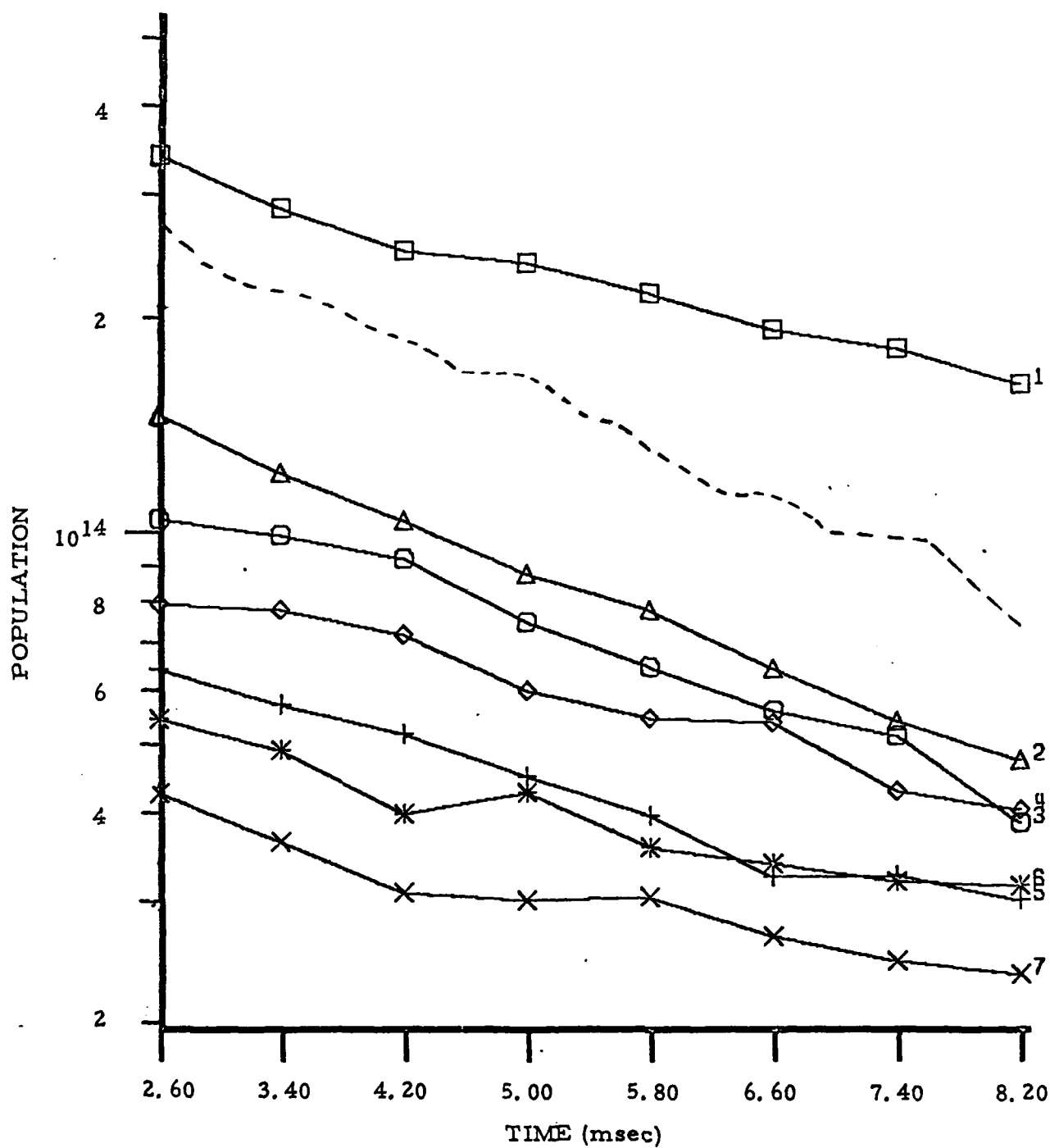


Fig. 49. Populations of CO in levels $v = 1 - 7$ within the field of view as a function of time after beam onset for 16 MARCH RUN 3 case. Beam termination occurs at 2.5 msec. Broken line is population of level 1 from 11 MARCH RUN 1 which has a greater CO_2 density.

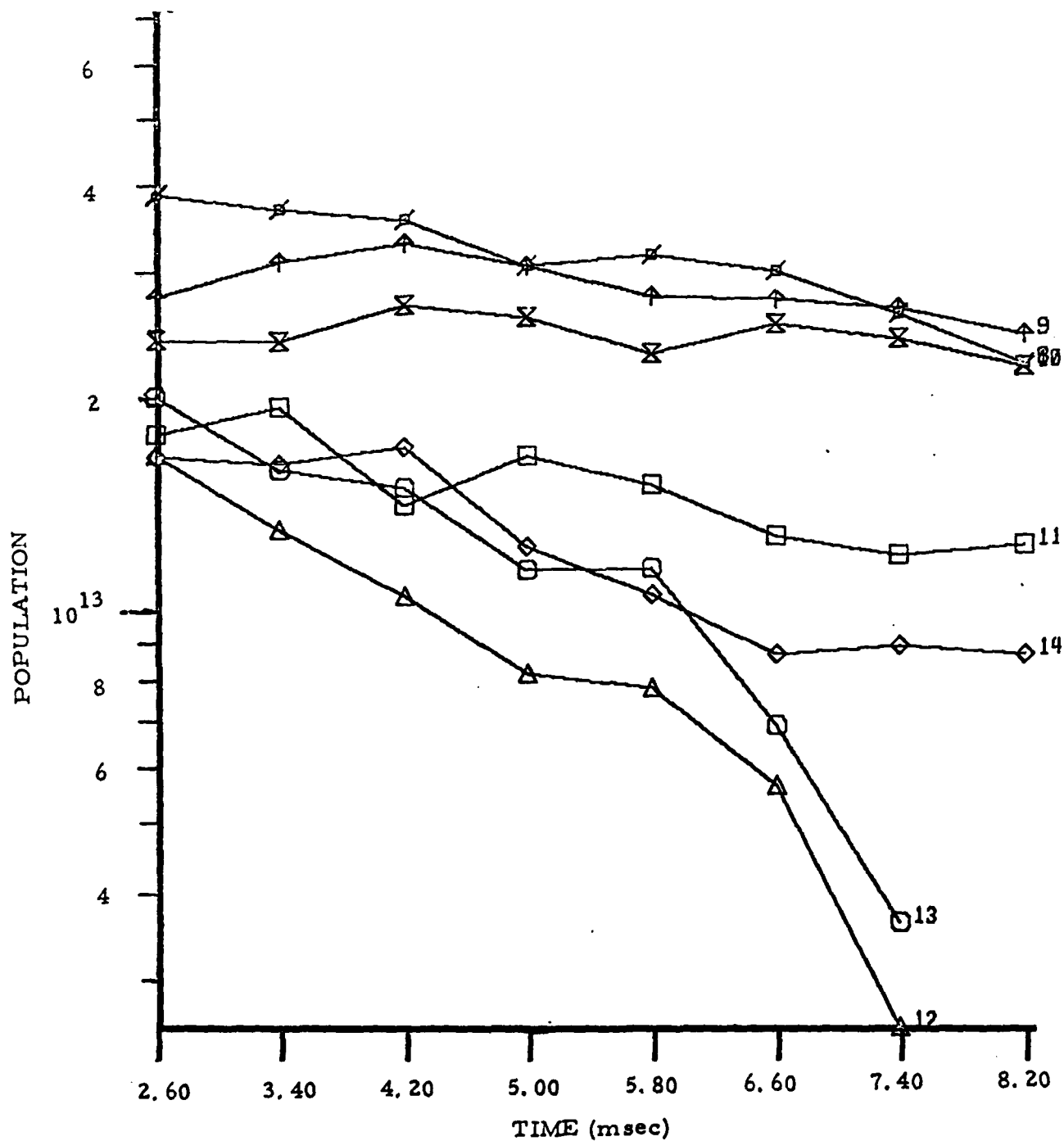


Fig. 50. Populations of CO in levels $v = 8 - 14$ within the field of view as a function of time after beam onset for 16 MARCH RUN 3 case. Beam termination occurs at 2.5 msec.

noise and fitting oscillations tend to obscure the decay). The value of n_{14} plotted is artificially high at the expense of level 12. Additional data scrubbing and fitting will be pursued in an effort to determine the population decay more accurately. It is clear from Figs. 49 and 50 that the very slow decay rate of levels 8 - 10 provides for a bottleneck preventing the efficient relaxation of CO vibrationally excited to $v > 8$.

A kinetic analysis of the relaxation phenomena was performed using the preliminary results for all the runs of Table VI. The effects of CO self-relaxation should be small for the predicted densities of beam created CO present in the field of view.² A more accurate estimate of these effects requires a larger data base covering a range of beam created CO concentrations. Uncertainties in the deduced n_v values prevent application of the standard time derivative rate equation. Under these circumstances, the relaxation of the vibrationally excited CO by CO_2 is more accurately determined by a time integral form developed previously:²

$$n_v(t_2) - n_v(t_1) = a_{v+1} R_{v+1} - a_v R_v + A_{v+2 \rightarrow v} a_{v+2} - A_{v \rightarrow v-2} a_v \quad (50)$$

where $n_v(t)$ is the deduced population of level v at time t and

$$a_v = \int_{t_1}^{t_2} n_v dt \quad (51)$$

In Eq. (50)

$$R_v = k_v [\text{CO}_2] + A_{v \rightarrow v-1} \quad (52)$$

where k_v is the rate constant for vibrational relaxation by reaction (40), $[\text{CO}_2]$ is the CO_2 number density, cm^{-3} , and the $A_{v \rightarrow v-1}$ and $A_{v \rightarrow v-2}$ are the fundamental and overtone transition Einstein coefficients respectively.

The direct determination of a_v from the vibrational population histories allows evaluation of Eq. (50) for R_v . Specifically a decrease in the total population of vibrationally excited CO can result only from fundamental radiation from level 1, overtone radiation from level 2 and collisional relaxation from level 1, therefore

$$\sum_{v=1}^{\infty} (n_v(t_2) - n_v(t_1)) = - a_1 R_1 - a_2 A_{2 \rightarrow 0} \quad (53)$$

The remaining R_v 's can then be found through the relationship

$$\sum_{v=1}^{n-1} (n_v(t_2) - n_v(t_1)) = - a_1 R_1 - A_{2 \rightarrow 0} a_2 + a_n R_n + A_{n+1 \rightarrow n-1} a_{n+1} + A_{n+2 \rightarrow n} a_{n+2} \quad (54)$$

Unfortunately, the relaxation data is available only for $n < 14$, and higher levels must be neglected in the summations of Eqs. (53) - (54). This omission will most seriously affect the upper levels, which were already noisy, and levels 8 - 10 where the quantity $(n_v(t_2) - n_v(t_1))$ is small. Variation of the number of levels included in the kinetic analysis revealed that the solutions became more stable as the number of levels included in the analysis was increased, as long as the populations of the higher levels were reasonably estimated. Inclusion of populations which exhibit oscillatory fluctuations between adjacent levels or neglecting levels which have significant populations such as n_{14} , n_{13} , or n_{12} lead to physically unrealizable values of R_v ($R_v < A_{v \rightarrow v-1}$).

The values of R_v determined for the 8 runs of Table VI are shown in Fig. 51. Shown for comparison are the Einstein coefficients $A_{v \rightarrow v-1}$. The R_v 's were evaluated over the maximum time interval for which population information was available; this choice of integration time minimizes the effects of uncertainties in the data. The spread in the R_v values is due in part to the variation in experimental CO_2 concentrations between cases. It can be seen that the relaxation of levels 9 - 13 is dominated by the radiative emission term in Eq. (52). Consequently, the relaxation rates, k_v , for these levels, as determined from the small differences between the values of R_v and $A_{v \rightarrow v-1}$, will have large uncertainties associated with them.

The nominal experimental CO_2 concentrations present in the irradiated mixture are the values listed in the second column of Table VI. However, because the relaxation rate constant for level 1 is well known,²¹⁻²⁴ the actual CO_2 concentration in the field of view may be found by requiring that the deduced k_1 equal the literature value. The CO_2 concentrations determined in this manner are listed in the last column of Table VI. The k_v values, calculated from R_v using these latter values for the CO_2 number density, are plotted in Fig. 52. The rates are smoothly varying and reasonably consistent between runs. The maximum relaxation rates occur at levels 2 and 3. The scatter in the data increases with vibrational level beyond level 7 reflecting the uncertainty in the populations of the higher levels. The rates deduced for levels 11 - 13 are essentially order of magnitude determinations. The broken line plotted in Fig. 52 represents the data of Hancock and Smith.²⁵ At large v their rate constants fall at upper end of the scatter in the present determinations. The factor of three difference in the rate constants for levels 4 - 6 was observed in our previous analysis and is still not understood. The present results exhibit good run-to-run reproducibility, however possible relaxation effects due to cold CO cannot be completely precluded.

These deduced relaxation rates may now be used in the determination of the electron beam production rates of vibrationally excited CO. The

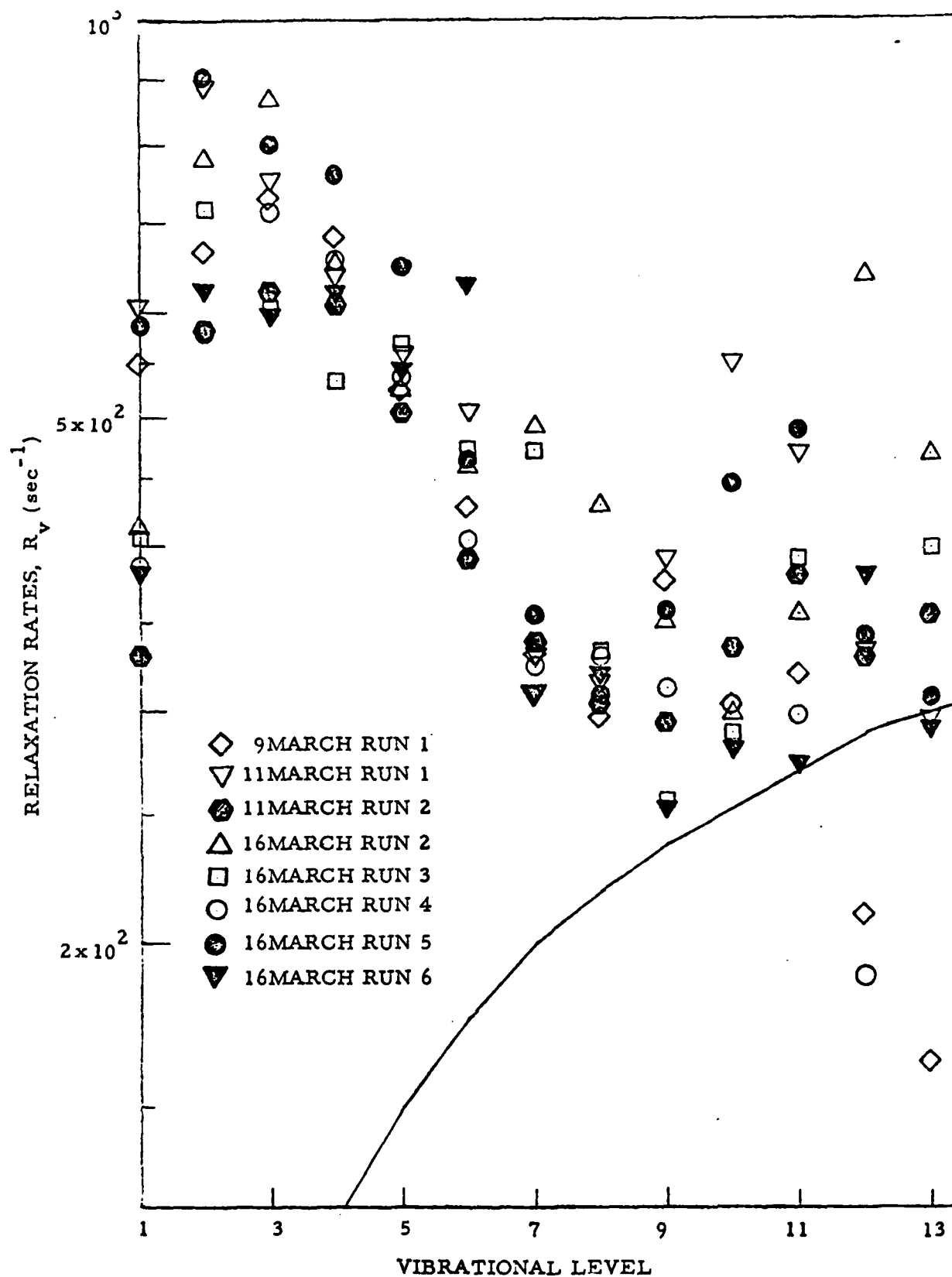


Fig. 51. The absolute relaxation rates for the eight runs in Table VI plotted as a function of vibration level. Solid line represents the fundamental transition Einstein coefficients.

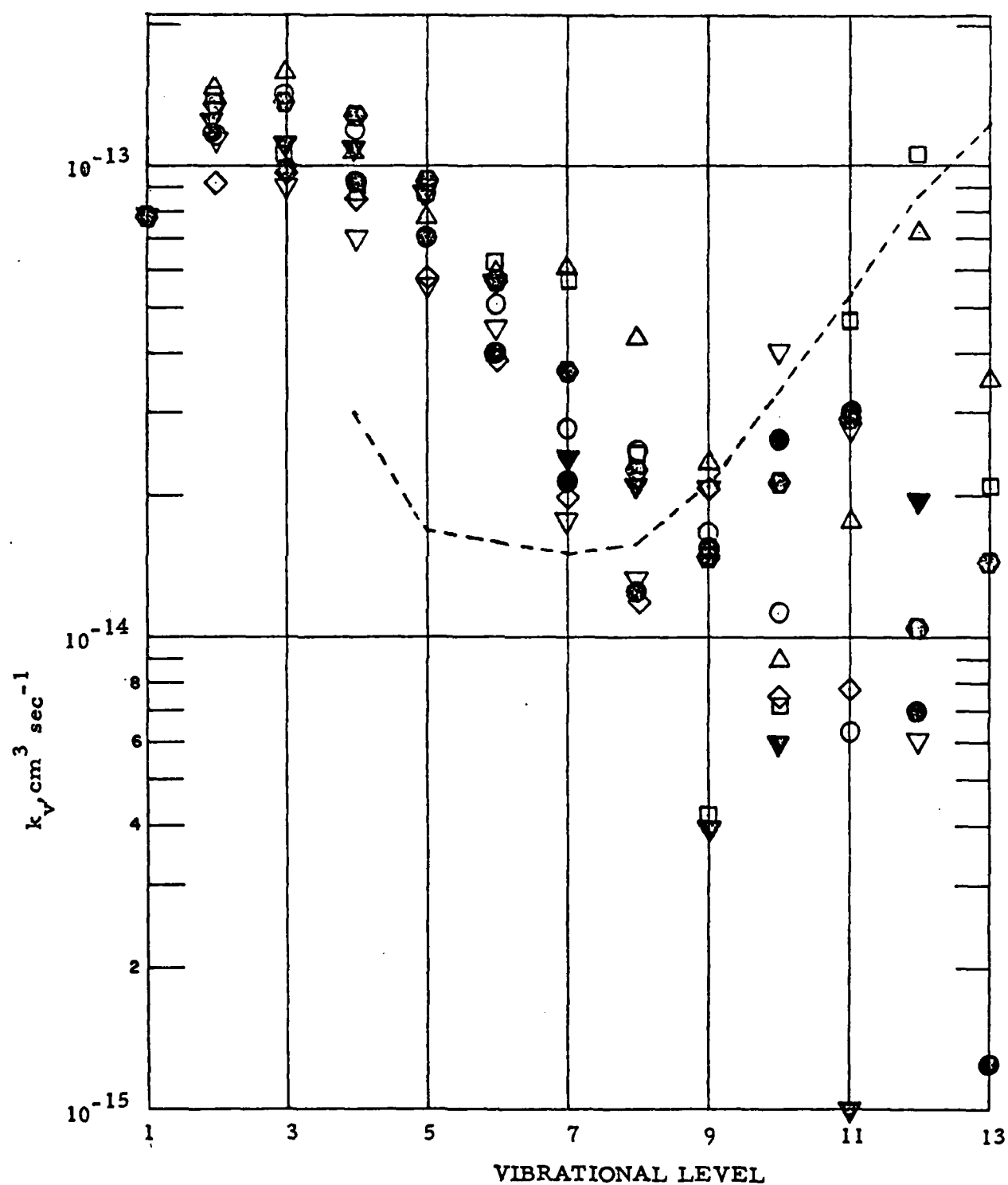


Fig. 52. Relaxation rates for the eight runs analyzed. The experimental CO_2 value is chosen such that k_1 agrees with the literature value. The broken line represents the data of Hancock and Smith.²⁵ Runs are designated as in Fig. 51.

fluorescence data observed while the beam is on, such as that shown in Fig. 42 was fit in the manner described above. The spectra at early times, immediately after beam onset, are quite noisy and the quality of the curve fit is poor. Typical fits are displayed in Figs. 53 - 55 for the data of 11MARCH1 at times of 0.6, 1.4 and 2.4 msec. The fit improves as the signal level increases. The calculated relative vibrational populations deduced from the fits to the data of 16MARCH3 are shown in Fig. 56. The populations of levels 1 - 5 increase linearly while the beam is on, with populations decreasing with increasing vibrational level. Levels 6 - 12 increase more slowly with the exception of level 9 which has a low relative population at $t = 1.0$ msec and then begins to increase rapidly. It was shown earlier that the population of this level continues to increase after beam termination; thus the increasing in population of this level appears to be due to vibrational cascade from higher levels rather than from direct beam creation.

Kinetic analysis of the excitation data is similar in form to the relaxation, but a term for the absolute rate of creation of CO molecules in level v , $R_e(v)$, must be included:

$$n_v(t) - n_v(t=0) = R_e(v)t + a_{v+1} R_{v+1} - a_v R_v + A_{v+2 \rightarrow v} a_{v+2} - A_{v \rightarrow v-2} a_v \quad (55)$$

Equation (55) may be evaluated directly inasmuch as the quantities a_v are found from the n_v histories and R_v was determined in the relaxation analysis. The integral is taken over the range 0.0 - 2.4 msec ($n_v(t=0) = 0$). Because the energy deposition within the field of view has only been modeled for a 30 kV electron beam this analysis was only performed for the runs taken at this voltage. The values of $R_e(v)$ deduced from these runs are presented in Fig. 57. The absolute creation rate is highest for $v = 1$ and decreases with increasing level.

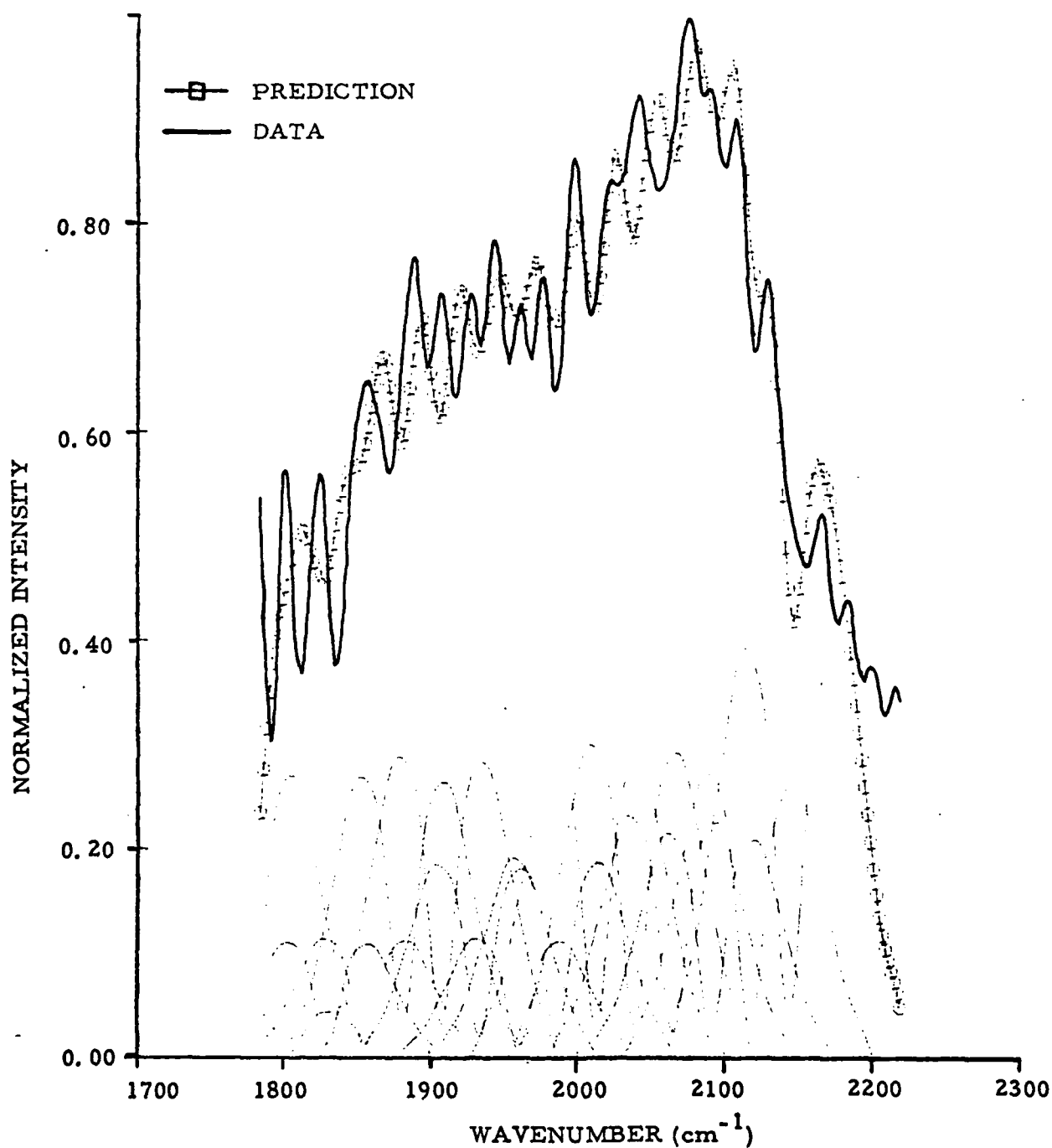


Fig. 53. Curve fit of 11MARCH RUN 1 data at 0.6 msec after beam initiation. Fit is performed over the spectral range 1780 - 2220 cm^{-1} . The basis functions are displayed along the bottom axis. Resolution is 10 cm^{-1} .

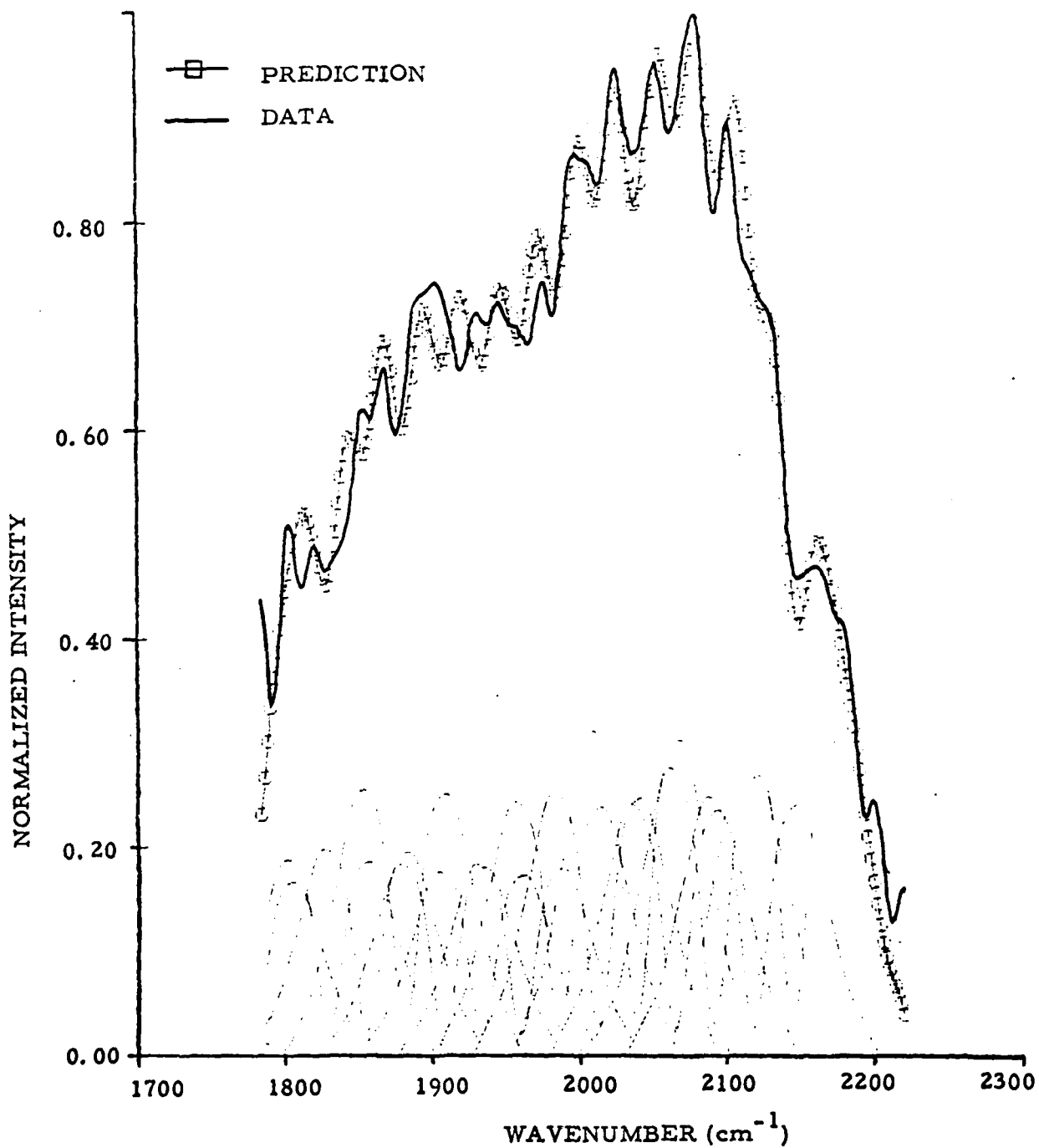


Fig. 54. Curve fit of 11 MARCH RUN 1 data at 1.4 msec after beam initiation.

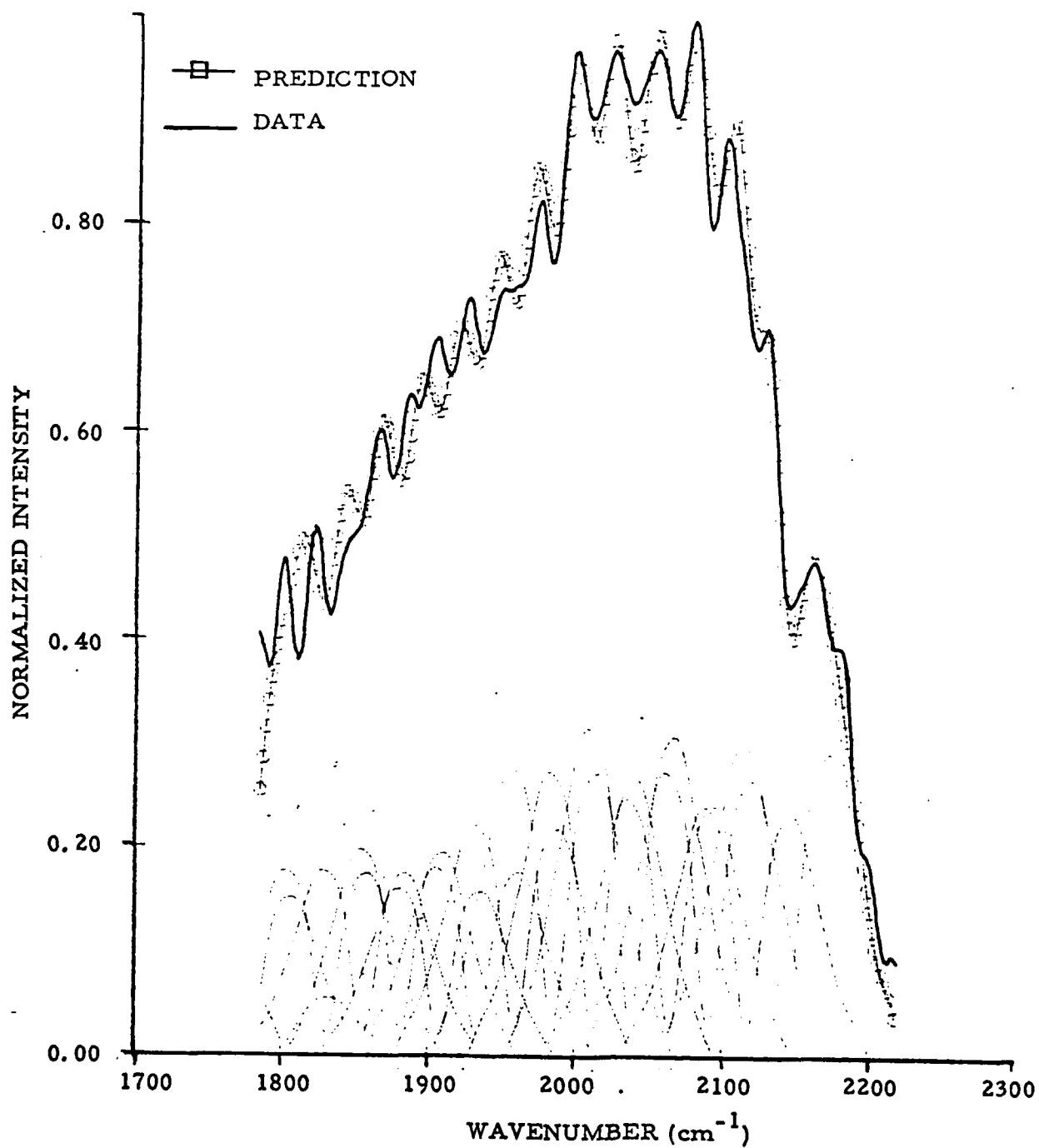


Fig. 55. Curve fit of 11MARCH RUN1 data at 2.4 msec after beam initiation (0.1 msec before beam termination).

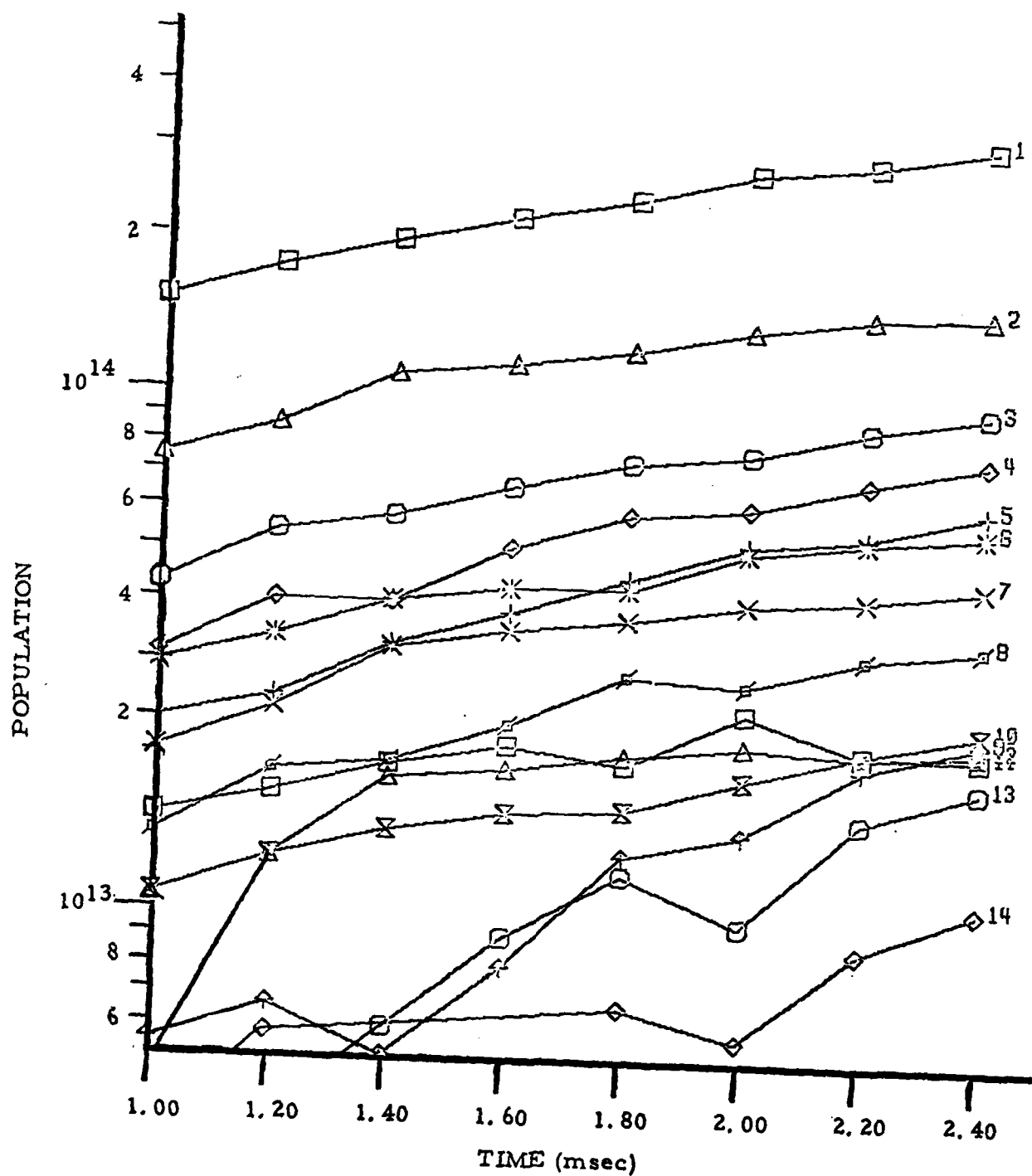


Fig. 56. Population of CO in levels $v = 1 - 14$ within the field of view as a function of time after the onset of the beam.

If the observed excitation rates are linearly proportional to the energy deposition, plots of R_e/I vs v for all six runs should be identical. (This is because the beam voltages and gas pressures of all cases considered are the same.) Such a comparison is made in Fig. 58 where the error bars represent one standard deviation from the average of the data points. The standard deviations are less than 10% for the first seven levels and even the four highest levels have less than 30% error bars.

The sum of the $R_e(v)$ values for a run represents the total CO creation rate in the field of view. These values can be compared with the total ion pair production rate in the field of view which is given by

$$\dot{x}^+ = \frac{I_p \left(\frac{1}{\rho} \frac{dE}{dx} \right) L_f g'}{eW} \text{sec}^{-1} \quad (56)$$

where the numerator is the energy deposition within the field of view, which was calculated in Section III, e is the electronic charge, and W is the average energy required to produce an ion pair, 26.1 eV for argon. Values of these quantities for the six runs are listed in Table VII. It is seen that approximately four vibrationally excited CO molecules are created per ion pair. Additionally, the average excitation of a vibrationally excited CO molecule is found to be

$$\frac{\sum E_v R_e(v)}{\sum R_e(v)} = 7090 \pm 260 \text{ cm}^{-1} \quad (57)$$

or approximately 3.3 quanta per vibrationally excited molecule. (E_v is the vibrational energy of level v .) The numerator of expression (57) is the total beam power converted to CO vibrational energy. This quantity, which is in the range 0.07 - 0.10 watts for the six runs, is also tabulated

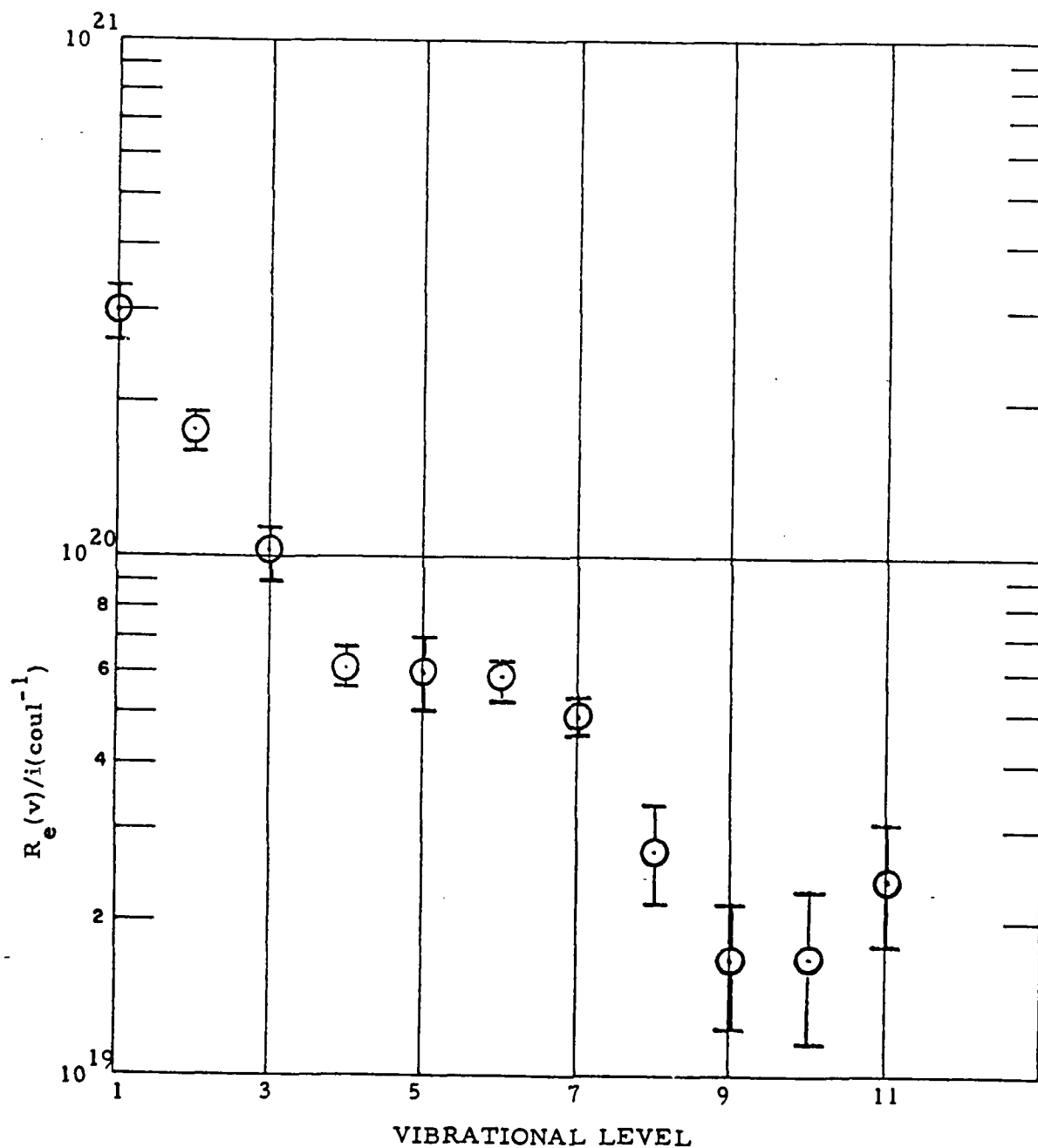


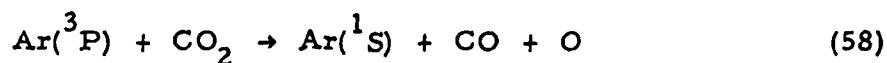
Fig. 58. The effective excitation rates per unit energy deposition for the six 30 kV runs. Error bars indicate standard deviation.

TABLE VII
CO EXCITATION PROPERTIES

Date	ΣR_e (sec^{-1}) $\times 10^{-17}$	Energy Deposited (W)	\dot{x}^+ (sec^{-1}) $\times 10^{-17}$	$\frac{\Sigma R_e}{\dot{x}^+}$	Average Vibrational Excitation	$\dot{\epsilon}_{\text{VIB}}$ (W)	Efficiency (%)
9MARCH 1	5.0	.85	2.03	2.5	3.48	.073	8.6
11MARCH 1	6.3	.96	2.29	2.8	3.36	.088	9.2
11MARCH 2	6.5	1.16	2.77	2.3	3.32	.092	7.9
16MARCH 2	7.1	1.21	2.89	2.5	3.34	0.100	8.3
16MARCH 3	6.5	1.12	2.67	2.4	3.23	.088	7.9
16MARCH 4	7.1	1.13	2.70	2.6	3.25	.097	8.6
Averages				2.5	3.33		8.4 $\pm .2$

in the Table. From knowledge of the total energy deposited, the average efficiency for electron energy conversion to CO vibration excitation is found to be $8.4 \pm 4\%$. The large error bars are again due to uncertainties in the energy deposition and interferometer alignment.

One of the more intriguing aspects of this analysis is the deduction that approximately 2.5 vibrationally excited CO molecules are created per ion pair. This value is of course inversely proportional to the energy deposited within the field of view, which requires more careful evaluation. Nonetheless it is of some interest to speculate on possible production sources for CO. The dominant production mechanism assumed previously² was dissociative recombination of CO_2^+ , Eq. (39), which would provide for at least one CO molecule per ion pair. It has also been found from the energy allocation predictions of Section III, see Fig. 40, that approximately 0.6 electronically excited Ar atoms are created per ion pair. Although only a fraction of these are metastable states, those electronic states which do have optically allowed transitions to the ground state will be optically trapped at the experimental pressures and thus will either radiatively cascade to metastable states or be quenched in collisions with CO_2 . These quenching collisions will most likely be dissociative as has been shown in the case of argon metastables,²⁶ i. e.,



Thus reactions (39) and (58) can account for at least 1.6 CO molecules per ion pair.

Furthermore both of these reactions are highly exo-ergic and have been observed²⁶⁻²⁸ to produce electronically excited states such as $\text{CO}(a^3\pi)$. This latter metastable state will be dominantly quenched by collisions with CO_2 under the present experimental conditions, most likely via the dissociative process²⁸



$\text{CO}(a^3\pi)$ formation has been observed in CO_2^+ recombination. Wauchop and Broida²⁸ found that 55% of the CO_2^+ created through Penning ionization collisions recombined to form $\text{CO}(a^3\pi)$. If reaction (58) created $\text{CO}(a^3\pi)$ with unit efficiency, the total CO creation rate would be at most 2.75 per ion pair. Note that metastable $\text{O}(^1\text{S})$ could also be produced by reactions (39) and (58). Preliminary studies²⁹ however, indicate that CO is not produced in quenching collisions between $\text{O}(^1\text{S})$ and CO_2 .

Thus out of a theoretical maximum of 2.75 CO created per ion pair, 2.5 are experimentally observed as being created vibrationally excited. It must be emphasized that the CO data analysis is not yet complete and the results presented above may be revised when a more detailed analysis is concluded. On the other hand, the deactivation rate constants and relative excitation rates deduced in the present analysis are in good agreement with those determined previously.²

V. SUMMARY AND CONCLUSIONS

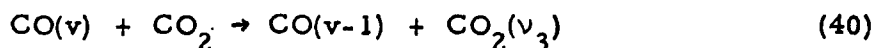
An absolute calibration has been developed for interferometric infrared measurements on the LABCEDE facility. The relative response of the system across the field of view has been mapped out and, to first order, is radially symmetric about the center of the field of view and may be described by a Gaussian distribution. The net effect of this non-uniform response, is that effectively only one-fourth of the irradiation resulting from a uniform source filling the field of view will be detected by the system. This fractional collection efficiency can of course be different if the fluorescence source itself is non-uniform; a range of values has been provided for anticipated electron beam shapes. It is clear that a significant improvement in signal to noise, without a concomitant decrease in spectral resolution, can be achieved by introducing collimating telescopic optics between source and interferometer. Such a system modification would also simplify data interpretation.

The absolute calibration has been used to analyze CO_2 fluorescence data observed in electron irradiated mixtures of CO_2/Ar in an effort to determine the fraction of deposited beam energy transferred to the $\text{CO}_2(\nu_3)$ mode. The main complication in this determination is the evaluation of the absorptive losses. These have been determined for the case of Voigt broadened radiative transitions, undergoing absorption by Voigt broadened lines in the test chamber, under the assumption of a non overlapping line model. Additional losses due to absorption by ambient CO_2 along the optical path have also been evaluated. Predicted $\text{CO}_2(\nu_3)$ spectral signatures have been compared with measurements for conditions covering a range of test chamber total and CO_2 partial pressures, and ambient CO_2 concentrations. In general agreement between prediction and data has been found to be very good with small differences most likely due to breakdown in the non-overlapping

line assumption. These spectral differences are not anticipated to have a significant effect on the total predicted band intensity.

Through this modeling it was found that 88 - 94% of the chamber $\text{CO}_2(\nu_3)$ fluorescence is re-absorbed. By applying this correction to the measured band intensities it was found that the efficiency of 30 kV electrons for exciting the $\text{CO}_2(\nu_3)$ made in mixtures of 9 torr Argon/0.1-0.2 torr CO_2 was $9\% \pm 4\%$. Perhaps the largest uncertainties in determining this excitation efficiency are in specifying the total beam energy deposited within the field of view and in gauging the effects of interferometer misalignment on absolute intensities. A careful evaluation of this quantity will be provided in future work. Furthermore, data taken at other beam voltage and chamber pressure conditions remains to be reduced. It should also be noted that the presence of beam created species may provide for a lower $\text{CO}_2(\nu_3)$ excitation efficiency than would be obtained in pure mixtures of Ar/ CO_2 .

Preliminary analysis of the CO fundamental vibrational band fluorescence data has provided a set of rate constants for the processes



The statistical uncertainty in these rates becomes quite large for vibrational levels greater than $v = 7$ reflecting in part uncertainties in the populations of the higher vibrational levels. The vibrational level dependent production rates for CO have also been deduced. When normalized by the rate of beam energy deposition, these quantities are found to be remarkably consistent from run to run. Preliminary estimates are that approximately $8 \pm 4\%$ of the deposited beam energy is transferred to CO vibrational energy and that ~ 2.5 excited CO molecules are created per ion pair with average excitation level of 3.3 vibrational quanta. A more careful analysis will include the effects of the beam created species CO and O on both the relaxation and production rates. This analysis has continued under a separate contract.

Lastly, it should be clear that the development of the absolute calibration was a complicated procedure, involving both non-uniform sources and response functions. A computer code to provide a more exact solution of the detector's response to the non-uniform electron beam source should be developed. Given the usefulness of this calibration in determining absolute creation rates and the beam excitation efficiencies, it is felt that the process should be repeated carefully with both experimental and theoretical crosschecks made wherever possible. After this has been accomplished the techniques discussed in this report could be used to determine other absolute electron beam excitation efficiencies such as those for forming vibrationally excited NO and N_2 in air.

VI. ACKNOWLEDGEMENTS

The authors would like to thank Drs. T. Rawlins and J. S. Goela and Mr. H. Murphy for their assistance in performing this study. The computing analysis was capably provided by Mr. E. Tomaszewski and Ms. M. Staniewicz. Drs. R. Murphy and A. Fairbarn of the Air Force Geophysics Laboratory provided consulting support throughout the duration of this effort.

PRECEDING PAGE BLANK-NOT FILMED

VII. REFERENCES

1. R. E. Murphy, F. H. Cook and H. Sakai, "Time Resolved Fourier Spectroscopy", J. Opt. Soc. Amer. 65, 600 (1975).
2. R. E. Murphy, F. H. Cook, G. E. Caledonia and B. D. Green, "Infrared Fluorescence of Electron Irradiated CO₂ in the Presence of N₂, Ar and He", Air Force Geophysics Laboratory TR-77-0205, Environmental Research Papers No. 609, 15 September 1977.
3. B. D. Green, G. E. Caledonia, and R. E. Murphy, "SWIR-MWIR Electron Fluorescence Measurements in N₂/O₂ and Air," Air Force Geophysics Laboratory TR-78-00083, Environmental Research Paper No. 629, 4 April 1978.
4. D. Baker, "Field Widened Interferometers for Fourier Spectroscopy" in Spectrometric Techniques, Vol. I, ed. by G. A. Vanasse (Academic Press, New York, 1977), pp. 71 - 106.
5. R. E. Center "Plural and Multiple Scattering of Fast Electrons in Gases", Phys. Fluids 13, 79 (1970).
6. J. T. Yardley and C. B. Moore, "Intramolecular Vibration-to-Vibration Energy Transfer in Carbon Dioxide", J. Chem. Phys. 46, 4491 (1967).
7. E. E. Whiting, "An Empirical Approximation to the Voigt Profile", J. Quant. Spectrosc. Radiat. Transfer 8, 1379 (1968).
8. J. J. Olivers and R. L. Longbothum, "Empirical Fits to the Voigt Linewidth: A Brief Review", J. Quant. Spectrosc. Radiat. Transfer 17, 233 (1977).
9. J. H. Pierluissi and P. C. Vanderwood, "Fast Computational Algorithm for the Voigt Profile", J. Quant. Spectrosc. Radiat. Transfer 18, 555 (1977).
10. R. A. McClatchey, W. S. Benedict, S. A. Clough, D. E. Burch, R. F. Calfee, K. Fox, L. S. Rothman and J. S. Garing, "AFCRL Atmospheric Absorption Line Parameters Compilation", AFCRL-TR-73-0096, January 1973.
11. G. Herzberg. Molecular Spectra and Molecular Structure I, Spectra of Diatomic Molecules (D. Van Nostrand Co., New York, 1951), 2nd ed., p. 208.

12. M. J. Berger and S. M. Seltzer, "Tables of Energy Losses and Ranges of Electrons and Positrons", NASA SP-3012, 1964.
13. F. H. Brittain, "A Description of ELTRAN: An Electron Deposition Code", Sandia Laboratories report SC-TM-68-713, 1969, as supplied by Oak Ridge National Laboratory RISC Computer Code Collection.
14. L. R. Peterson, T. Sawada, J. N. Bass and A. E. S. Green, "Electron Energy Deposition in a Gaseous Mixture", *Comp. Phys. Comm.* 5, 239 (1973).
15. L. R. Peterson and J. E. Allen, Jr., "Electron Impact Cross Sections for Argon", *J. Chem. Phys.* 56, 6068 (1972).
16. T. Sawada, D. J. Strickland and A. E. S. Green, "Electron Energy Deposition of CO₂", *J. Geophys. Res.* 77, 4812 (1972).
17. C. H. Jackman, R. H. Garvey and A. E. S. Green, "Electron Impact on Atmospheric Gases I. Updated Cross Sections", *J. Geophys. Res.* 82, 5081 (1977).
18. G. Herzberg, Molecular Spectra and Molecular Structure I. Spectra of Diatomic Molecules, 2nd ed. (D. Van Nostrand Co., New York, 1951), pp. 106 - 109.
19. G. Schiffner and E. Klement, "Calculation of Improved ¹²C ¹⁶O Molecular Constants and Rotational-Vibrational Transition Frequencies", *Appl. Phys.* 6, 199 (1975).
20. K. Kirby-Docken, "Theoretical Study of Molecular Dipole Moment Functions I. The X¹Σ⁺ State of CO", *J. Chem. Phys.* 66, 4309 (1977).
21. J. C. Stephenson and C. B. Moore, "Temperature Dependence of Nearly Resonant Vibration-Vibration Energy Transfer in CO₂ Mixtures", *J. Chem. Phys.* 56, 1295 (1972).
22. W. A. Rosser, Jr., R. D. Sharma and E. T. Gerry, "Deactivation of Vibrationally Excited Carbon Dioxide (001) by Collisions with Carbon Monoxide", *J. Chem. Phys.* 54, 1196 (1971).
23. D. J. Miller and R. C. Millikan, "Vibration-Vibration Energy Exchange Between Carbon Monoxide and Carbon Dioxide", *Chem. Phys.* 6, 317 (1974).

24. D. F. Starr and J. K. Hancock, "Vibrational Energy Transfer in CO₂-CO Mixtures from 163 to 406°K", J. Chem. Phys. 63, 4730 (1975).
25. G. Hancock and L. W. M. Smith, "Quenching of Infrared Chemiluminescence 1. The Rates of De-Excitation of CO($4 \leq v \leq 13$) by He, CO, NO, N₂, O₂, OCS, N₂O and CO₂", Appl. Opt. 10, 1827 (1971).
26. W. L. Starr, "Dissociation-Excitation Reactions of Argon Metastables with Carbon Dioxide", J. Chem. Phys. 55, 5419 (1971).
27. R. A. Gutcheck and E. C. Zipf, "Excitation of the CO Fourth Positive System by the Dissociative Recombination of CO₂⁺ Ions", J. Geophys. Res. 78, 5429 (1973).
28. T. S. Wauchop and H. P. Broida, "Lifetime and Quenching of CO($a^3\Pi$) produced by Recombination of CO₂ Ions in a Helium Afterglow", J. Chem. Phys. 56, 330 (1972).
29. T. G. Slanger and G. Black, "O(¹S) Interactions - the Product Channels," J. Chem. Phys. 68, 989 (1978).

APPENDIX

This appendix is a direct reproduction of Physical Sciences Inc. report
TR-114, 10 January 1978.

PRECEDING PAGE BLANK-NOT FILMED

ABSTRACT

The infrared fluorescence of electron irradiated room air and mixtures of N_2/O_2 has been observed over the spectral range of $1600 - 6700\text{ cm}^{-1}$. Dominant spectral features include the NO fundamental and first overtone bands as well as the $CO_2(\nu_3)$ and $N_2O(\nu_3)$ fundamental bands. Comparisons between the spectra observed in room air and laboratory N_2/O_2 mixtures are provided.

1. INTRODUCTION

One of the main topics of discussion at the recent High Altitude Effects Simulation Infrared Data Review meeting¹ was the origin of and data base for 2.7 μm band radiation occurring in the quiescent and aurorally disturbed upper atmosphere. The short wave infrared data taken on several recent rocket flights were discussed and some comparisons with theoretical estimates were provided. These predictions were developed under the assumption that the dominant atmospheric radiation source in the 2.7 μm region is the NO first overtone vibration/rotation band. Although this thesis is generally accepted as valid it has not yet been verified experimentally inasmuch as to date upper atmospheric fluorescence measurements have been performed utilizing radiometers which allow little spectral resolution.

It was pointed out during the meeting² that there are several sets of measurements of 2.7 μm radiation which are not consistent with an NO source. Specifically, in some instances measurements of the total columnar 2.7 μm radiation as a function of altitude exhibit a behaviour typical of an optically thick source, whereas atmospheric NO is optically thin. Furthermore it was pointed out that the ratio of 2.7 μm to 5.3 μm band radiation observed in recent project EXCEDE measurements³ was much too large to be explained in terms of the ratio of the NO first overtone to fundamental band radiation. Lastly some laboratory measurements of electron irradiated air⁴ were shown to exhibit spectral features due to a species other than NO.

Of course it can be argued that the aforementioned data were either anomalous or affected by contaminants. Indeed the laboratory spectra of Ref. 4 was later found to be contaminated by HF, which was formed in some

complex manner from teflon spacers positioned inside the test chamber. In any event the final resolution of this conflict must await spectrally resolved measurements of the atmospheric radiation. Nonetheless it can be of some interest to define alternate atmospheric sources of $2.7 \mu\text{m}$ radiation which would be consistent with the data base.

Such an analysis has recently been performed² and it was concluded that atmospheric CO_2 is the most likely additional source of $2.7 \mu\text{m}$ radiation. It is well known that radiation from the CO_2 combination bands ($101 \rightarrow 000$) and ($021 \rightarrow 000$) will fall in the $2.7 \mu\text{m}$ region. These transitions are typically⁵ taken to be $1/25$ th as weak as the corresponding fundamental band transitions ($101, 021 \rightarrow 100, 020$). It was pointed out however that if these transitions were only one fourth as weak as the fundamental transition they could prove to be a significant source of $2.7 \mu\text{m}$ radiation and indeed could provide radiation signatures similar to the anomalous observations discussed above.

The purpose of the present study was to examine, under laboratory conditions, the spectrally resolved fluorescence in the $2.7 \mu\text{m}$ region occurring in electron irradiated air, and to identify the molecular sources of this radiation. This was done utilizing the room temperature LABCEDE facility which requires total operating pressures greater than one torr. It must be emphasized that this device does not simulate upper atmospheric conditions. Specifically a high degree of collisional quenching will occur in the test chamber and this quenching can obscure radiative phenomena which might be dominant at the lower pressures of the upper atmosphere.

A description of the test facility and the techniques used in taking the fluorescence data is presented in Section II. The data analysis and interpretation may be found in Section III and summary and conclusions are provided in Section IV.

II. EXPERIMENTAL

The LABCEDE facility is a room temperature apparatus designed to study the fluorescence of electron beam irradiated gas mixtures. In this device a constant pressure, continuously flowing gas is irradiated by a collimated, mono-energetic electron beam. The infrared fluorescence from the irradiated gas target is monitored in a plane perpendicular to the excitation beam. This fluorescence may be both spectrally and temporally resolved through use of a computer interfaced Michelson interferometer. Because of signal to noise limitations the device cannot be operated at gas pressures below approximately one torr and thus cannot be used to provide an exact simulation of processes occurring in the upper atmosphere, e.g. $H \geq 80$ km. In the present studies the observation region flow and pressure conditions, as well as beam current and voltage, were chosen to maximize the fluorescence intensity in the short wavelength infrared (SWIR) near $2.7 \mu\text{m}$.

The LABCEDE apparatus has been described in detail elsewhere,⁶⁻⁹ and only an overview of the facility will be presented here. The electron beam is operated in a pulsed mode and in the present study was characterized by a square wave pulse of 2.5 msec duration and period (25 msec 10% duty cycle). The electrons are accelerated through an adjustable 32 - 36 kV potential drop, focussed, and sequentially passed through three pin hole nozzles which form a differential pumping network. The differential pumping permits observation chamber operation at pressures of up to 150 torr while maintaining pressures below 10^{-3} torr in the electron gun. The electron beam current reaching the observation chamber is largely determined by the amount of beam spreading prior to the last pinhole nozzle. The flow and pressure in the observation

region directly affect the nozzle chamber pressure due to pump loading, and thus can affect the amount of beam scattering loss for a given run. Typical electron beam currents were 1 - 2 milliamps for 32 - 36 kV operation. The beam is maintained at approximately constant operating conditions during the course of a run; short term stability fluctuations and long term drift were both less than 5% of the total current level.

The gases are introduced into the chamber above and to the side of the beam entrance. Mixing of the test gases occurs just outside of the observation chamber. The gas flow rate is measured with a calibrated flowmeter and accurately controlled by knife-edge needle valves. The chamber pressure is monitored by MKS Baratron capacitance manometer with an atmospheric pressure head, referenced to the electron gun pressure.

The fluorescence is monitored by a lead-salt detector mounted at the exit plane of the scanning Michelson interferometer. The moving interferometer mirror, mounted on an oil driven piston, is continuously scanned. Relative mirror movement is monitored by the interference fringes resulting from a helium-neon laser beam positioned parallel to the fluorescent signal. Constructive interference fringes occur every time the mirror changes position by 0.316 microns. The mirror scanning rate is chosen so that on the average 40 beam pulses occur between laser fringes. The detector signal is bandpass amplified (PARC Model 113), interfaced with a Digital PDP-15 computer using an A/D converter, processed, and stored on magnetic tape.

Observation of the temporal dependence of the fluorescence spectrum is made possible by a sample and hold network referenced to the electron beam pulse onset.⁸ The network output is directly input into the A/D converter,

at sampled intervals less than the detection system response time. The A/D converter time resolution limitation is around 40 μ seconds, and for these experiments, the resolution limit is determined by the detector and amplification network. Because of the detector limitations it was not possible to measure the emission of the NO fundamental and first overtone vibration/rotation bands simultaneously. A PbSe detector, cooled to 77°K, was used to monitor fluorescence in the mid wavelength infrared region (MWIR) near 5 μ m. This detector had a 75 μ sec response time which was degraded to 200 μ sec by the bandpass amplifier in order to decrease the noise level. A PbS detector (at 195°K) was used for the SWIR measurements. This detector exhibits higher responsivity but is limited to a 2 millisecond response time.

Averaging of the appropriate detector intensities between laser fringes is performed to increase signal to noise. These averaged signal are then stored on magnetic tape as a single point in each of the time resolved interferograms. For all the experiments sufficient data points (at different mirror positions) were gathered to provide for 10 cm^{-1} spectral resolution. Degradation of the resolution to artificially decrease the apparent noise level could then be performed mathematically by the computer at a later time if desired.

The gases used in these experiments were ultrahigh purity nitrogen and oxygen, and room air. When use was made of room air, it was introduced into the chamber through the flowmeter and needle valve in order to match the cylinder gas flow conditions as closely as possible. The room air could be filtered to remove dust and water vapor by means of a glass wool/silica gel desiccant trap. This trapping system was found to be effective in removing water vapor from the laboratory air.

The infrared fluorescence intensity was found to be optimized at relatively slow flow conditions, 2.5 standard liters per minute total flow, with pumping of the test chamber occurring only through the electron beam differential pumping system. The optimized chamber operating pressure was 100 torr and the residence time of the test gas was 30 seconds. Under these flow conditions beam created species are likely to build up in the observation region. Specifically nitrogen and oxygen atoms are produced in the test gas either by direct electron impact dissociation or by subsequent electron/ion/neutral reactions. These atoms can then produce other chemical species such as NO, O₃, NO₂, N₂O. The present experiments are designed to study NO fluorescence resulting from the reactions



If the gas residence time is long compared to the beam pulsing time the amount of NO and other beam created species will increase pulse by pulse until reaching a steady state level. The details of the relevant chemical kinetics for N₂/O₂ mixtures may be found in Ref. 6. It is not anticipated that the presence of these beam created species will affect the conclusions of this study however their presence must be considered when interpreting the experimental observations.

Attempts to decrease the gas residence time result in a loss of fluorescent intensity. Increasing the flow and pumping rates at constant chamber pressure lead to beam current degradation; pressure reduction at constant flow causes a reduction in the total energy deposition of the beam within the field of view.

As a result, only slow flow measurements were made in the MWIR region. On the other hand, because of the greater sensitivity of the PbS detector, SWIR fluorescence measurements could be made both at the slow flow conditions and also at flow rates of 5 standard-liters per minute. For these latter flow rates, and a chamber pressure of 12 torr, the beam current degradation may be kept at an acceptable level, while the gas chamber residence time is decreased to 2 seconds. Consequently, in these measurements the build-up of beam created species is greatly reduced. Experiments performed in the past⁶ with an integrating sphere in the chamber have resulted in increased signal level at the expense of the residence time and field-of-view definition. No attempt was made to implement the integrating sphere in the present study.

Experimental measurements were first made in the MWIR region in order to observe the temporal behavior of the NO fundamental band radiation ($\Delta v = 1$) with 0.2 millisecond resolution. Additionally, the presence and relative strengths of radiation from $\text{CO}_2(\nu_3)$ and $\text{N}_2\text{O}(\nu_3)$ transitions at $4.3 \mu\text{m}$ and $4.5 \mu\text{m}$ could be examined. A series of slow flow runs using first a mixture of 80% N_2 /20% O_2 , then trapped (dried) room air, and finally unfiltered room air, were made keeping chamber pressure, beam current and voltage constant at 100 torr, 1.6 mA, and 36 kV respectively. When unfiltered air was used, no significant detector signal could be obtained. It is expected that the level of fluorescence in this case is diminished because of the efficient quenching of vibrationally excited states by water vapor.

A similar series of measurements was made in the SWIR, NO overtone, spectral region with the PbS detector. The experimental conditions of the MWIR measurements were duplicated as much as possible. Beam currents achieved

were slightly different, 1.2 mA - 1.8 mA, but all other parameters were unchanged. Because of the increased sensitivity of this detector, signal was observed even for the case of unfiltered air. Fast flow measurements were made with both cylinder gases and filtered room air at 36 kV, but at a reduced beam current of 0.9 - 1.4 mA. Although the magnitude of the beam current was decreased in these runs, the current stability was maintained at the 5% fluctuation level. The total fluorescence intensity for these cases was reduced by more than a factor of two below that of the slow flow cases.

An additional set of measurements at reduced oxygen partial pressures were made both in the MWIR and SWIR regions. At the same total pressure, it was found that mixtures with fractional oxygen concentrations of 1.2 - 3.0×10^{-4} of the nitrogen pressure provided the maximum NO fluorescence intensity. The total fluorescence intensity of these runs was a factor of four larger than those observed in the air mixtures.

The final collected data base included eight runs taken with the PbSe detector and fifteen runs taken with the PbS detector. In several instances measurements were repeated over a period of several weeks in order to ensure data reproducibility. Furthermore detector spectral response calibrations were performed daily using a black body radiation source. The collected experimental data (stored on magnetic tape) was processed by first sorting the data into time-resolved interferograms, Fourier transforming them into spectra, then applying a correction for detector spectral response and field-of-view. The final form of the reduced data is a series of time-resolved, calibrated spectra for each run. Spectral resolution, up to the maximum of 10 cm^{-1} , is

determined by the number of interferogram points included in the transformation.

These spectra are then used for species identification and kinetic analysis.

III. DATA ANALYSIS AND INTERPRETATION

The signal to noise ratio of the data taken in the MWIR was sufficiently low so that the observed spectra exhibited a "spikey" structure. The apparent noise level could be diminished by artificially degrading the spectral resolution to 20 cm^{-1} ; however, this had to be done with care inasmuch as real spectral features can be inadvertently washed out by this procedure.

A typical MWIR spectra, taken in a mixture of 80% N_2 / 20% O_2 at a total pressure of 100 torr, is shown in Fig. 1. This data was taken with the PbSe detector under slow flow conditions and corresponds to a time just prior to beam termination; the spectral resolution of the data has been degraded to 20 cm^{-1} . Two distinct spectral features are apparent. The first of these, spanning the spectral range of $1760\text{--}1925\text{ cm}^{-1}$, is the result of NO fundamental vibrational/rotational band fluorescence, arising from NO molecules with up to six quanta of vibrational excitation. Radiation from the N_2O (ν_3) band is also observed at 2223 cm^{-1} . Note that neither of these species is present in the original test gas and thus both must be created through chemical reactions such as (1) and (2). From a knowledge of the relevant Einstein coefficients^{5, 10}, it can be determined that the populations of the vibrationally excited NO and N_2O responsible for the fluorescence are in the ratio of seven to one. No other significant spectral radiators are observed in the bandpass of this detector. (The feature at 1630 cm^{-1} is an artifact of the spectral calibration.)

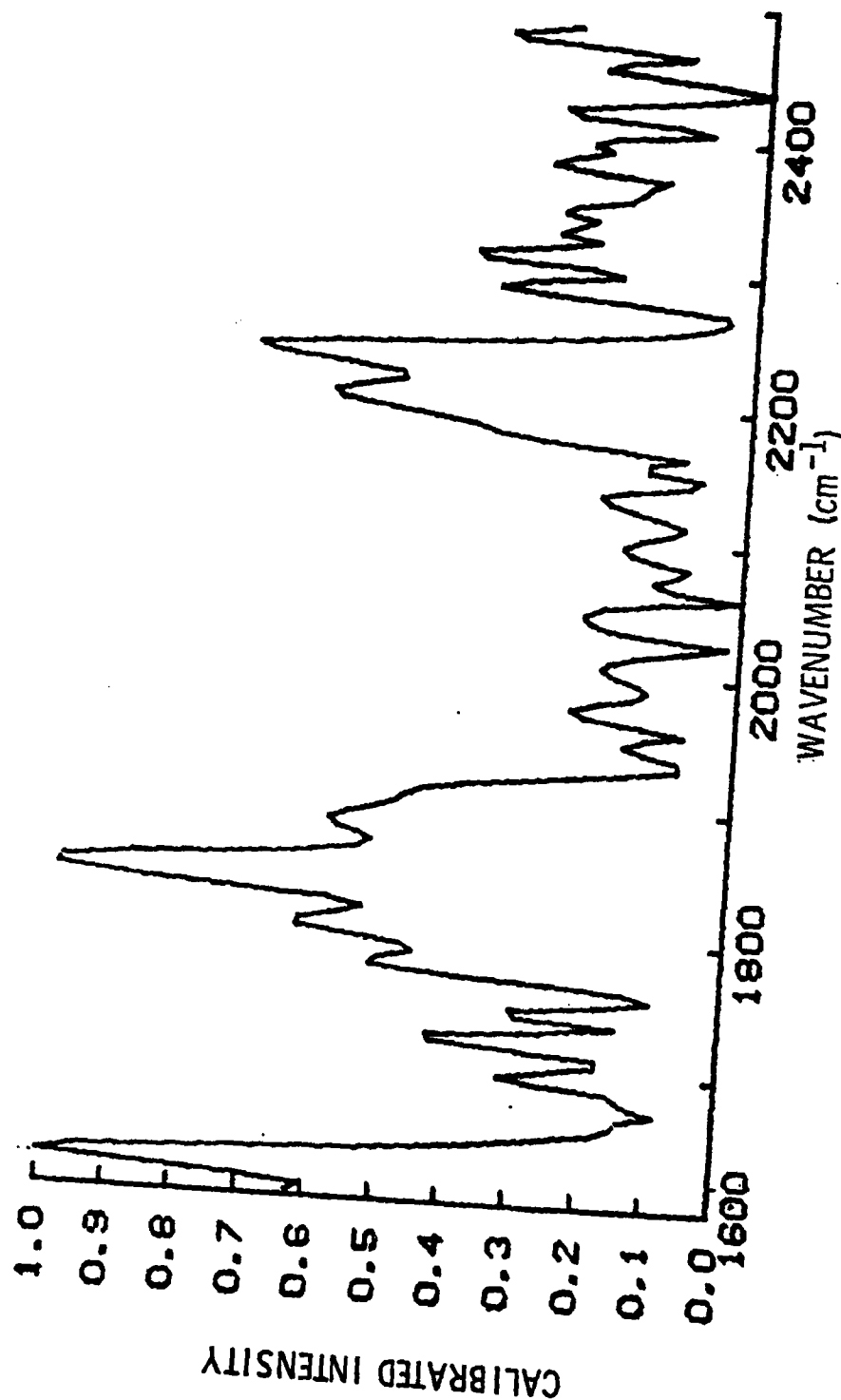


Figure 1: MWIR fluorescence at beam termination from 80% nitrogen/20% oxygen mixtures at 100 torr pressure, for slow-flow conditions. Resolution is 20 cm⁻¹. Electron beam current was 1.6 mA, voltage was 36 kV. NO and N₂O(ν_3) radiation are evident.

The same spectrum is shown in Fig. 2 at 10 cm^{-1} resolution. The large noise level is due to the combination of poor detector response and low fluorescence levels. It can be seen, however, that the basic spectral features of Figs. 1 and 2 are the same. The spectrum of Fig. 3 corresponds to the same case at a time of 0.2 msec after beam termination. The time difference between Figs. 2 and 3 is equal to the response time of the detection network. The intensity scale is the same for both figures and it can be seen that with increased time the fluorescence due to NO is greatly diminished, while the N_2O signal is essentially unchanged. The rate constants for vibrational quenching of NO ($v=1$) by N_2 and O_2 have been measured¹¹ as $1.7 \times 10^{-16} \text{ cm}^3/\text{sec}$ and $2.4 \times 10^{-14} \text{ cm}^3/\text{sec}$ respectively leading to a predicted NO fluorescence decay time of 0.07 msec for the present case. The observed NO decay is limited by the time resolution of the experiment. N_2O (v_3) quenching by N_2 has been measured¹² to have a rate constant of $4 \times 10^{-15} \text{ cm}^3/\text{sec}$, and thus the N_2O (v_3) fluorescence would be expected to decay on the same time scale, as NO, 10^{-4} seconds. The N_2O fluorescence in this experiment is observed to decay with a time constant of 20 msec, thus implying the presence of a source of N_2O vibrational excitation in the test gas after beam termination. Vibrationally excited molecular nitrogen (i. e., excited by beam electrons) is a known energy reservoir under these conditions⁶ and near-resonance vibrational exchange between N_2O (v_3) and N_2 (v) is postulated as an explanation for the observed slow N_2O decay. Specifically, the vibrational exchange reaction

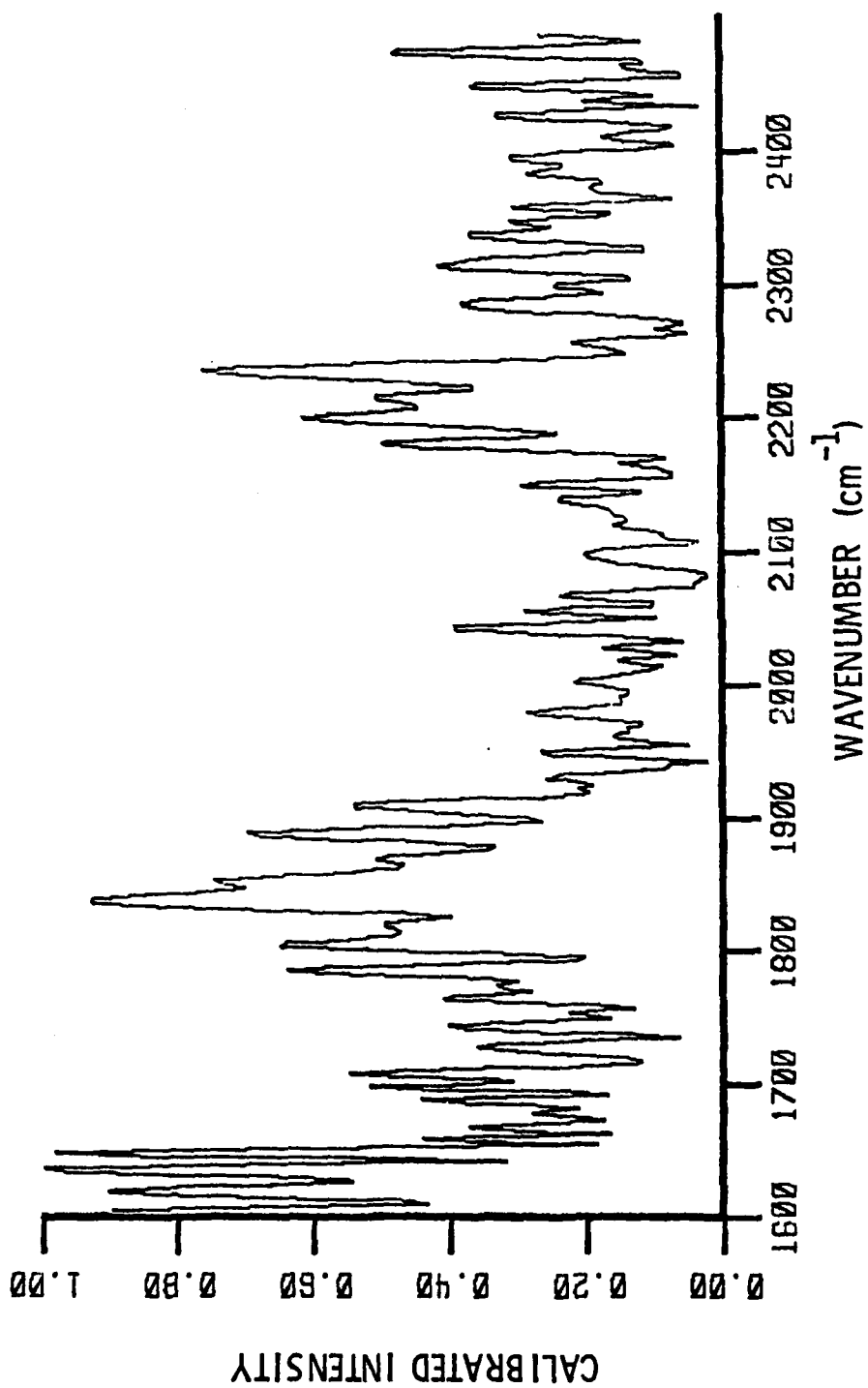


Figure 2: MWIR fluorescence of Fig. 1 at beam termination with 10 cm^{-1} resolution. Normalized to $I_{\text{max}} = 6.9 \times 10^{-9} \text{ W/cm}^2 \text{-str-cm}^{-1}$.

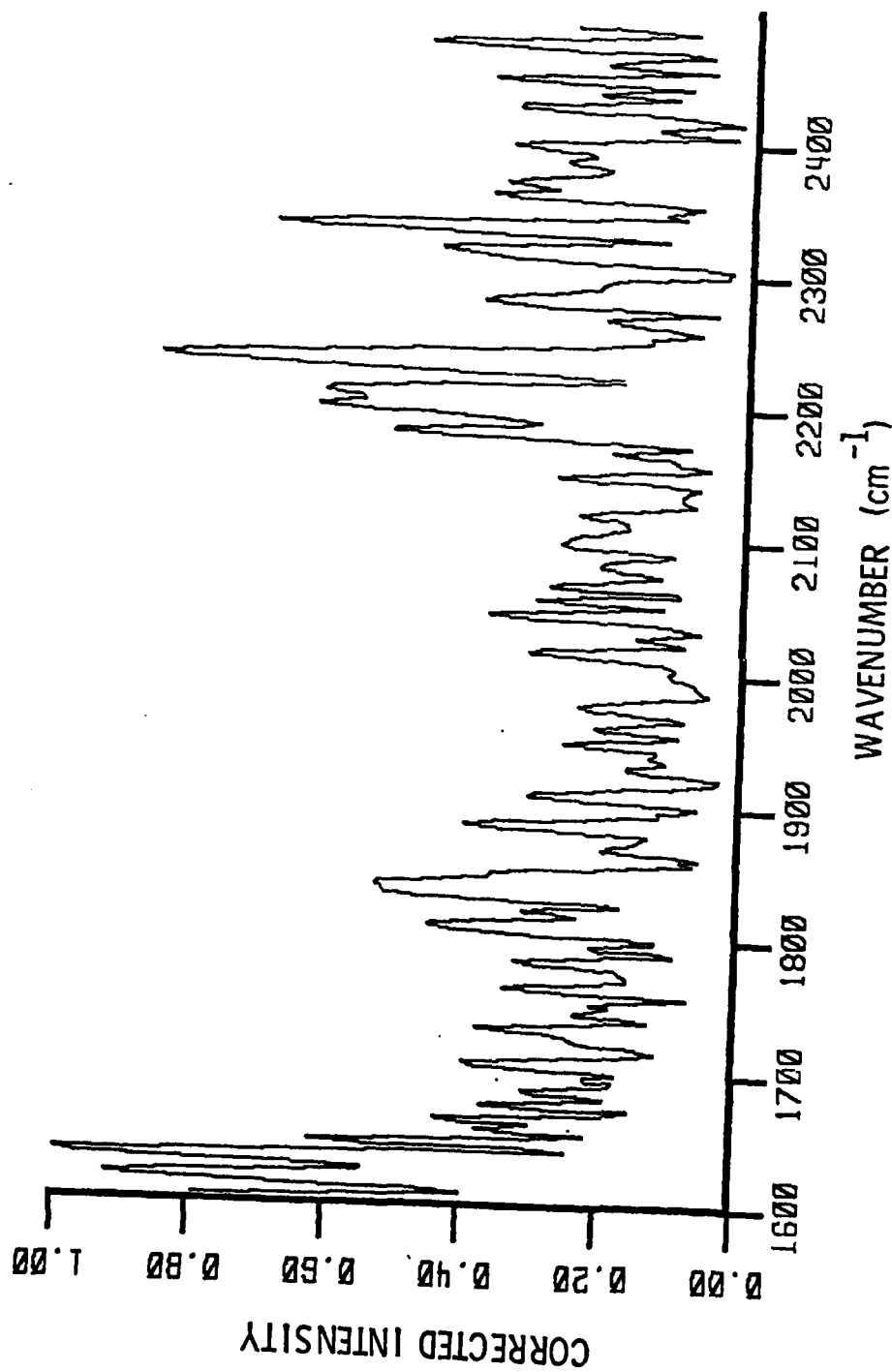
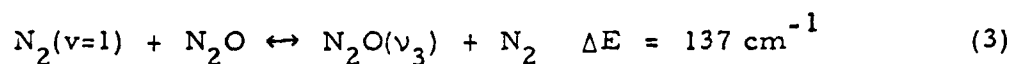


Figure 3: MWIR fluorescence 0.2 msec after beam termination for the same run as Fig. 2. Resolution is 10 cm⁻¹. Maximum intensity is $6.9 \times 10^{-9} \text{ W/cm}^2 \cdot \text{str} \cdot \text{cm}^{-1}$.



is assumed to be in local steady state so that to first order

$$\frac{\text{N}_2(v=1)}{\text{N}_2} = \frac{\text{N}_2\text{O}(v_3)}{\text{N}_2\text{O}} e^{-\Delta E/kT} \quad (4)$$

and thus, since N_2O is a trace species, the decay of $\text{N}_2\text{O}(v_3)$ mirrors the decay of vibrationally excited N_2 . The large energy defect between N_2 and NO, 484 cm^{-1} , precludes a similar effect in the case of NO.

In Fig. 4 the spectrum of irradiated filtered room air under slow-flow conditions is displayed at beam termination. Both NO and $\text{N}_2\text{O}(v_3)$ fluorescence are observed along with radiation from $\text{CO}_2(v_3)$ at 2350 cm^{-1} ($4.3 \mu\text{m}$) as expected. The $\text{N}_2\text{O}(v_3)$ fluorescence intensity is increased by 20% over that of the N_2/O_2 runs of Figs. 2 and 3, while the NO fluorescence has decreased by a third. Carbon dioxide is the dominant spectral radiator. From consideration of the relative bandstrengths of CO_2 , N_2O , and NO, it may be estimated that the $\text{N}_2\text{O}(v_3)$ and NO^* concentrations at beam termination relative to that of $\text{CO}_2(v_3)$ are 1.4 and 5.6 to 1 respectively. A spectrum from the same case corresponding to the fluorescence 0.2 msec after beam termination is shown in Fig. 5. Again the NO fluorescence has disappeared while both the N_2O and CO_2 fluorescence remain unchanged. The fluorescence detected 3.4 msec after beam termination is displayed in Fig. 6. Vibrationally excited N_2O and CO_2 are still both present in the same relative concentrations. The measured decay time of their fluorescence is approximately 14 msec. Like N_2O , CO_2 exhibits a rapid near resonant vibrational exchange reaction with N_2 , i.e.,

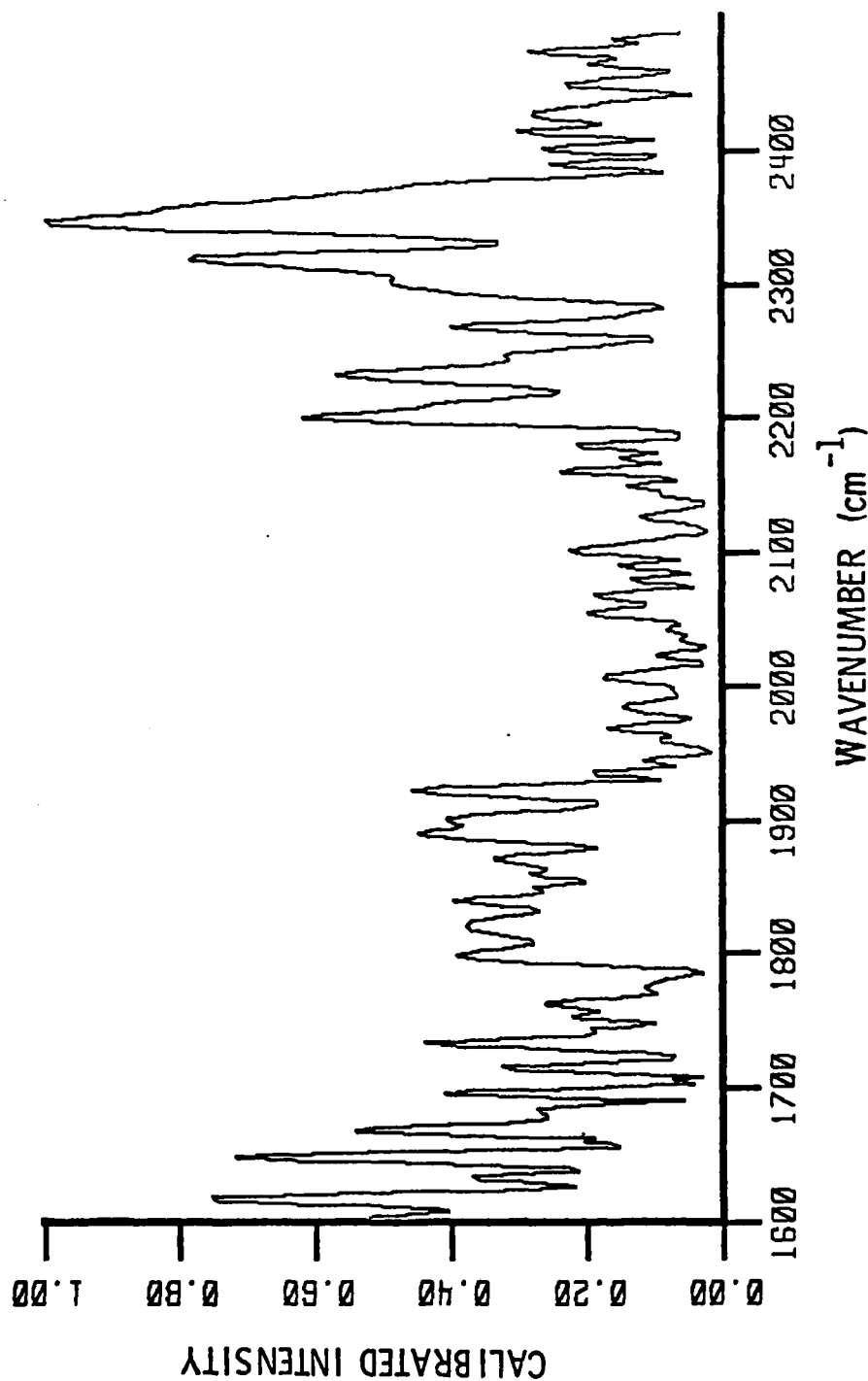


Figure 4: MWIR fluorescence at beam termination from filtered room air at 100 torr pressure and slow-flow conditions. Resolution is 10 cm^{-1} , $V = 36 \text{ kV}$, $i = 1.6 \text{ mA}$. Radiation from NO , $\text{N}_2\text{O}(\nu_1)$, and $\text{CO}_2(\nu_3)$ can be observed. Maximum intensity is $1.1 \times 10^{-8} \text{ W/cm}^2\text{-str-cm}^{-1}$.

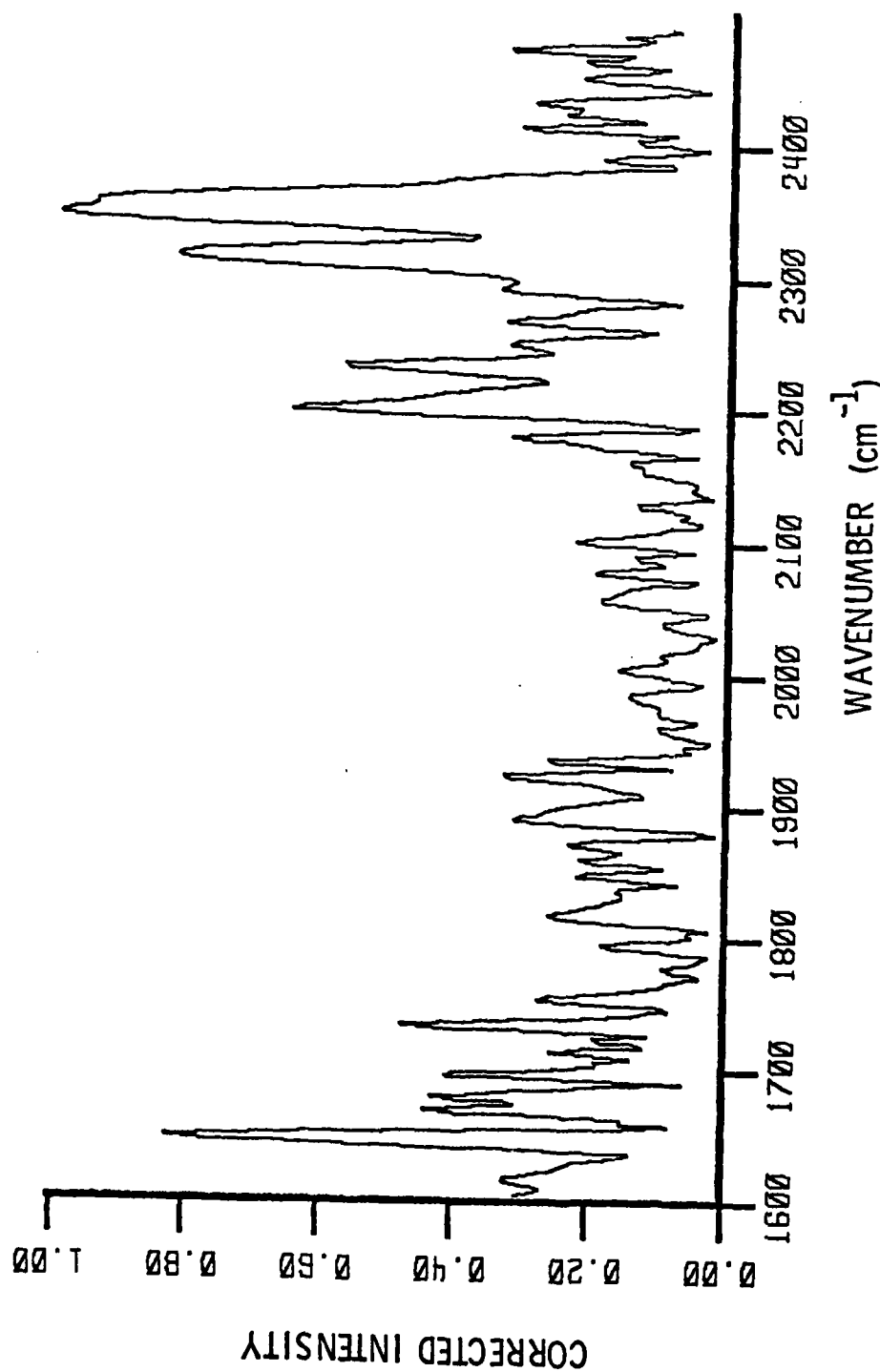


Figure 5: Fluorescence 0.2 msec after beam termination for conditions of Fig. 4. Maximum intensity is $1.1 \times 10^{-8} \text{ W/cm}^2 \text{ -str-cm}^{-1}$.

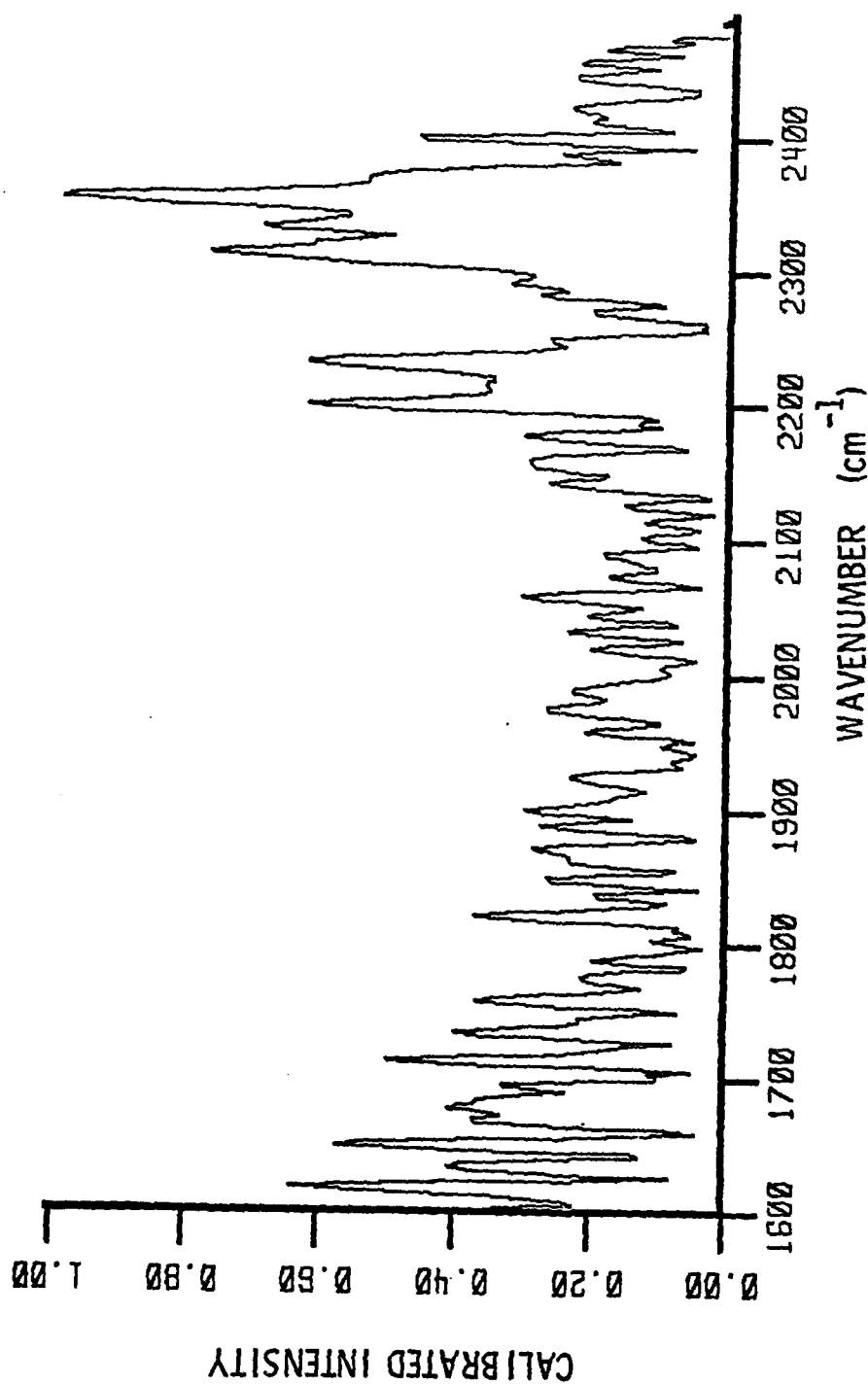
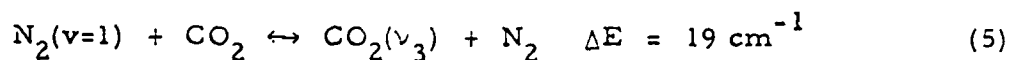


Figure 6: Fluorescence at 3.4 msec after beam termination for run of Figs. 4 and 5. $\text{CO}_2(\nu_3)$ and $\text{N}_2\text{O}(\nu_3)$ radiation are only slightly diminished from beam termination values. Maximum intensity is $9.1 \times 10^{-9} \text{ W/cm}^2 \text{ -str-cm}^{-1}$.



and thus the CO_2 fluorescence will also mirror the decay of vibrationally excited N_2 .

A spectrum taken under slow flow conditions in filtered room air using the PbS detector is shown in Fig. 7. This spectrum, corresponding to the time of beam termination, has a resolution of 20 cm^{-1} and is uncorrected for the spectral response of the detector; the $\text{CO}_2 v_3$ radiation at 2350 cm^{-1} is by far the strongest feature observed although this detector is relatively insensitive to $4.3 \mu\text{m}$ radiation. $\text{N}_2\text{O}(v_3)$ fluorescence, not a prominent feature in the spectrum shown, has also been observed with the PbS detector. The calibrated intensity of the $\text{CO}_2(v_3)$ radiation shown in Fig. 7 agrees to within 20% with a value obtained using the PbSe detector under similar experimental conditions. This excellent agreement reflects both the accuracies of the detector calibrations and the good run to run reproducibility of the data base. The other spectral features evident in Fig. 7 are the radiation of interest in the spectral range of $3500 - 3800 \text{ cm}^{-1}$ and the sharp features around 5500 cm^{-1} ($1.8 \mu\text{m}$) which have been identified as atomic oxygen and nitrogen lines in previous studies performed at the Air Force Geophysics Laboratory.¹³

Figure 8 displays a calibrated version on the spectrum of Fig. 7 over the spectral range of $3100 - 3800 \text{ cm}^{-1}$ ($3.23 - 2.63 \mu\text{m}$). Also shown for comparison is a computer generated NO first overtone spectrum. The generated spectrum is calculated using the latest spectroscopic constants of NO and includes contributions from both total angular momentum states. The shapes of all vibrational/rotation transitions in the synthetic spectrum are broadened

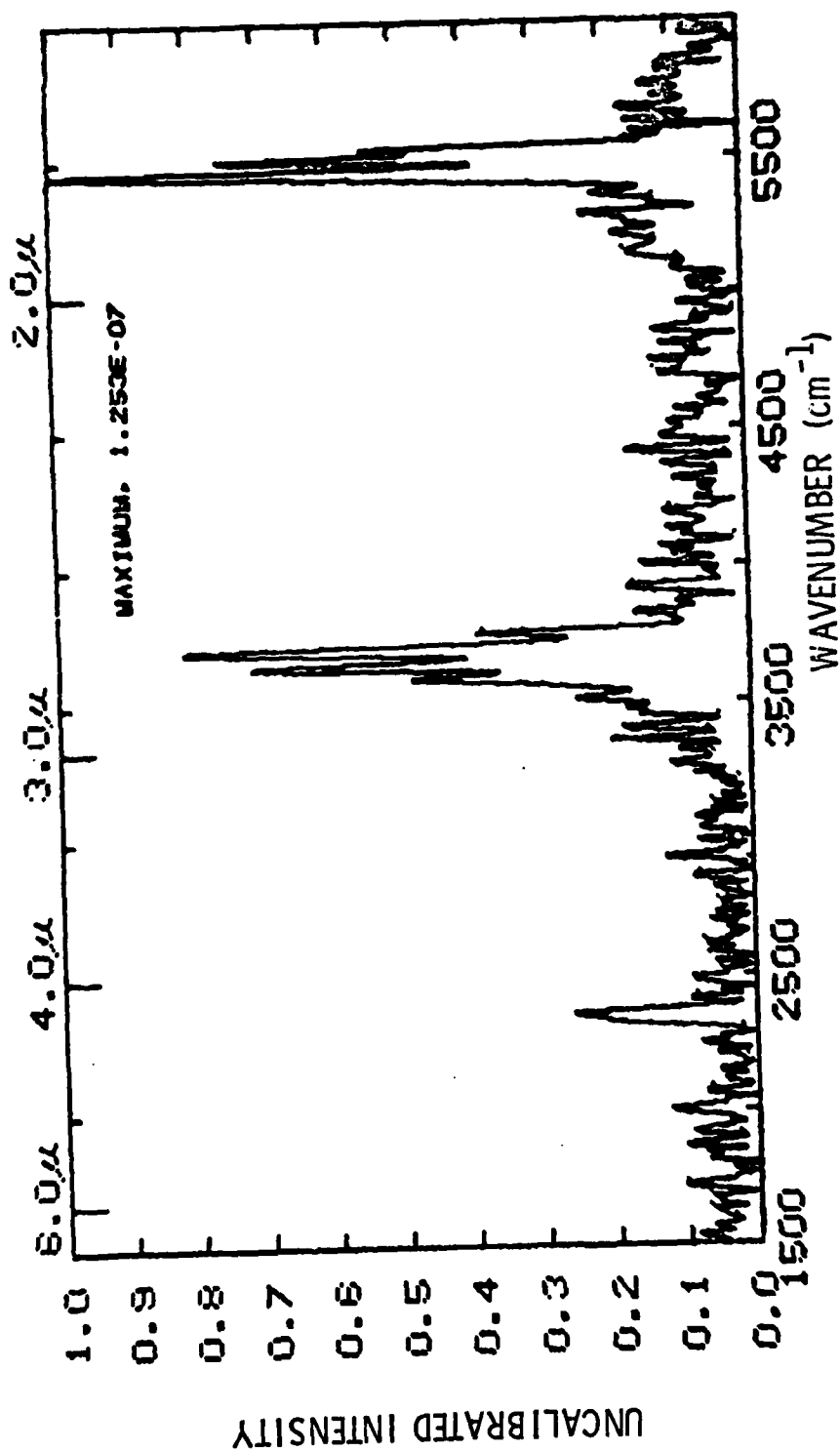


Figure 7: Uncalibrated fluorescence observed with PbS detector at beam termination from filtered room air under standard slow-flow conditions. Resolution is 20 cm^{-1} . Radiation observed is from $\text{CO}_2(\nu_3)$ at $4.3 \text{ } \mu\text{m}$, $\text{NO}(\Delta v=2)$ at $2.7 \text{ } \mu\text{m}$ and atomic O and N at $1.8 \text{ } \mu\text{m}$.

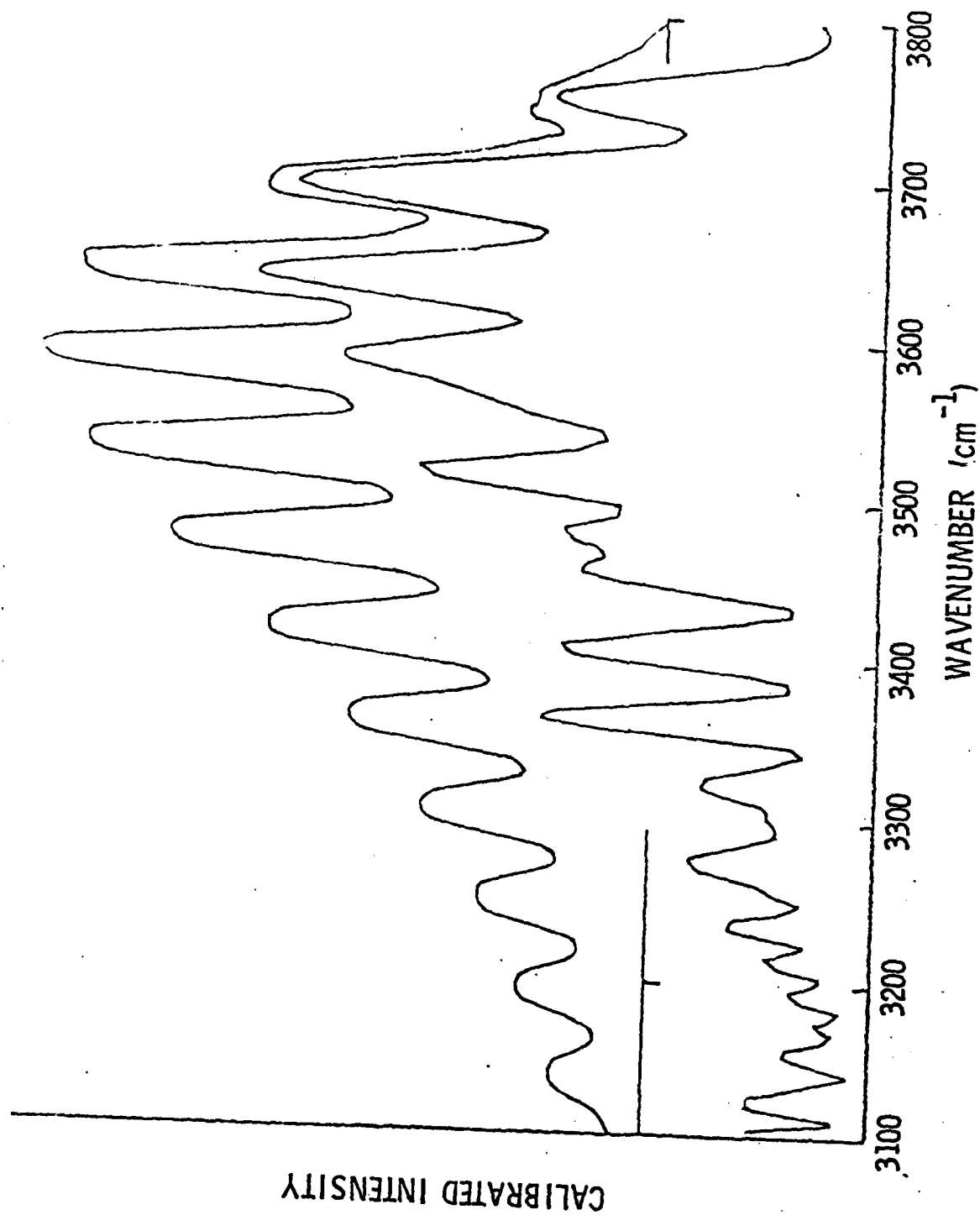


Figure 8: Lower trace: Expansion of 3100 - 3800 cm^{-1} region of Fig. 7. Calibrated maximum intensity is $1.5 \times 10^{10} \text{ W/cm}^2 \cdot \text{str} \cdot \text{cm}^{-1}$. Upper trace: Synthesized spectrum of NO overtone radiation (see text for details).

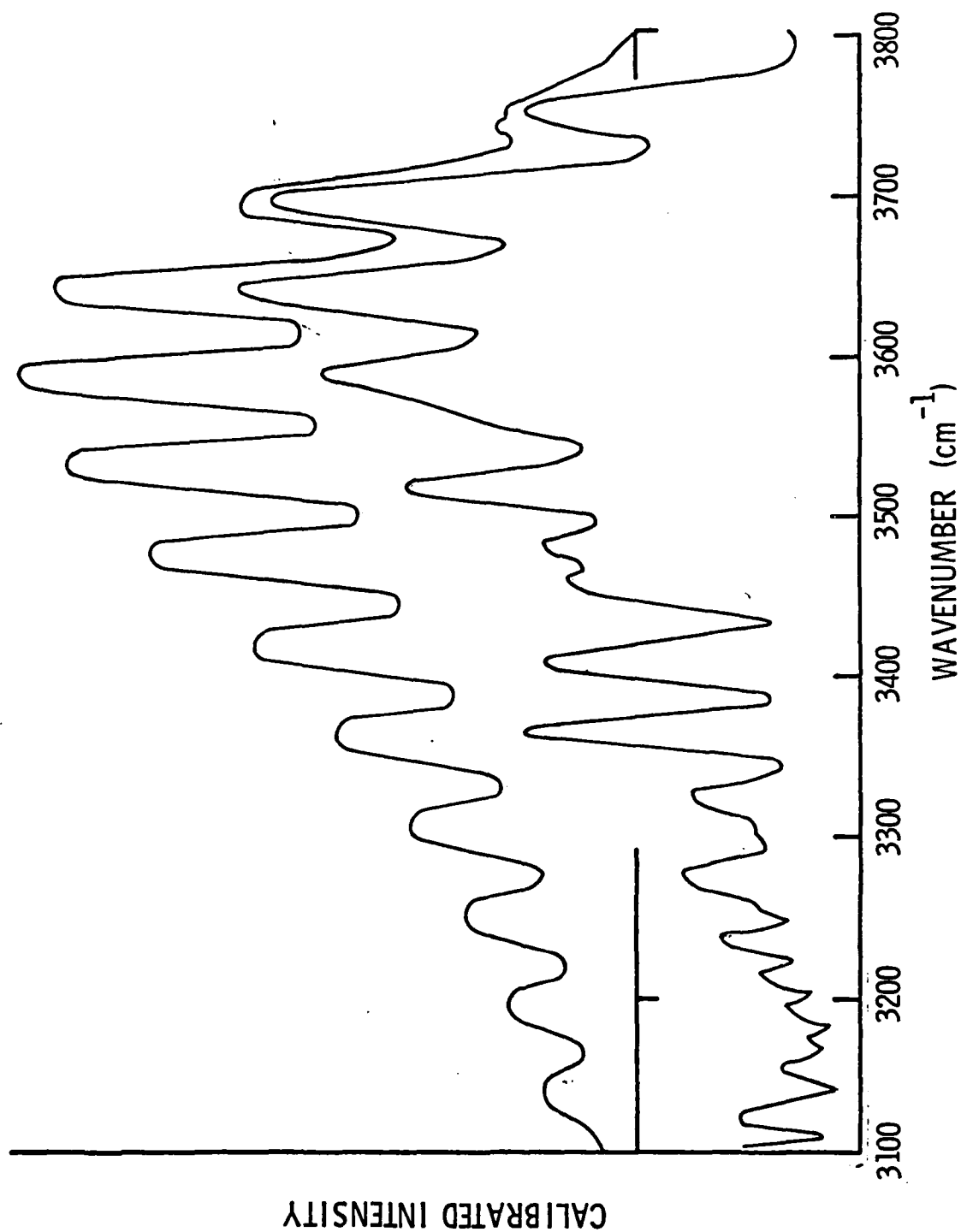


Figure 8: Lower trace: Expansion of 3100 — 3800 cm⁻¹ region of Fig. 7. Calibrated maximum intensity is $1.5 \times 10^{10} \text{ W/cm}^2 \cdot \text{str} \cdot \text{cm}^{-1}$. Upper trace: Synthesized spectrum of NO overtone radiation (see text for details).

by a sinc slit function appropriate to the interferometer used in these experiments. The synthesized spectrum was chosen to have a Boltzmann vibrational distribution corresponding to a vibrational temperature of 5000°K and a rotational temperature of 300°K ; no attempt has been made to fit the two spectra. It is seen that the structure of the experimental spectrum taken in room air lines up very well with the predicted NO spectrum, leading to the conclusion that NO is the dominant radiator in the $2.6 - 3.2\ \mu\text{m}$ region under these conditions. Again fluorescence arising from vibrationally excited NO up to level $v=6$ is observed.

When the spectral resolution is increased to $10\ \text{cm}^{-1}$ reproducible features not attributable to NO appear, as is shown in Fig. 9. Although the noise level of the $10\ \text{cm}^{-1}$ calibrated spectrum is greater than the $20\ \text{cm}^{-1}$ spectrum of Fig. 8, the features indicated by arrows are reproducible both as a function of time and from run to run. The expected spectral shapes of the $\text{N}_2\text{O}(02^{\circ}1 \rightarrow 00^{\circ}0)$ and $(10^{\circ}1 \rightarrow 00^{\circ}0)$ combination bands as well as the $\text{CO}_2(02^{\circ}1 \rightarrow 00^{\circ}0)$ and $(10^{\circ}1 \rightarrow 00^{\circ}0)$ combination bands are also shown in Fig. 9. It is clear that CO_2 radiation does not occur in any significant amount in this spectral region. The N_2O combination band at $3480\ \text{cm}^{-1}$ does seem to match the frequency, if not the shape, of some of the unidentified spectral features. (This band is predicted to be the strongest in this spectral region⁵ for N_2O in vibrational equilibrium at room temperature.) Nonetheless, even if the $3480\ \text{cm}^{-1}$ features are attributed to N_2O , other strong features remain unexplained.

The SWIR spectrum of a slow flow run taken with a 80% N_2 / 20% O_2 mixture is shown in Fig. 10. The data, shown with $10\ \text{cm}^{-1}$ resolution, is

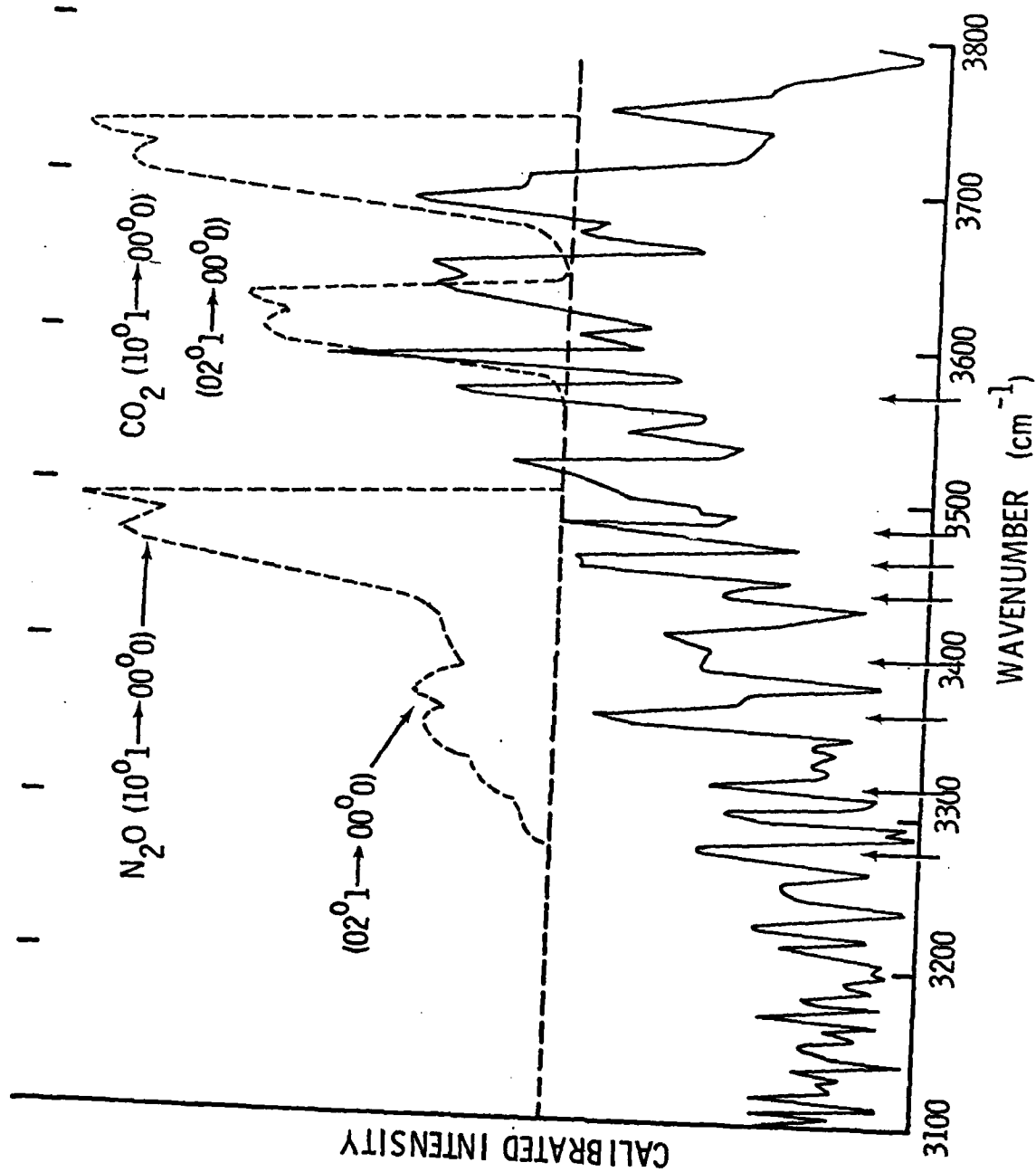


Figure 9: Lower trace: Spectrum of filtered room air as in Figs. 6 and 7 at 10 cm^{-1} resolution. Maximum calibrated intensity is $1.8 \times 10^{-10} \text{ W/cm}^2 \text{ - str - cm}^{-1}$. Upper traces: Estimated N_2O and CO_2 combination band shapes and relative intensities. Arrows along bottom axis indicate reproducible features not due to NO.

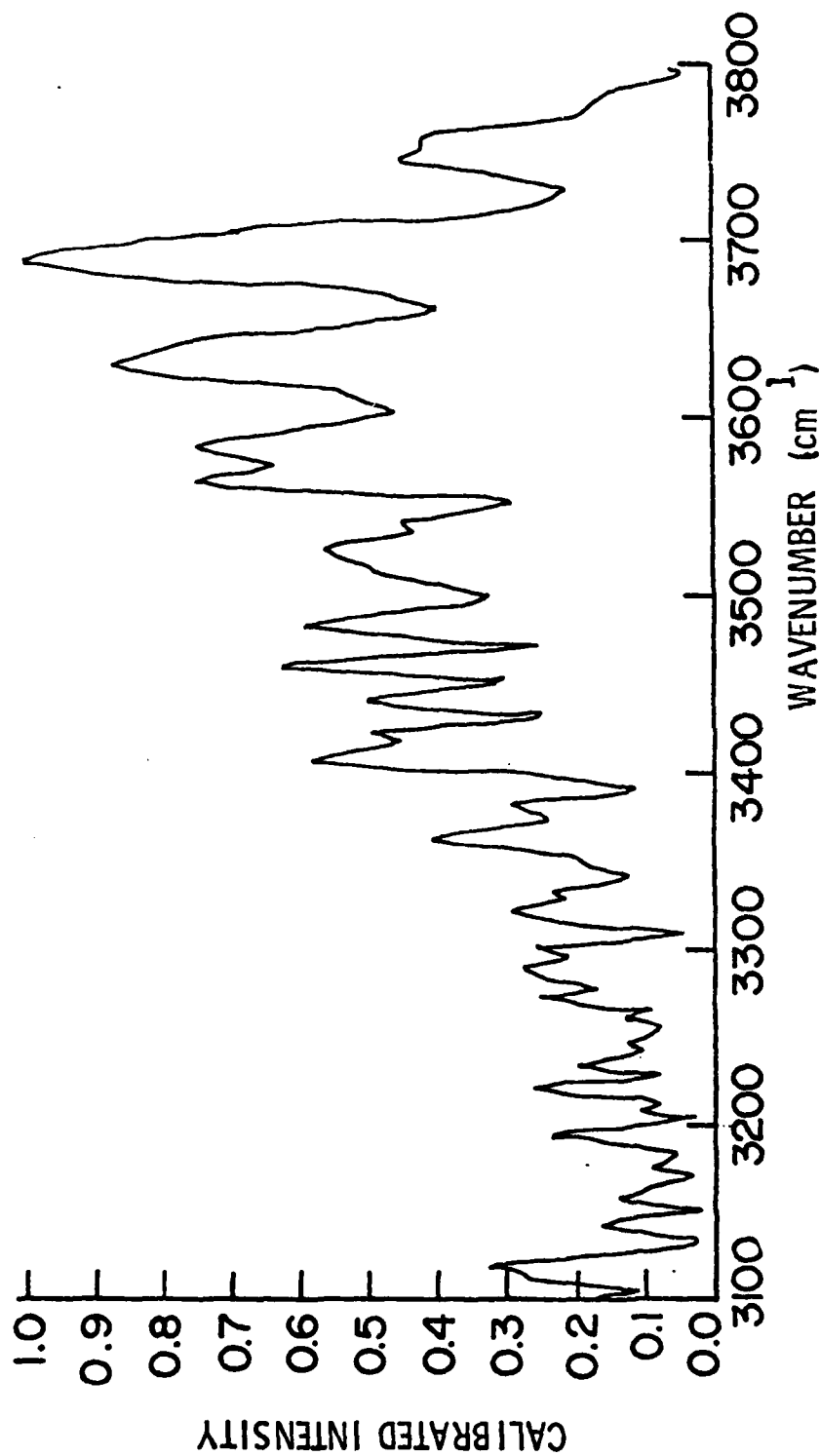


Figure 10: SWIR fluorescence from 80% nitrogen/20% oxygen mixtures at 100 torr pressure under slow-flow conditions. Resolution is 10 cm^{-1} . Maximum intensity is $3.6 \times 10^{-10} \text{ W/cm}^2 \cdot \text{str} \cdot \text{cm}^{-1}$. Increase in NO radiation is in agreement with MWIR observations - NO fluorescence was decreased in the presence of CO_2 .

taken at the time of beam termination. Again, as for the filtered room air cases, NO is the dominant radiator in the spectral region shown. The lack of significant CO₂ radiation in this spectral region is demonstrated in Fig. 11 which provides a comparison between the spectra recorded in filtered room air and an 80% N₂/20% O₂ mixture where no CO₂ should be present. It can be seen that there are no observable differences between the two scans, with the exception that the laboratory air case appears to have a somewhat greater spectral resolution. Interestingly enough even the features attributed to noise appear to line up; the unexplained spectral features of the air runs are also present in the N₂/O₂ experiments.

Measurements taken under faster flow conditions and for much shorter residence times yield similar spectra. In these cases only runs using the PbS detector were possible due to decreased signal intensity, but the unidentified features remained. If these features were attributable to a build up of beam created species, such as N₂O, their relative intensity should have been greatly diminished because of the decreased residence time. In fact, N₂O(ν_3) radiation at 4.5 μ m was no longer observed for these runs (with the PbS detector). Radiation arising from NO $\Delta v=2$ transitions is still the dominant radiation source at 2.7 μ m under these conditions, and the NO vibrational distribution appears to be very similar to that of the higher pressure runs.

The experiments performed using trace concentrations of oxygen mixed with nitrogen provided slightly more signal in the MWIR region. No evidence of N₂O fluorescence at 4.5 μ m is observed in these spectra. The observed vibrational distribution of NO is not greatly different from that of the 80% N₂/20% O₂ mixture data of Fig. 2. In these runs the nitrogen pressure

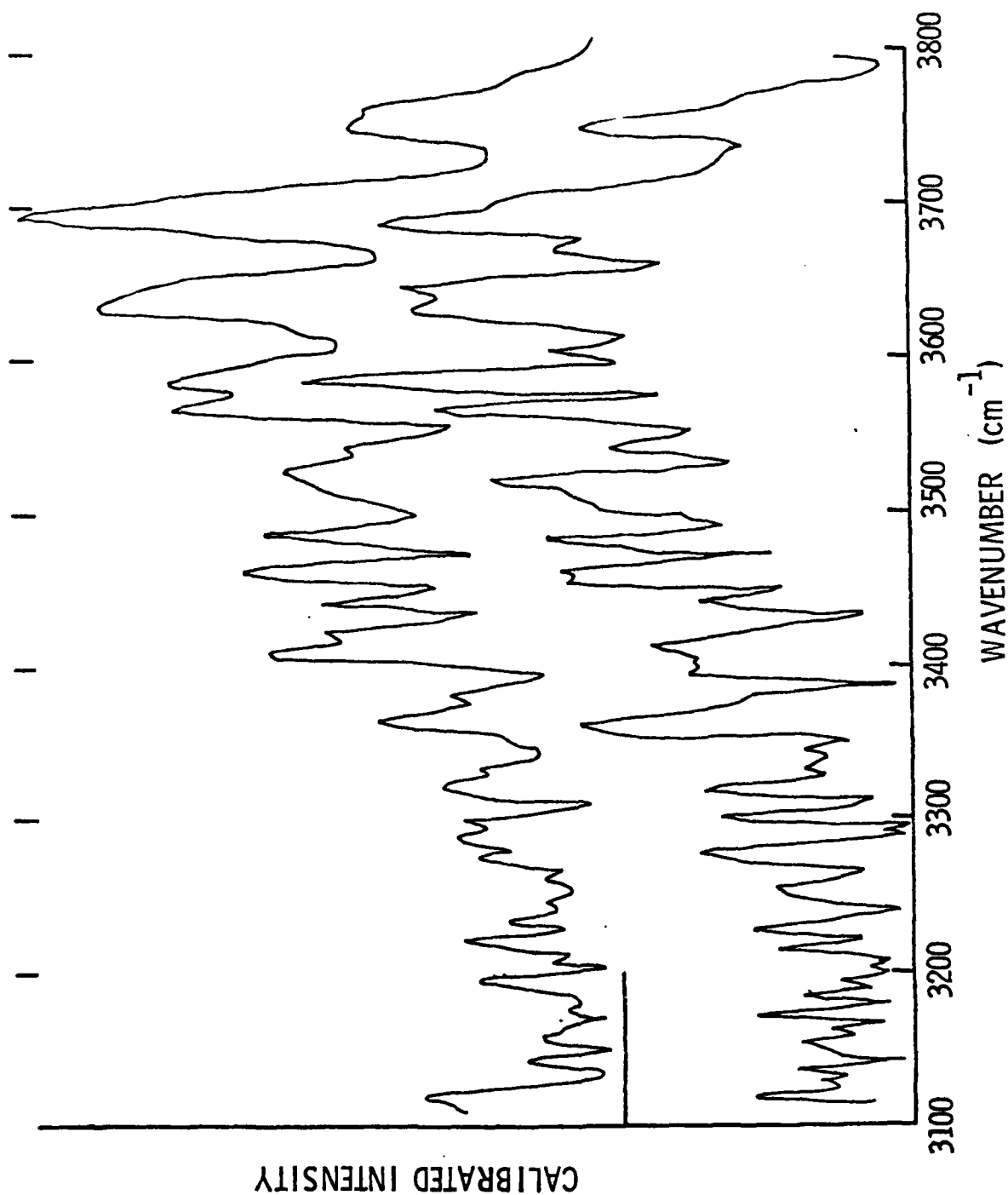


Figure 11: Comparison of N₂/O₂ and room air spectra taken under similar conditions. Resolution is 10 cm⁻¹. Lower trace: room air fluorescence (Fig. 9). Upper trace: N₂/O₂ fluorescence (Fig. 10).

was varied from 25 - 115 Torr and the oxygen pressure, set to achieve maximum intensity, was varied from 0.2 - 0.75 Torr. No variation in the observed NO excited vibrational distribution was noted over this range of conditions. The measured NO fluorescence decay rate was in good agreement with previous observations.¹¹ A more systematic study of this type might permit the measurement of individual vibrational level decay rates of NO by N₂ and O₂.

When the PbS₂ SWIR sensitive detector was used, the observed NO spectral intensity increased by a factor of two over the air cases. The unidentified features noted previously all increased by an even greater amount, about a factor of four, and are the most prominent spectral features, as shown in Fig. 12. The displayed spectrum is from a 100 torr N₂, 0.03 torr O₂ slow flow run, and corresponds to the time of beam termination. The NO vibrational bands are greatly obscured by the sharp spiked features, which have widths equal to the experimental resolution. Since unresolved vibrational-rotational bands would have spectral widths much greater than this, the features were suspected to be either due to atomic lines or individual rotational lines of a molecular vibrational band.

Under certain conditions the unidentified spectral features were found to persist long after NO fluorescence had decayed. Figure 13 shows a spectrum taken in the same experiment as Fig. 12, but at a time corresponding to 3.4 msec after beam termination. Some residual NO radiation from the slowest decaying observable level ($v=2$) might be present between 3650 and 3770 cm⁻¹. Most striking, however, is the appearance of the unidentified spectral features. Indeed some weaker features attributed to noise in the other runs are observed to be reproducible with time under these conditions.

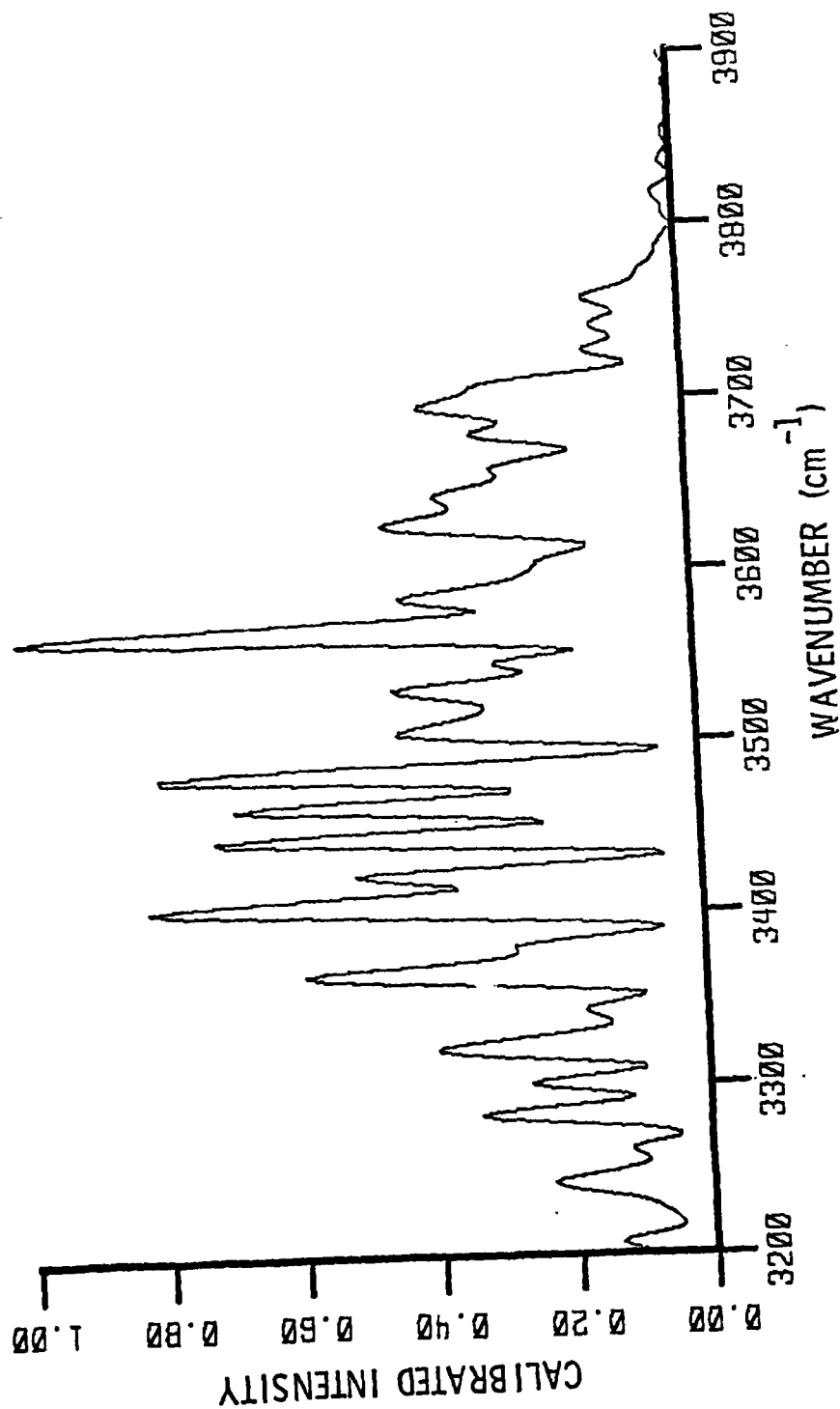


Figure 12: SWIR fluorescence from a trace oxygen run under slow-flow conditions. The N₂ pressure is 100 torr, O₂ pressure is 0.03 torr. Resolution is 10 cm⁻¹ and maximum intensity is $6.1 \times 10^{-10} \text{ W/cm}^2 \cdot \text{str} \cdot \text{cm}^{-1}$ at beam termination. The NO radiation is no longer the dominant spectral radiation.

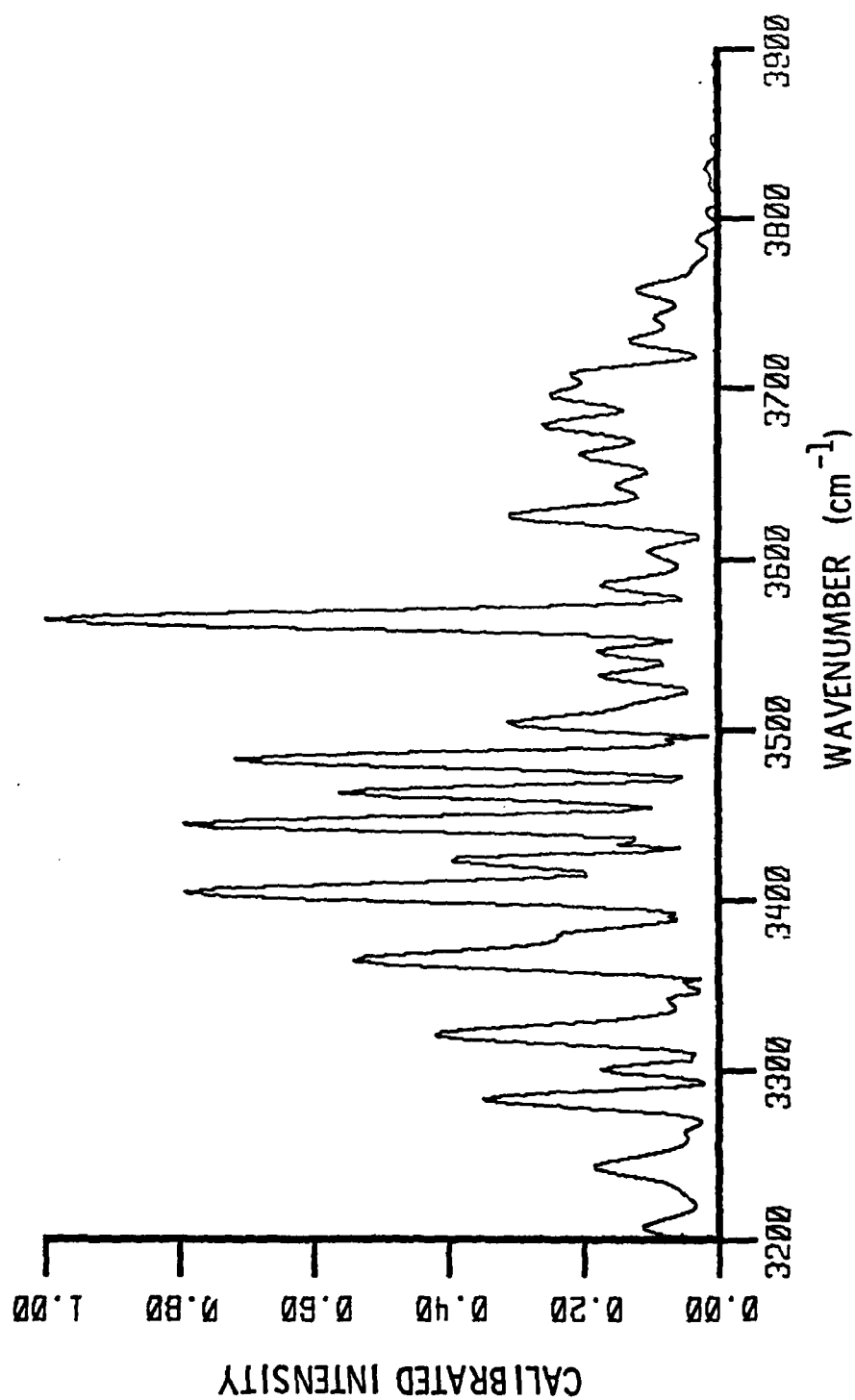


Figure 13: SWIR fluorescence 3.5 msec after beam termination for run of Fig. 12. Maximum intensity is $1.9 \times 10^{-10} \text{ W/cm}^2 \text{-str-cm}^{-1}$. The NO overtone radiation has virtually disappeared, isolating the spectral lines of interest.

Note that the relative intensity of the lines appears unchanged from early time observations, see comparison of Figs. 12 and 13. These long time observations provided a much clearer picture of the unidentified radiator. Specifically the strong features at $\sim 3560 \text{ cm}^{-1}$ was noted to agree well with the frequency of the Q branch of the $\text{OH}(\nu=1 \rightarrow 0)$ transition. The free radical OH was considered a likely radiation source inasmuch as water was introduced into the system with the room air and could have a long residence time on the chamber surfaces for typical system pumping rates.

In order to verify the tentative assignment, a synthetic spectrum of the OH molecule was generated. The OH free radical has an inverted $^2\Pi$ ground electronic state with strong coupling between spin and angular momentum giving rise to two total angular momentum manifolds of states $\Omega=1/2$ and $3/2$. Transitions between similar states within these manifolds are not degenerate, and should be easily observable. Coupling of rotation to the total angular momentum is a complex function of the rotational and vibrational energy and a vibrating rotor-anharmonic oscillator model of the spectrum is not sufficient. Detailed predictions of the OH spectral line positions and strengths have been performed by Mies¹⁴ and shown to be in good agreement with experimental spectra. Mies' calculated frequencies and Einstein coefficients were used to generate a synthetic OH spectrum using a sinc slit function and assuming a 300°K rotational temperature. A comparison between this synthesized spectrum and the long time spectrum of Fig. 13 is presented in Fig. 14. (Note that the synthetic spectrum exhibits negative values of intensity. This is a result of convoluting the predicted OH spectrum over a sinc slit function which displays prominent negative sidelobes. This effect

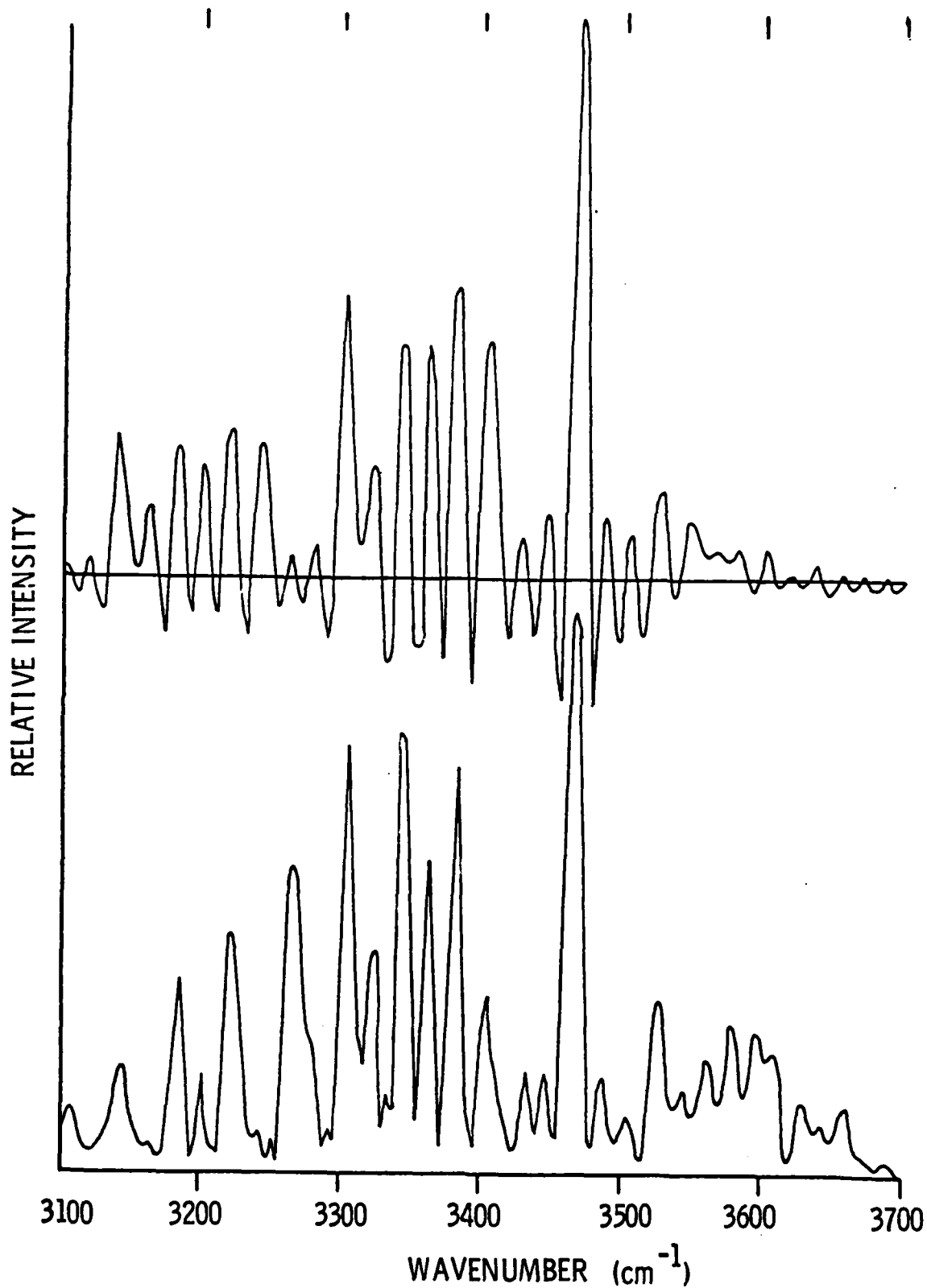


Figure 14: Comparison of synthetic spectrum of OH with spectral features of Fig. 13. All significant features (except 3270 cm⁻¹ line) are matched by OH predictions.

is an artifact of the Fourier transform.) It can be seen that the prominent spectral features match OH vibration/rotation lines. In addition, excellent agreement occurs between the spectral positions of nearly all of the weaker features and OH lines arising from high J levels and the weaker, $\Omega_{1/2}$ transitions. Note that in the synthetic spectrum the relative populations of the two spin states and the rotational levels are assumed to be in the thermal equilibrium with the gas kinetic temperature. The observed relative OH vibrational populations can be readily determined from the measured Q branch intensities and it has found that the relative populations of OH $v=2$ and $v=1$ are nearly equal at beam termination ($n_2/n_1=0.8$) for all the runs in which they could be observed (including trace oxygen, and fast and slow flow cylinder gas and room air runs.)

Upon backchecking it was found that the OH spectrum was not observed in early runs made using cylinder gases prior to that admission of room air into the chamber. Thus it appears that once water vapor was admitted it strongly adhered to the chamber surfaces and ultimately gave rise to the OH fundamental band radiation even in "dry" air mixtures. Additionally, not all the ambient water vapor is removed by the trap in the filtered room air measurements.

Due to the slow time response of the PbS detector, only estimates of the quenching rates of OH by O_2 and N_2 could be made. The total OH quenching rate constant by an air mixture of N_2/O_2 has been measured¹⁵ as 1.5×10^{-14} cm³/sec, dominated by O_2 quenching. Observations from the present work support O_2 quenching of OH as faster than N_2 , but slower than O_2

quenching of NO. Quenching of OH by N_2 appears to be significantly faster than quenching of NO by N_2 , and is estimated to have a rate constant of order $1.5 \times 10^{-15} \text{ cm}^3/\text{sec}$ which is approximately 10% of the rate constant for quenching by O_2 . These observations arise from the analysis of the low pressure trace oxygen runs. The slow decay of the OH radiation in Figs. 12 and 13 ($P=100 \text{ torr}$) can possibly be explained by vibrational pumping from $N_2(v \geq 2)$ which would not make as large a contribution in the low pressure runs (a more detailed investigation is obviously required). Observations of the decay OH($v=2$) are limited and estimates of the quenching rates are not possible. It should be emphasized that the present study was not designed to study OH kinetics and the above observations must be considered qualitative rather than quantitative. For example the possible chemical destruction of OH, through reactions with beam produced species, has not been considered.

A number of interesting side features which could be studied in more detail have been observed in this data. These include: (a) the observation of OH fluorescence and decay which might be utilized to ascertain fundamental quenching rate constants for vibrationally excited OH, (b) NO fluorescence data sufficiently resolved to allow determination of vibrational level dependent quenching rate constants and relative fundamental to first overtone band Einstein coefficients, and (c) the possibility of using trace quantities of CO_2 to determine relative populations of N_2O and vibrationally excited N_2 .

V. REFERENCES

1. "Proceedings of the HAES Infrared Data Review", 13-15 June 1977, Falmouth, MA. Air Force Geophysics Laboratory report OP-TM-05, 1977
2. Ibid, pp 327-341, presented by H. Mitchell
3. R. R. O'Neil, unpublished results
4. R. E. Murphy, unpublished results
5. R. A. McClatchey, W. S. Benedict, S. A. Clough, D. E. Burch, R. F. Calfee, K. Fox, L. S. Rothman and J. S. Garing; "Atmospheric Absorption Line Parameters Compilation", AFCRL report TR-73-0096, 26 Jan. 1973.
6. R. E. Murphy, F. H. Cook, G. E. Caledonia and B. D. Green, "Infrared Fluorescence of Electron Irradiated CO₂ in the Presence of N₂, Ar and He", AFGL report TR-77-0205, 15 Sept. 1977.
7. F. H. Cook, and R. E. Murphy, "A Synchronous Signal Processing Technique for Repetitive Arbitrary Waveforms", AFCRL Report TR-76-0035, 19 Jan. 1976
8. R. E. Murphy, F. H. Cook and H. Sakai, "Time Resolved Fourier Spectroscopy", J. Opt. Soc. Amer. 65, 600 (1975)

9. R. O'Neil and G. Davidson, "The Fluorescence of Air and Nitrogen Excited by Energetic Electrons", American Science and Engineering, Inc. report ASE-1602 (AFCLR-67-0277), 1 Jan. 1968.
10. F. P. Billingsley II, "Calculated Vibration Rotation Intensities for $\text{NO}(X^2\Pi)$ ", J. Molec. Spectrosc. 61, 53 (1976)
11. R. E. Murphy, E. T. P. Lee and A. M. Hart, "Quenching of Vibrationally Excited Nitric Oxide by Molecular Oxygen and Nitrogen", J. Chem. Phys. 63, 2919 (1975)
12. J. T. Yardley, "Vibration-to-Vibration Energy Transfer in Gas Mixtures Containing Nitrous Oxide", J. Chem. Phys. 49, 2816 (1968)
13. R. E. Murphy, A. R. Fairbarn, J. W. Rogers and A. M. Hart, "Near IR Nuclear Spectra: Interpretation by Recent Laboratory Results", presented at the Fourth Strategic Space Symposium, Monterey, CA, 23 Sept. 1975
14. F. H. Mies, "Calculated Vibrational Transition Probabilities of $\text{OH}(X^2\Pi)$ ", J. Molec. Spectrosc. 53, 150 (1974)
15. R. E. Murphy, "Infrared Emission of OH in the fundamental and First Overtone Bands", J. Chem. Phys. 54, 4852 (1971)

END

DATE
FILMED

4-82

DTIC